RICE UNIVERSITY

Quantum Transport and Microwave Response in Modulated High-Mobility Two-Dimensional Electron Systems

by

Yanhua Dai

A THESIS SUBMITTED
IN PARTIAL FULFILLMENT OF THE
REQUIREMENTS FOR THE DEGREE

Doctor of Philosophy

APPROVED, THESIS COMMITTEE:

Rui-Rui Du, Chair
Professor of Physics and Astronomy

Emilia Morosan
Assistant Professor of Physics and Astronomy

Junichiro Kono
Professor of Electrical and Computer Engineering

Houston, Texas

April, 2011

Abstract

Quantum Transport and Microwave Response in Modulated High-Mobility Two-Dimensional Electron Systems

by

Yanhua Dai

Two-dimensional electron gas (2DEG) in microwave irradiation has been an intriguing system to study transport properties of electrons for a decade, during which extensive important phenomena have been discovered, such as microwave induced resistance oscillation (MIRO), zero resistance state(ZRS) and zero conductance state(ZCS). Along this direction, this thesis is devoted to new phenomena recently discovered in such systems, 1) microwave induced cyclotron harmonic peak ($2\omega_C$ spike) in ultra-clean 2DEG without antidots inducing electric modulation potential 2) Aharonov-Bohm(AB) oscillations in microwave irradiated 2DEG with modulation potential. Those phenomena originate from quantum interference, from either interplay between two different kinds of scattering or different electrons transition paths.

In addition to microwave induced phenomena, other nonlinear effects such as Zener tunneling and geometric resonance(GR) have been investigated further in the past few years and collected in this thesis. Zener tunneling has been found in two-dimensional hole gas(2DHG) with a large damping factor, which inspires more questions on the

unique band structures of holes. GR has been studied in ultra-clean modulated 2DEG , in which more oscillation peaks show up. In the GR regime with an inplane magnetic field applied, the antisymmetric hall oscillations lead us to propose the existence of a magnetic lattice along with an artificial antidots lattice and a current lattice in such systems.

Acknowledgments

In the first place, I would like to thank my thesis adviser Dr. Rui-Rui Du, who has been always by my side, so generous and ready to help on my long way towards my Ph.D. He not only led me into the world of quantum transport on 2DEG in low temperature, by questioning, inspiring, and teaching, but also set me a real model of a responsible and earnest physicist.

Next, I would like to thank my committee members, Dr. Junichiro Kono, and Dr. Emilia Morosan for their insightful discussions and advices on my thesis and defense. Thanks also go to Dr. Anthony Chan, who supervised me in my Master's defense.

The wafers employed in this work were partly from Dr. M. J. Manfra, Dr. L. N. Pfeiffer, and Dr. K. W. West, without their generous support, my research road would definitely be tougher.

I would also like to thank my labmates, Dr. Chi Zhang, who rendered me numerous help on experiments, and Dr. Z. Q. Yuan, who imparted the fabrication and low temperature skills to me. Dr. Kris Stone, Ivan Knez and Xiaowei He are also greatly appreciated for their assistances on experimental processes.

Majority of the work was carried out in Rice Shared Equipment and Rice Quantum Transport Lab, supported and funded by National Science foundation. High Magnetic Field Lab in Tallahassee assisted in some experiments as well. Thank you.

Last but not the least, I would like to thank all my friends in Rice University, for the joy and happiness you guys have brought to me. I cannot imagine a long journey

v

without y'all! My parents and my little brother, needless to say, thank you, for the unconditional love and trust! Finally, I want to thank my boyfriend Lanyue Lu for his love and efforts in helping me in all possible ways.

Contents

Tables

Illustrations

Chapter 1

Introduction

26 years ago, the 1985 Nobel Prize in physics was awarded to Dr. K. von Klitzing, for his discovery of Integer Quantum Hall Effect (IQHE) in two-dimensional electron gas (2DEG) [8]. Ten years later, the Nobel Prize was bestowed on Dr. D.C. Tsui, Dr. H.L. Stormer, and Dr. R.B. Laughlin for their pioneering work on Fractional Quantum Hall Effect (FQHE) in 2DEG [9, 10]. In the last few decades, 2DEG has been a very important system explored by physicists

2DEG is a thin layer of electrons trapped in a sandwich structured compound semiconductor, such as GaAs/InGaAs. 2DEG can be treated as two-dimensional ideal gas insulated from outside environment in a temperature around 0K because of highly confined spacial distribution of electrons and uniform momentum. In a high perpendicular magnetic field, because of the cyclotron motion of electrons, the longitudinal magnetoresistance shows Shubnikov-de Haas (SdH) oscillations and the Hall resistance shows a series of quantized values $R_\nu = R_H \cdot \nu$ with $R_H = 25.8k\Omega$, and $\nu = 1, 2, 3....$The later was referred to as IQHE, which was first discovered in a silicon Metal Oxide Semiconductor Field Effect Transistor (MOSFET) [8]. This phenomenon could be understood by the semiclassical picture for independent electrons. More quantized resistance values were discovered later with fractional filling factors $\nu = 1/3, 1/2....$ The first factor 1/3 was discovered by Dan. Tsui et al [9]and new types of

quasi particles named as composite fermions (CF) were proposed to carry a fraction of elementary charge. Later, a theory was established by Laughlin to understand this novel phenomenon and further predict a family of similar ground states. [10].

In a low magnetic field, with modulation fields applied, 2DEG exhibits new phenomena,such as Zener tunneling, Microwave Induced Resistance Oscillation(MIRO), and Geometric Resonance(GR).

Zener tunneling refers to oscillating resistance in response to a sweeping low magnetic field when a strong DC electric current is applied through a Hall bar. The periods of oscillations are $B_l \propto \frac{I_{dc}}{wl}$, where $l = 1, 2, 3...$ is the order of peaks and w is the width of the Hall bar[2]. Zener tunneling was also proposed to explain the breakdown of quantum hall state by Tsui et al Tsui et al. [11].

MIRO is the phenomenon that when microwave shines on a high mobility sample, it induces the resistance oscillations with the order $\varepsilon = \frac{\omega_{MW}}{\omega_C}$, where $\omega_{MW} = 2\pi f_{MW}$ and $\omega_C = \frac{eB}{m^\star}$ is the cyclotron frequency[12, 13, 14]. For low orders, the valley of resistance oscillation can reach zero, corresponding to zero resistance state (ZRS) in some ultra-high mobility samples [3, 15]. The conductance was later found to be zero in the same regime and obey the relation $\sigma_{xx} \approx (n_e e/B)^2 \rho_{xx}$, which corresponds to zero conductance state (ZCS) [16].

GR is the resistance oscillation induced by a spatial electric potential . One dimensional and two dimensional periodic potentials were physically realized by lithography techniques. The resistance oscillations occurred when two parameters, namely the

modulation potential diameter and the cyclotron orbit diameter, are commensurable [17, 18, 19, 20, 21, 4].

In the following chapters, I will first introduce the background of the magneto-transport of 2DEG as well as previous experimental results on nonlinear transport in a low magnetic field.

Then I will discuss new results on 2DEG, including the new spike in ultra-clean GaAs/AlGaAs samples and Aharonov-Bohm (AB) effect in the spatially modulated samples, both of which are induced by microwave irradiation and imply the presence of quantum interference. GR on modulated 2DEG also exhibits more clear features and its combination with hall oscillations in this regime indicates the existence of magnetic lattices.

What follows is the discussion on Zener tunneling and MIRO in two dimensional hole gas (2DHG). These two phenomena render us to gain more insights in complex band structures of 2DHG.

The appendixes of this thesis contain fabrication techniques of antidots and some raw data on other 2DEG systems, including InP/InAlAs and InAlAs/InGaAs, in the research of quantum insulator states.

Chapter 2

Quantum Transport in Two Dimensional Electron/Hole Systems

2.1 GaAs/AlGaAs Structure and 2DEG

Gallium Arsenide (GaAs) is one type of III/IV compound semiconductors with the Zinc blend type structure2.1. Aluminum Gallium Arsenide (AlGaAs) has a lattice structure similar to GaAs and therefore AlGaAs can grow on top of GaAs layers without any strain. 2DEG is trapped between the layers of GaAs and AlGaAs because of their difference in conduction band electric potentials 2.2.

2.2 Band Structure for Electron and Hole Gas in GaAs

The conduction band in GaAs can be treated as a simple parabola around $k \sim 0$. The dispersion relation is $\varepsilon(k) = E_C + \frac{\hbar^2 k^2}{2m_e^\star}$, with E_C the energy at the bottom of the conduction band and $m_e^\star$ the effective mass of electrons.

For the valence band , because it is constructed from three p orbitals, p_x, p_y, p_z, it contains two degenerate 'heavy' hole bands (light heavy (LH) hole band and heavy heavy (HH) hole band) and one 'light' hole band . The dispersion relation near $k \sim 0$ is $\varepsilon(k) = E_V - \frac{\hbar^2 k^2}{2m_h}$, with E_V the energy at the top of the valence band and $m_h^\star$ the effective mass of holes.
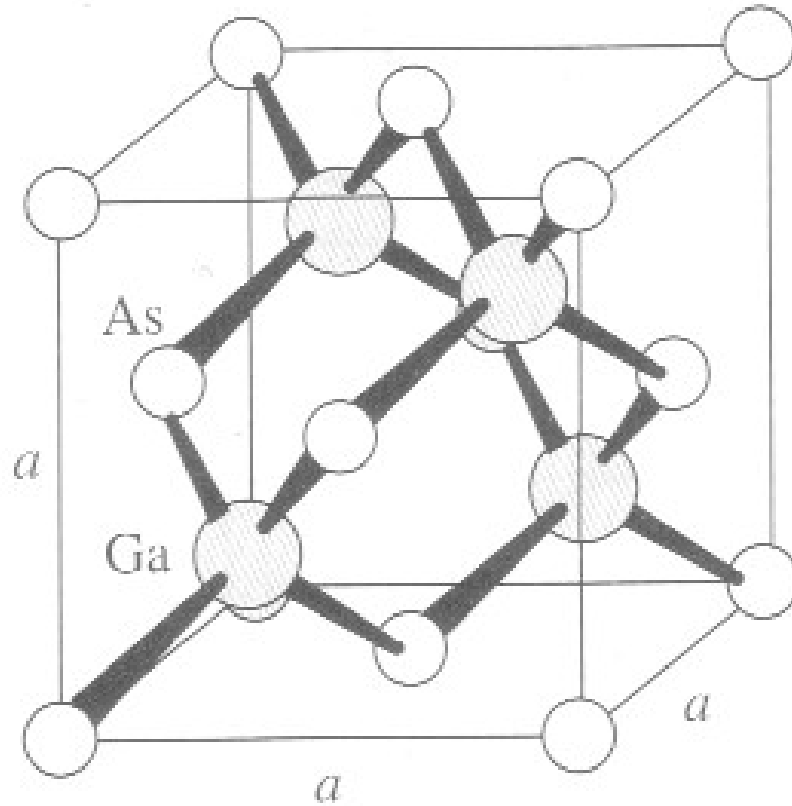
Figure 2.1 : The GaAs crystal structure, taken from
http://ogrenci.hacettepe.edu.tr/~b0123174/HW3PictureOfGaAs.htm
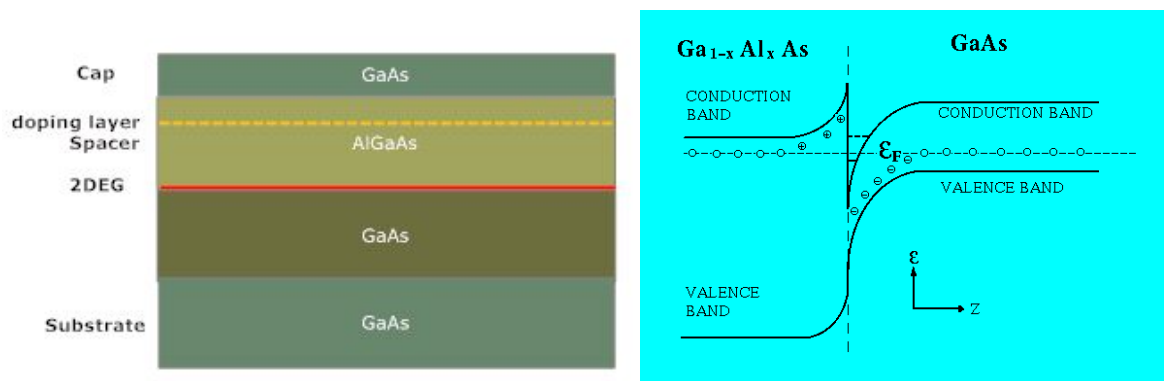
Figure 2.2 : The GaAs/AlGaAs Heterostructure (left) and band structure (right)
(taken from http://www.pha.jhu.edu/~qiuym/qhe/node3.html)

2.3   2DEG in a Perpendicular Magnetic Field

The density of states (DOS) of 2DES is a constant $\frac{m_e^\star}{\pi\hbar^2}$. When placed in an uniform

and perpendicular magnetic field, electrons (or holes) follow cyclotron motion because

of Lorentz force. The cyclotron frequency is

$$\omega_C = |\frac{eB}{m_e^\star}|$$

and the cyclotron radius is

$$R_C = \frac{\upsilon}{\omega_C} = \frac{\sqrt{2m_e^\star E}}{|eB|}$$

, where B is the magnitude of magnetic field, υ is velocity of electrons, and E is the

kinetic energy.

In Landau gauge, vector potential of a magnetic field is $\overrightarrow{A} = (0, Bx, 0)$, so, we

have Schrödinger equation,

$$\left\{\frac{1}{2m_e^\star}\left[-\hbar^2\frac{\partial^2}{\partial x^2} + \left(-i\hbar\frac{\partial}{\partial y} + eBx\right)^2 - \hbar^2\frac{\partial^2}{\partial z^2}\right] + V(z)\right\}\phi\left(\overrightarrow{R}\right) = E\phi\left(\overrightarrow{R}\right)$$

or

$$\left[-\frac{\hbar^2}{2m_e^\star}\nabla^2 - \frac{ie\hbar Bx}{m_e^\star}\frac{\partial}{\partial y} + \frac{(eBx)^2}{2m_e^\star} + V(z)\right]\phi\left(\overrightarrow{R}\right) = E\phi\left(\overrightarrow{R}\right)$$

, where $V(z)$ is the confinement potential to trap 2DEG and does not influence the

electron motion in $x - y$ plane, $\overrightarrow{R} = (x, y)$. Therefore, we can remove $V(z)$ from

above equations. Because $\overrightarrow{A}$ depends only on x, the wave function can be rewritten

as $\phi\left(\overrightarrow{R}\right) = u\left(x\right)exp(iky)$ and we have,

$$\left[-\frac{\hbar^2}{2m_e^\star}\frac{d^2}{dx^2} + \frac{1}{2}m_e^\star\omega_C^2\left(x + \frac{\hbar k}{eB}\right)^2\right]u\left(x\right) = \varepsilon u\left(x\right)$$

Consequently, the energy levels are

$$\varepsilon_n = (n + \frac{1}{2})\hbar\omega_C$$

$$n = 0, 1, 2...$$

, and the wave functions are

$$\phi_{nk}\left(x, y\right) \propto H_{n-1}\left(\frac{x - x_k}{l_B}\right)exp\left[-\frac{\left(x - x_k\right)^2}{2l_B^2}\right]exp\left(iky\right)$$

, where $l_B = \sqrt{\frac{\hbar}{m_e^\star\omega_C}}$ is the magnetic length. More details can be found in [1]

It is interesting to note that the energy levels are only determined by n . These energy levels are named as Landau Levels (LLs). The DOS changes from a constant in Figure2.3 a) to modulated values with maxima corresponding to ε_n, as shown in Figure 2.3b). The LLs have an energy spacing $\hbar\omega_C$. With increasing magnetic field B, the LLs spacing increases and the filling factor ν, which is the number of filled LLs, decreases; while Fermi level E_F passes through maxima and minima of DOS periodically, which results in oscillations in magnetoresistance. This kind of oscillations is called Shubnikov-de Haas (SdH) oscillations, as shown in red trace in

Figure2.4. For high ν, spin up and down states are degenerate and for $\nu \leq 5$, the degeneracy is lifted, as illustrated in Figure2.4.

The blue line in Figure 2.4 shows IQHE[8].The hall slope is $R_H = \frac{1}{n_e e}$, with n_e the density of electrons. The plateau corresponds to the valley of SdH and the transition from plateau to plateau corresponds to the peak of SdH. At each plateau, the resistivity is $\rho = \frac{R}{\Box} = \frac{1}{\nu} \frac{\hbar}{e^2} = \frac{25.8k\Omega}{\nu}$, with $\Box$ the square number of a hall bar.

In reality, 2DEG is not ideal gas. Disorders, including impurities as well as defects, and long range potential arising from the dopant layer influence transport properties of 2DEG. For example, the existence of disorders plays an important role in localized states, which is the origin of the plateaus in IQHE. Disorders also influence mobility μ, an important parameter in 2DEG. $\mu = \frac{e\tau}{m}$, where m is the carrier mass andτ is the transport scattering time.

2.4   Magnetotransport Experiment for 2DEG

As we can see from previous introduction, amazing phenomena show up in magnetic fields for 2DEG. The typical experiment setup is in the following in Figure 2.5. 2DEG samples usually are prepared with lithography techniques to achieve ohmic contacts, regular patterns, and robust gates to become controllable devices. Low temperature, around 300mK, is another condition for 2DEG samples to reach its maximum performance. Because at this low temperature, lattice vibration is negligible and therefore, 2DEG could be treated as ideal gas in approximation, while the perturbations are
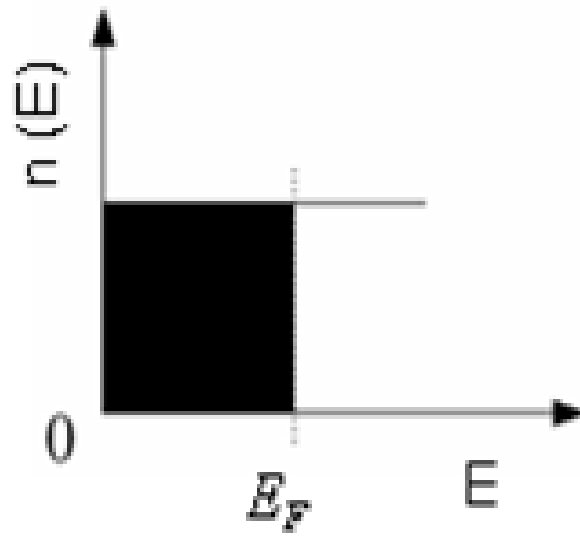
(a)
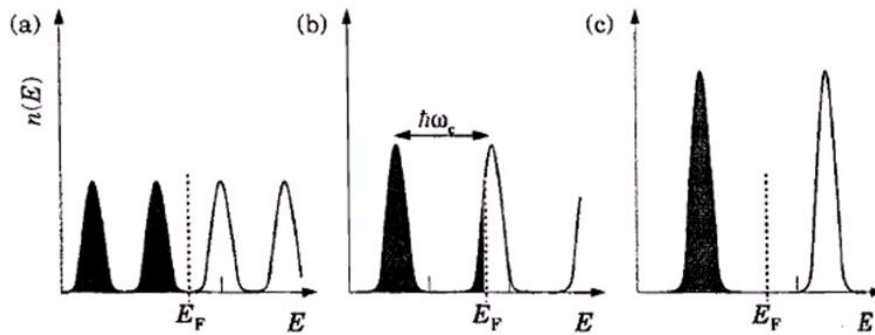
(b)

Figure 2.3 : DOS of 2DEG a: DOS of 2DEG without magnetic fields applied. b: DOS of 2DEG with magnetic fields applied. The magnetic field increases from (a) to (c). (from ref.[1])
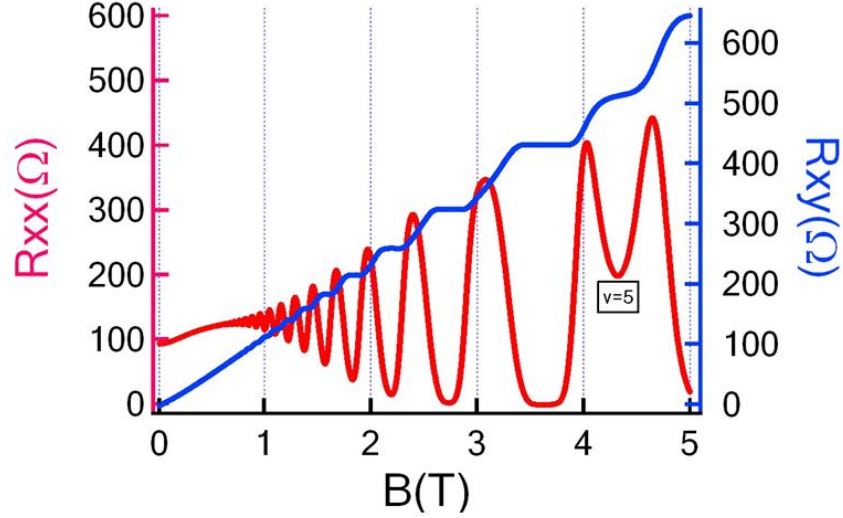
Figure 2.4 : Magnetoresistance in 2DEG in a InGaAs/ InAlAs V5 sample. Red line stands for SdH with its resistance axis on the left and Blue line is for IQHE with its resistance axis on the right. The spin degenerated in high filling factors and its splitting starts from the filling factor $\nu = 5$ as in the figure.

from disorders and lattice vibrations. A standard magnetotransport trace is shown in Figure 2.4.

2.5   Zener Tunneling in 2DEG

With high DC current I_{dc} applying through a 2DEG hall bar, a new set of resistance oscillations was found in very low magnetic fields in Figure2.6 a) by Dr. Yang [2]. The periods of the oscillations are $B_l \propto \frac{I_{dc}}{wl}$, where $l = 1, 2, 3...$ is the order of peaks and w is the width of the Hall bar. The large DC current increases hall field, with which LLs are titled. The titled LLs then provide additional channels for electrons to hop as shown in Figure 2.6 b). Energy conservation rule must be followed and therefore, we have $\hbar\omega_C$At $\triangle Y = Y - Y' = \frac{l\hbar\omega_C}{eE_y} \sim 2R_C$, two wave function overlapped and

<center>(a)   (b)</center>
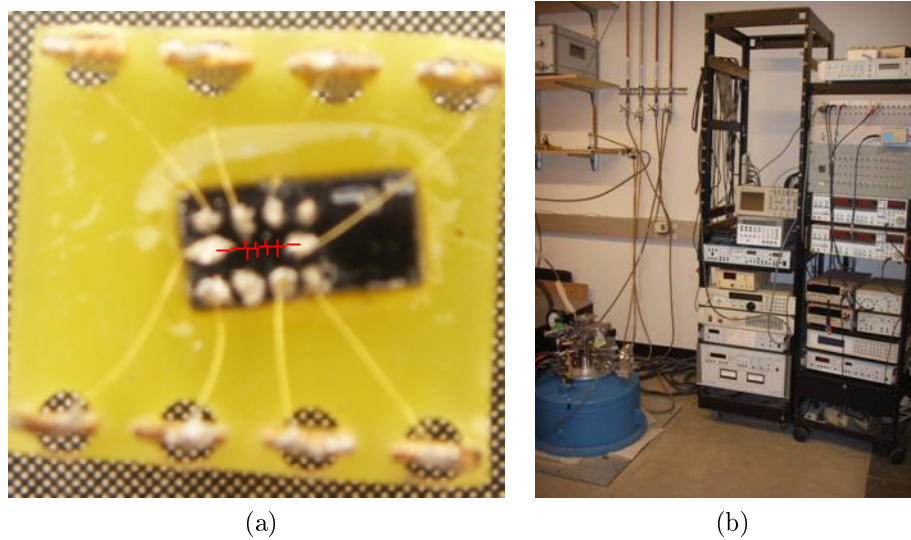
Figure 2.5 : Basic experiment setup. a) Finished 2DEG sample for quantum transport. The bottom part is the chip carrier. The black part is the sample with fabricated hall bar and indium contacts. Gold wires are used to connect the sample and the chip carrier. b)Low temperature measurement setup overview. On the left ground is a low temperature Dewar with magnet inside and on the two racks on the right, are the equipments of measurement.

hopping probability goes to maximum but when $\triangle Y > 2R_C$, the hopping probability drops quickly so does the magnetoresistance.

2.6 Microwave Experiment: MIRO and Magnetoplasmon

2.6.1 MIRO

MIRO was discovered by Dr. Zudov[13, 3]. Magnetotransport shows resistance oscillations with $\frac{1}{B}$ period for high mobility samples irradiated by microwave, as illustrated in Figure2.7. The peak orders are defined as $\varepsilon = \frac{\omega_{MW}}{\omega_c}$ with ω_{MW} the frequency of microwave and ω_C the cyclotron frequency.

MIRO can be explained by electrons jump between LLs with the assistance of disorders after excited by microwave. The momentum change of electrons at peaks is $\triangle q = 2k_F$, where k_F is the Fermi wave vector[13]. Some theorist also proposed equations to approximately describe MIRO[22, 23].

In addition to MIRO, from Fig.2.7, ZRS have shown between $\varepsilon = 1$and $\varepsilon = 2$. Resistance becomes zero in this regime, or in some situations, it does not come to absolute zero but to a small value near zero[3, 15]. This kind states is ZCS as late found by Dr. Yang [16]. Amazed by this dissipativeless effect, a lot of theories were proposed, among which there are two major ones 1) the domain model and 2) the displacement model. In the first one, currents circulate inside domains anti-paralleled to each other and therefore show zero current to outside[24, 25]. The second model tells impurity scattering plays an important role in MIRO and induces the transitions
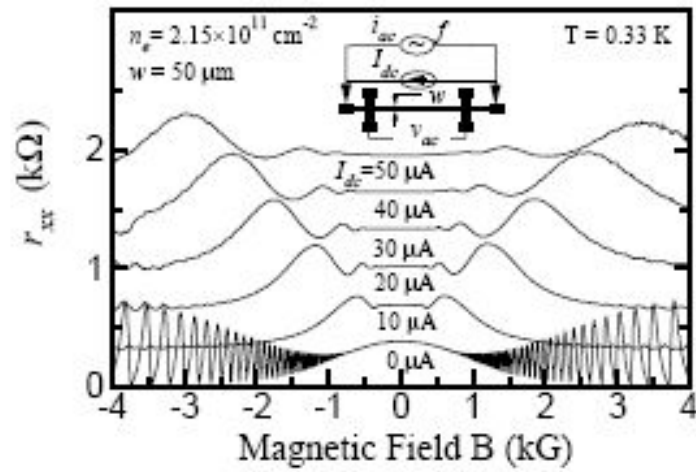
(a)
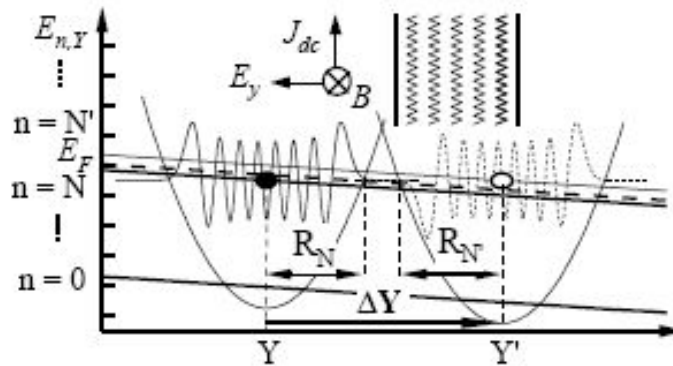
(b)

Figure 2.6 : Zener tunneling in 2DEG a) The measured differential magnetoresistance traces at various dc currents I_{dc} are shown. Up to three orders of oscillations are clearly seen and the inset is differential resistance measurement setup. b) The LLs are spatially tilted along y direction and the Fermi level has the same slope as the LLs. Figures and captions are from [2].
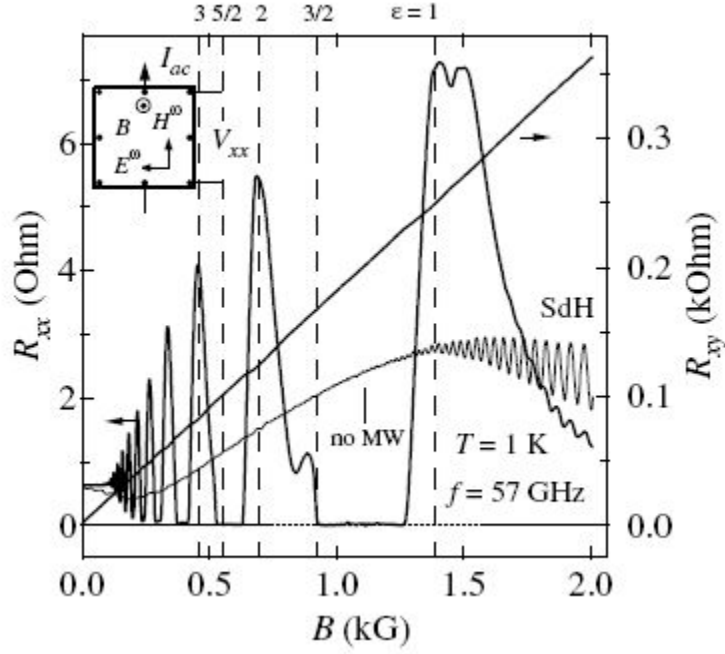
Figure 2.7 : MIRO as well as ZRS (taken from [3])

between different LLs. Because of that, conductivity largely reduced and even goes to zero[26].

2.6.2   Magnetoplasmon

Magnetoplasmon happened very often with the illumination of microwave in a finite size hall bar or a dish structure. the plasma frequency is [27, 28]

$$\omega = \sqrt{(n\omega_C)^2 + \omega_0^2}$$

, where $\omega_{MW} = 2\pi f_{MW}$ is the MW frequency, $\omega_C = eB/m^*$ is the cyclotron frequency, $\omega_0 = \sqrt{n_e e^2 q / 2\epsilon\epsilon_0 m^*}$ is the 2D plasmon frequency, ϵ is the effective dielectric constant ($\epsilon = 6.9$ for GaAs), and $q = \frac{\pi}{w}$ is the plasma wave vector with w the width and n the
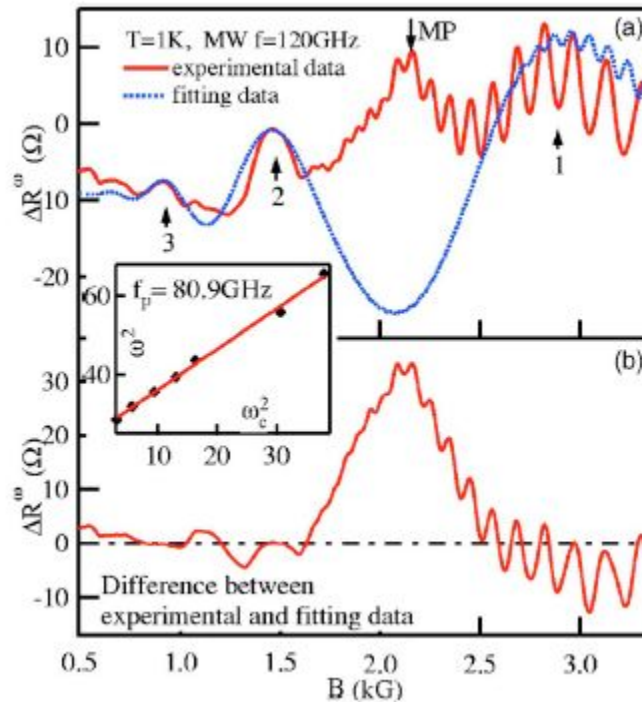
Figure 2.8 : a) Magnetoplasmon labeled as MP. The Red trace is magnetoresistance including MIRO and MP. The blue trace is the numerical fitting data of MIRO in f=120GHz. [4] b) The trace represents for the differences between magnetoresistance and the fitting data.

order of magnetoplasmon. A typical magnetoplasmon peak is shown in Figure 2.8.

When microwave is strong, more high order cyclotron motions are involved in, which

results in high order magnetoplasmon. Because magnetoplasmon does not depend on

electron wavevector, it is not suppressed by an inplane magnetic field [29].

2.7   AB Effect

AB effect is a quantum mechanical phenomenon in which an electron is affected

by the complex phase of the electromagnetic potential instead of the force of an

electronmagnetic field. It is usually demonstrated in an interference experiment such
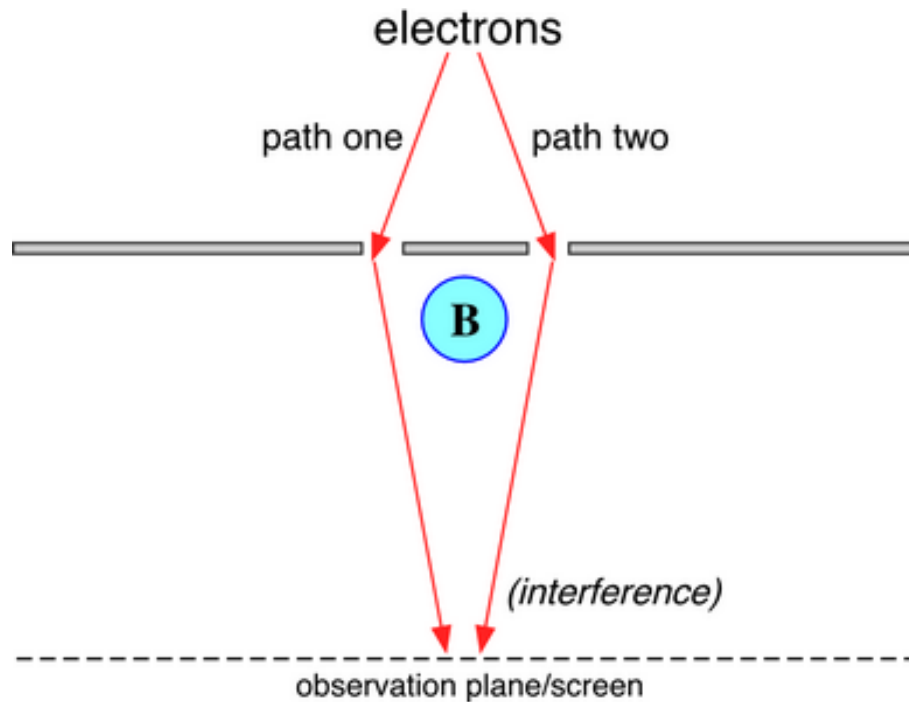
Figure 2.9 : AB effect in a double slit interference exper-
iment with a magnetic solenoid (Picture is from wikipedia
http://en.wikipedia.org/wiki/Aharonov%E2%80%93Bohm_effect).

as in a magnetic solenoid experiment as shown in Figure 2.9.

In the magnetic solenoid experiment, magnetic field B only exists inside the

solenoid. Outside the solenoid, B=0, nevertheless, the magnetic field potential $\overrightarrow{A} \neq 0$.

According to the quantum mechanics without the solenoid, the phase difference

of the two beams should be the same since they originate from the same source [30].

$$\frac{p^2}{2\mu}\varphi_0(\overrightarrow{r}) = E\varphi_0(\overrightarrow{r})$$

$$\varphi_0(\overrightarrow{r}, t) = \varphi_0(\overrightarrow{r})e^{-iEt/\hbar}$$

At any point on the screen, the total amplitude is the sum of amplitudes from

both loops.

With the solenoid,

$$\overrightarrow{p} \rightarrow \overrightarrow{p} - \frac{e}{c}\overrightarrow{A}$$

Thus,

$$\frac{(\overrightarrow{p} - \frac{e}{c}\overrightarrow{A})^2}{2\mu}\varphi(\overrightarrow{r}) = E\varphi(\overrightarrow{r})$$

$$\varphi(\overrightarrow{r},t) = \varphi(\overrightarrow{r})e^{-iEt/\hbar}$$

Or

$$\varphi(\overrightarrow{r}) = e^{\frac{ie}{\hbar c}\int_0^r A(r')\cdot dr'}\varphi_0(\overrightarrow{r})$$

Therefore, the amplitude at one point c on the screen is

$$f_c = exp\left\{\frac{ie}{\hbar c}\int_{a,1}^c \overrightarrow{A}\cdot dl\right\}f_1^{(0)}(c) + exp\left\{\frac{ie}{\hbar c}\int_{a,2}^c \overrightarrow{A}\cdot dl\right\}f_2^{(0)}(c)$$

$$= exp\left\{\frac{ie}{\hbar c}\int_{a,1}^c \overrightarrow{A}\cdot dl\right\}\left\{f_1^{(0)}(c) + e^{\frac{ie}{\hbar c}\oint \overrightarrow{A}\cdot dl}f_2^{(0)}(c)\right\}$$

$$e^{\frac{ie}{\hbar c}\oint \overrightarrow{A}\cdot dl} = e^{\frac{ie}{\hbar c}\iint(\nabla\times\overrightarrow{A})\cdot dS} = e^{\frac{ie}{\hbar c}\phi}$$

ϕ is the phase factor which influences the position of the interference peaks and

valleys, and the magnetic flux inside the loops 1 and 2 .
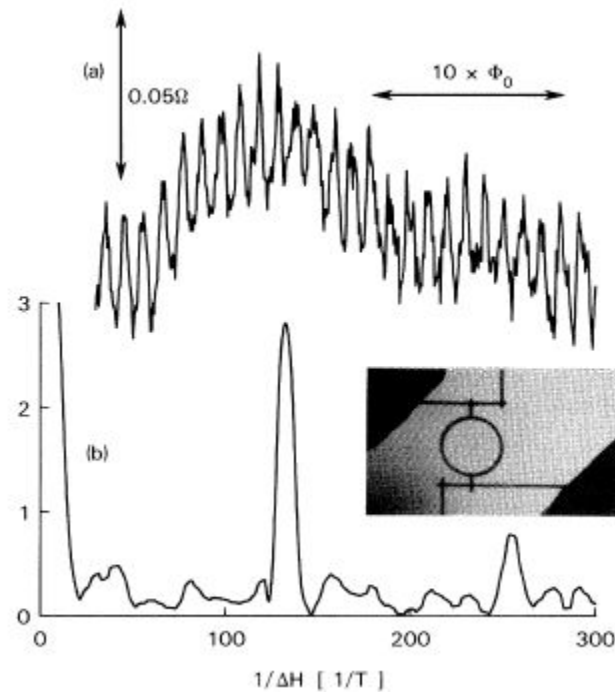
Figure 2.10 : AB effect in a normal metal ring. (a) Magnetoresistance of the ring measured at T = 0.01 K. (b) Fourier power spectrum in arbitrary units containing peaks at $\hbar/e$ and $\hbar/2e$. The inset is a photograph of the larger ring. The inside diameter of the loop is 784 nm and the width of the wires is 41 nm. Taken from ref. [5]

AB effect has been found in many other interference experiments, especially in the ring structures.

In the Au rings with a sub-micron diameter, magnetoresistance oscillations have been observed with a period of $\hbar/e$, which is the first observation of AB effect in a normal metal ring [5] as shown in Figure 2.10.

In the quantum hall regime , AB effect has also been observed, by M. Kato et. al in an antidots lattice patterned hall bar. The period is $\hbar/2e$ and the phenomenon was observed in the vicinity of $\nu = 2$ quantum hall state[6].
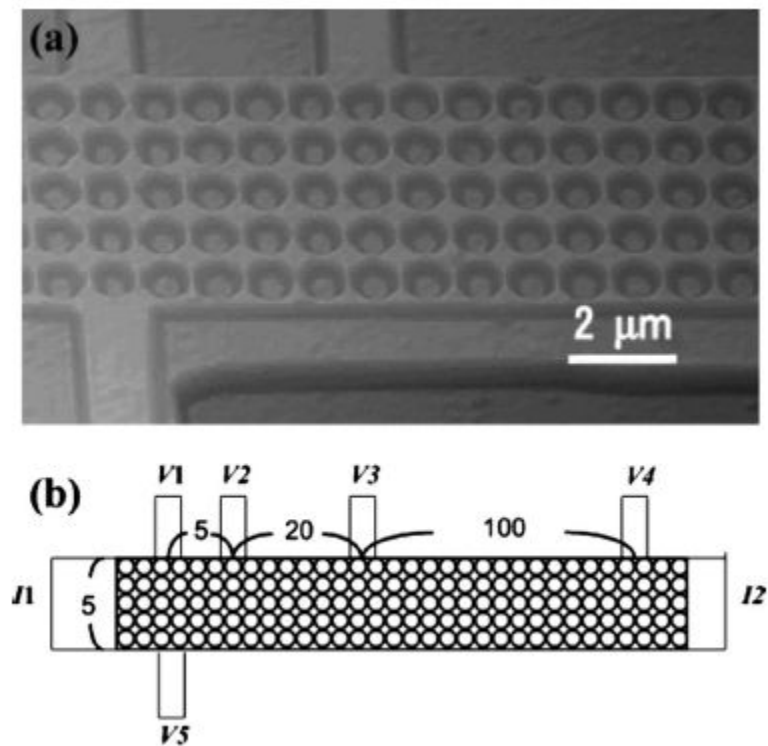
Figure 2.11 : AB effect in the quantum hall regime(a) An atomic force microscopy image of the hall bar sample with the antidots lattice. (b) The probe assignment of the sample (the width of the hall bar is $5.3\mu m$). Taken from ref.[6]

Chapter 3

Microwave Irradiated Magnetotransport in an Ultra-high Mobility Two Dimensional Electron Systems

3.1 The Cyclotron Harmonic Spike in Two Dimensional Electron Systems

3.1.1 Experiments

3.1.1.1 Sample Characterization

We have observed the cyclotron harmonic spike in many samples, however, here we only focus on three samples. All samples are $GaAs/Al_xGa_{1-x}As$ quantum wells (QWs) with width w and spacer distance d, as listed in the Table 3.1 .

Sample A is a GaAs/AlGaAs 30 nm QW with a low electron density of $3 \times 10^{11} \text{cm}^{-2}$ and the mobility is about$3 \times 10^7 \text{cm}^2/\text{V} \cdot \text{s}$. This ultra-high mobility indicates that there are less scatterer in 2DEG than usual high mobility samples, which leads to more inhomogeneity in this sample. There are two subbands in the QW, one has a population about $2.88 \times 10^{11} \text{cm}^{-2}$ and the other has a population about $0.08 \times 10^{11} \text{cm}^{-2}$.

Multisubband may be one of the reasons for the inhomogeneity of the sample. Based on the relationship of mobility $\mu = \frac{e\tau_{tr}}{m^\star}$, $\tau_{tr} \sim 1088\,ps$, and the MIRO result,

$$\Delta R = 4R_0 X(T) exp(-\pi/\omega_c \tau)$$

[31] , we can deduce that $\tau_{\mathrm{MIRO}} = 20\,\mathrm{ps}$. Meanwhile, the estimation of τ_{SdH} can be inferred from the onset of the SdH oscillation $\omega_c \tau_{\mathrm{SdH}} \sim 1$, which is around 3ps and much smaller than τ_{MIRO} . Here τ_{SdH} is underestimated because of the inhomogeneity [32]resulting from the electron density deviation and lack of impurities. Furthermore, $\tau_{\mathrm{MIRO}}$is more reliable to the present scattering time in the sample with B and MW. The ratio$\frac{\tau_{\mathrm{tr}}}{\tau_{\mathrm{MIRO}}} \sim 55$, and the estimate of the scattering angleφ is around 24 according to $\frac{\tau_{\mathrm{tr}}}{\tau_{\mathrm{MIRO}}} \sim \left(\frac{180°}{\varphi} \right)^2$, which indicates that small angles scattering dominates in the sample. All above parameters are consistent with the ultra-high mobility features. A hall bar was fabricated with a standard photolithography technique, with the width around $90\mu m$ and the length around $1000\mu m$.

The same phenomenon has also been observed in another GaAs/AlGaAs 25nm QW sample B, with an electron density of $4.2 \times 10^{11}\mathrm{cm}^{-2}$ and the mobility of $1.2 \times 10^7\mathrm{cm}^2/\mathrm{V} \cdot \mathrm{s}$. Under the same method of sample A, sample B gives a result of $\tau_{\mathrm{tr}} \sim 480\,\mathrm{ps}$, $\tau_{\mathrm{SdH}} \sim 2.2\,\mathrm{ps}$, and $\tau_{\mathrm{MIRO}} \sim 15\,\mathrm{ps}$. The Hall bar width is $180\mu m$, with a length about $1000\mu m$.

Sample C with an electron density of $n_e = 6 \times 10^{11}cm^{-2}$ and a mobility of $\mu \sim 8.6 \times 10^6 cm^2/Vs$ was used to make the comparison. Only MIRO and ZRS were observed in the sample, but not with the new peak.

Base parameters in these three samples are listed in table3.1.

$GaAs/Al_xGA_{1-x}As$	x	QW w	Spacer d	Electron Density	Mobility
sample A	0.24	30nm	80nm	$3 \times 10^{11} \text{cm}^{-2}$	$3 \times 10^{7} \text{cm}^2/\text{V} \cdot \text{s}$
sample B	0.24	25nm	80nm	$4.2 \times 10^{11} \text{cm}^{-2}$	$1.2 \times 10^{7} \text{cm}^2/\text{V} \cdot \text{s}$
sample C	0.3	20nm	30nm	$6 \times 10^{11} cm^{-2}$	$8.6 \times 10^{6} cm^2/Vs$

Table 3.1 : Sample parameters

3.1.1.2 Sample preparation

All samples were fabricated into hall bar shape with a width of $90\mu m$ or $180 \ \mu m$. The contacts on hall bars were all made from Ge/Pd/Au alloy, a receipt ensuring perfect ohmic contacts on GaAs. Typical photolithography methods and metal deposition processes were employed during hall bars and contacts fabrication . More details could be found in Appendixes in [33] .

3.1.1.3 Experiments Setup

This experiment was running in a He-3 refrigerator with a base temperature 300mK. Microwave (MW) was sent from top through a waveguide inside the test probe and shines upon the sample. The magnetic field, the sample and the MW were in a Faraday Geometry. High frequency MW (50-150GHz) was produced by Gunn diode oscillators. (see Figure3.1) We also used a piece of InSb as a bolometer, and placed the InSb underneath a QW, which is from the same wafer of the sample A and has a dimension of $3mm \times 5mm$, to calibrate absorption peaks position of sample A in a cyclotron resonance experiment. The magnetic field was carefully calibrated by a

Gauss meter and all MW frequencies smaller than 120GHz are measured by a remote sensor and a MW counter.

3.1.2 Results

We have observed a sharp spike superposing on top of the MIRO peak. In Fig.3.2, the spike occurs around 1.21kG and it is at the half of the cyclotron resonate magnetic field, $\frac{\omega_f}{\omega_c} = 2$. SdH oscillations are not very strong till around 2.3 kG. This spike is different from the common phenomena MIRO in MW irradiation and has much narrower width and much stronger intensity. To describe the spike quantitatively, we define it as an extra part from the top of the $\varepsilon = 2$ MIRO peak. The width is defined by full width at a half maximum (FWHM) of the extra part. The width of this spike is much narrower than FWHM of the MIRO peaks and normally has ranges from 20G (0.042K) to 100G (0.21K). With the MW power and the sample space temperature vary at different frequencies, we cannot summarize any trend for height and width of the spike for frequency dependence, but generally speaking, the spike favors high frequencies (>100GHz). At frequency 103.08GHz in the Fig 3.2, the amplitude is as high as 300% of the MIRO. The width is about 0.026kG at this frequency, which leads to amazing high quality factor, $Q = \frac{B}{\triangle B}$ 50.

The absorption signal from CR experiment on sample A indicates that there is strong absorption peaks around $\omega = \omega_c$, one with effective mass $m^\star \sim 0.066$ and the other with $m^\star \sim 0.069$. $m^\star \sim 0.066$ is very close to effective mass previous reported
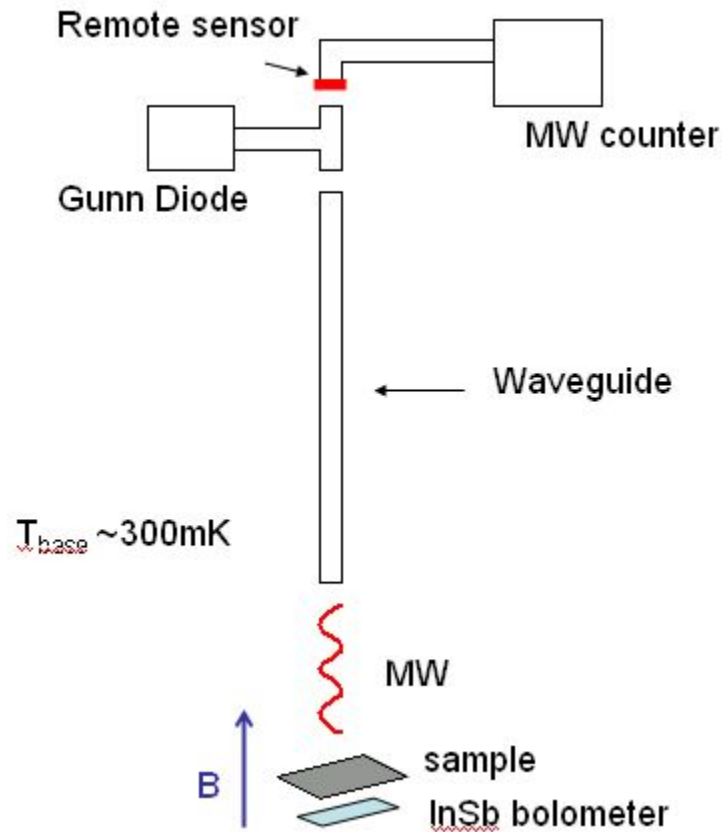
Figure 3.1 : The illustration of the experiment setup. The whole setup is placed in a He-3 cryogenic with a base temperature of 300 mK. A vertical (to sample surface) probe is used equipped with electrical circuits and a waveguide. Samples (with a bolometer underneath in a CR experiment) are put onto a chip carrier and located in the center of the magnetic field. A vertical magnetic field is generated in a super-conducting magnet with a range from 0 to $\pm 10T$. MW is produced from a series of Gunn diode oscillators with a range from 50GHz to 150GHz and the power produced by Gunn diodes varies for different frequencies. A remote sensor connecting to a MW counter is set aside to measure the real frequency of MW.

and $m^\star \sim 0.069$ is probably from electrons in the AlGaAs layer. At $\omega = 2\omega_c$, we did not see any absorption signal within experiment limit but in the other experiment which we conducted in lab later in 4K with Cernox thermometer, a strong absorption single as this frequency has been seen by Aeron et al..

This spike occurs in many other samples. In some previous published data related to MIRO, the indication of this spike also has been found[29]. So, this phenomenon is universal in 2DEG system with MW and magnetic field presence but it favors high mobility.

In Fig.3.2, the experimental data at MW frequency 117.59GHz is fitted with the theoretical expression in ref.[23] ,

$$\Delta\rho_{xx}\left(B\right) = A \int d\epsilon \left[n_F\left(\epsilon\right) - n_F\left(\epsilon + \hbar\omega_c\right)\right] \nu\left(\epsilon\right) \partial_\epsilon \nu\left(\epsilon + \hbar\omega_c\right)$$

, here

$$n_F\left(\epsilon\right) = \frac{1}{1 + \exp\left(\frac{\epsilon - \epsilon_F}{k_B T}\right)}$$

is Fermi distribution function and

$$\nu\left(\epsilon\right) = \sum \frac{\left(\frac{eB}{\pi^2 \hbar \Gamma}\right)}{\left\{1 + \frac{\left[\epsilon - \left(i + \frac{1}{2}\right)\hbar\omega_c\right]^2}{\Gamma^2}\right\}}$$

is DOS . A is the scaling factor for amplitude.$\epsilon_F = 15mev$ and$T = 0.4K$ are experimental parameters. The experiment trace $\Delta\rho_{xx}$was taken with a double modulation
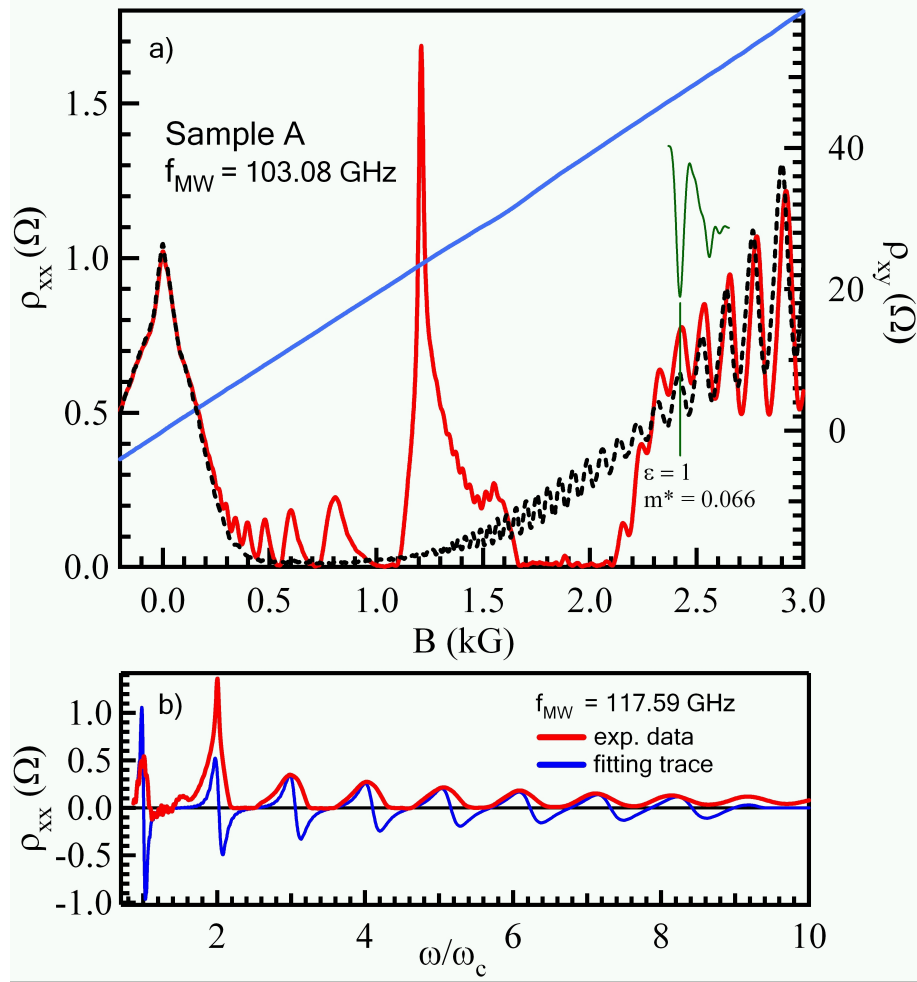
Figure 3.2 : a) Those were traces taken at $f_{MW} = 103.08GHz$. The spike on top of the MIRO peak as shown in a red solid line. The dot black line shows magnetotransport without MW irradiation. The dot blue line is the Hall trace. The dash black curve on top of MIRO is the absorption trace, and deduced from deeper dip, the effective mass with MW is $0.066m_e$ in sample A. b) MW resistance response versus MIRO orders. The red solid line is the experimental trace at $f_{MW} = 117.59GHz$. The dot line is the simulation using the same parameters (frequency f_{MW}, temperature T, Fermi energy ϵ_F, and etc.) in experiment.

technique, which uses another low frequency MW to modulate major MW in order to get net resistance response at frequency of major MW . For $\frac{\omega_f}{\omega_c} > 2$, amplitude and magnetic field position of MIRO peak fit very well with theory. At $\frac{\omega_f}{\omega_c} = 2$,we see higher amplitude than MIRO peak. At $\frac{\omega_f}{\omega_c} = 1$, amplitude from the experiment trace looks lower than simulation, because of usual saturation for the first peak. An important parameter is gotten from this simulation: LLs broadening $\Gamma \sim 10\mu eV$ or $\tau \sim \frac{\hbar}{2} \times \frac{1}{\Gamma} \sim 30ps$. The latter is on the same order of scattering time deducing from envelop of experiment traces above.

3.1.2.1 Frequency Dependence

Frequency survey has been conducted in a lager frequency range from 50GHz to 150GHz. This spike is a general phenomenon in a wide range. In Fig.3.3, three traces from different frequencies were listed as examples. If we compare ω_{MW} with measured ω_c of spike,$\frac{\omega_{MW}}{\omega_c} = 2$ with $m^\star = 0.066$ as plotted in the insert of Fig.3.3.

Fig.3.3 also shows us that the quality of the spike in sample A is much better than in sample B, which confirms the mobility or purity of samples does matter in this experiment. As f_{MW} increases, the peak becomes more predominant.

3.1.2.2 Temperature Dependence

In temperature dependence experiment, spike height increases a little bit with increasing of temperature, then decreases above 0.7K (see Fig.3.4). This is because in this sample phonon involves into transport in a very low temperature 1K and thus the
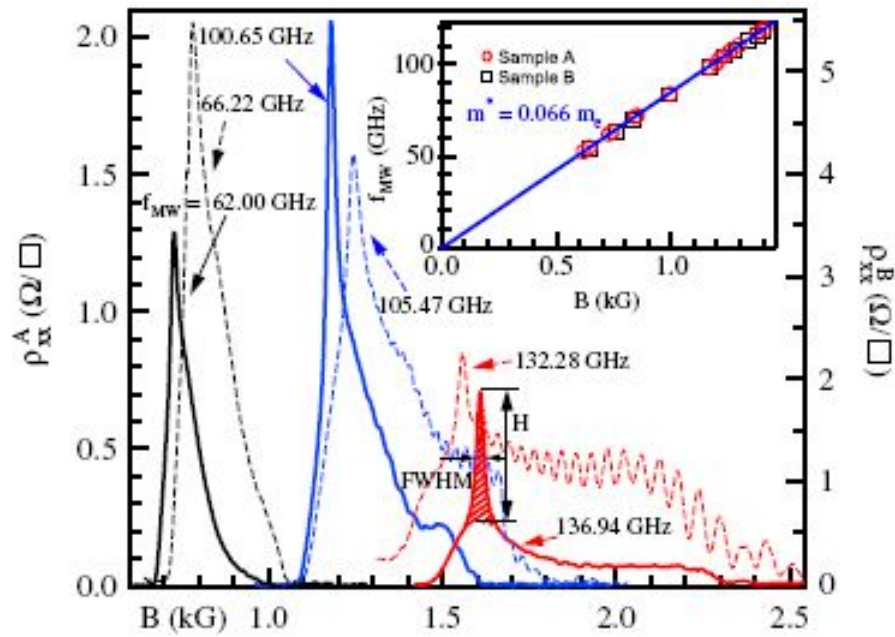
Figure 3.3 : The frequency dependence of the spike is shown for, respectively, sample A (solid lines) and sample B (dashed lines) in f_{MW} between ~60 and ~135 GHz. It is shown that the spike amplitude and width are correlated with the sample mobility. The inset shows a linear relation between the magnetic field position of the spike and the f_{MW}, indicating that the spikes occur at $2\omega_C = \frac{2eB}{m^\star}$, with $m^\star = 0.066m_e$.
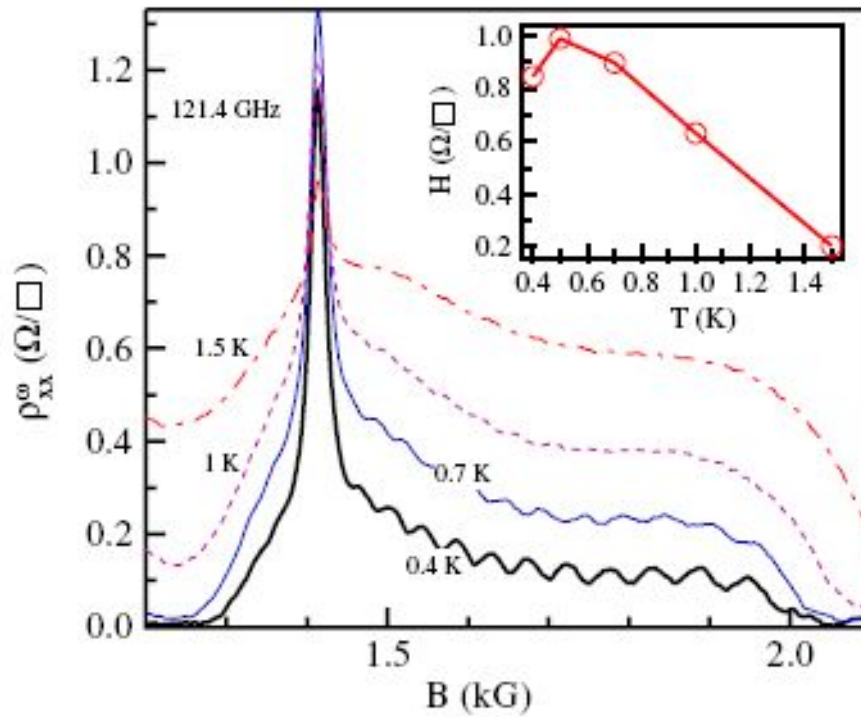
Figure 3.4 : Spikes measured at different temperatures are shown for sample A. Inset: The spike amplitude shows an approximately linear dependence with temperatures. The line is a guide for the eye.

electron transport interferes with the photon assisted transport. Overall, the height of spike is a few times larger than $\varepsilon = 2$ MIRO peak, the maximum spike height to MIRO can reach 7 times with right frequency and power.

3.1.2.3   Power Dependence of the Spike

The MW source was produced by a series of Gunn diodes and the power of MW was attenuated by a mechanical MW attenuator. It is really difficult to measure the power onto the sample as well as photons absorbed by the sample. In our experiment we use He-3 coolant temperatures to roughly represent MW powers.
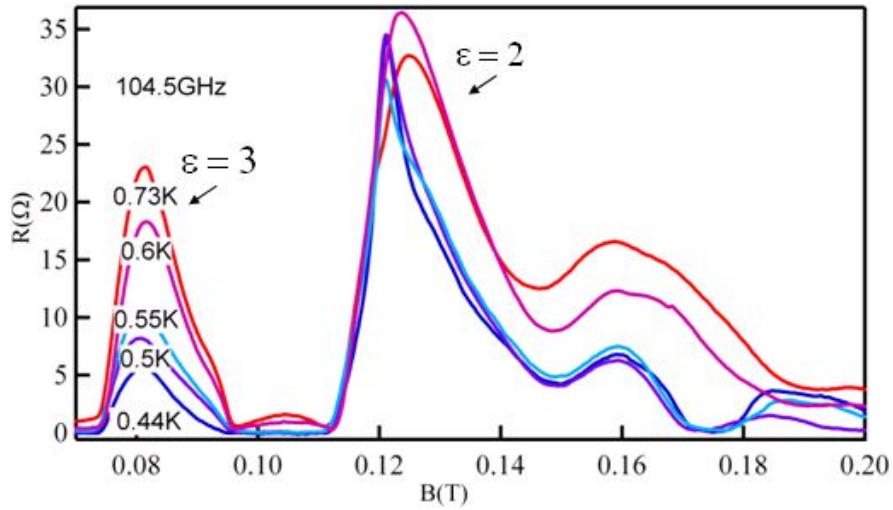
Figure 3.5 : The power dependence of the spike as well as $\varepsilon = 2, 3$ order MIRO at $f_{MW} = 104.5 GHz$. The temperatures labeled are coolant temperatures and used to represent MW powers.

The power dependence of the spike is drawn in the Fig. 3.5. As power increases, the spike height decreases a little bit at 0.55K. Above that Temperature, the effect of spikes has been taken over by $\varepsilon = 2$ MIRO peaks.

3.1.3 Discussion

3.1.3.1 Electromagnetically Induced Transparency

In optical experiments, electromagnetically induced transparency was found to be interference between different virtual processes between final and initial states. Laser was used to couple and probe resonate signals. Similarly, in MW irradiated 2DEG, quantum interference happened when MW was served as a coupling signal.

When a plane electromagnetic wave shines on a sample, for independent electrons,

$$H = \frac{1}{2m}\left(\vec{p} - q\vec{A}(\vec{r},t)\right)^2 + V\left(\vec{r}\right) - \frac{q}{m}\left(\vec{E}\times\vec{B}\bullet\vec{B}\left(\vec{r},t\right)\right)$$

. Dipole transition is from the zero order of $-\frac{q}{m}\left(\vec{E}\times\vec{B}\bullet\vec{B}\left(\vec{r},t\right)\right)$ and $W_{DE} = -qE_0 z cos\omega t$. The selection rule is $\Delta l = \pm 1$. Electron quadruple transition is gotten from the first order term

$$W_{QE} = -\frac{q}{2mc}(yp_z + zp_y)E_0 cos\omega t$$

and the selection rule is $\Delta l = 0, \pm 2$. Normally,$W_{QE} \ll W_{DE}$. In our high mobility 2DEG, with MW shining on top, MIRO is a very common phenomenon from dipole transitions. If the electric field interacts with perpendicular electric field, the quadruple transitions happen with the selection rule $\Delta l = \pm 2$ which means transitions can happen from N to N+2 LLs.

MIRO could be taken as the first order quantum interference as Dr.Dung-Hai Lee proposed[7]. MW coupling creates many different loops between final state and initial states. Only when $\omega_{MW} = \omega_c$, two states coupled have almost the same orbits size and therefore transitions from all loops are in phase, and the total contribution is constructive. Otherwise, deconstruction happens as shown in Fig. 3.6.

The spike could be the second order quantum interference from N to N+2 state. Quadruple transition could be one possible loop, magnetic field induced a cross elec-
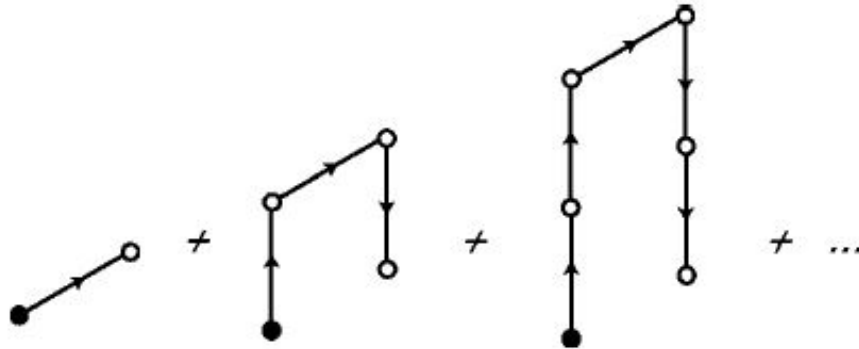
Figure 3.6 : The processes above and their particle-hole inversion analog causes interference. The vertical lines represent absorption or emission of the coupling field photons. The slanted horizontal arrows correspond to the absorption of the probing field photon. The Fig. and its caption are from ref. [7].

tric field spontaneously in 2DEG. But this effect should be way smaller than dipole transition in magnitude and not able to induce such intense spike. The other possible loop could be non-resonate transition from N to N+2 with the assistant of impurities since in low magnetic field, LLs mixing cannot be avoided[28]. N+1 state contains part of N state and part of N+ 2 state. In this case, transition from N state to N+2 state become possible.

High order quantum interference could exist, the 4th, 6th .... Actually we saw some indication in our experiment, see Fig.3.7. Enough electric field is crucial to high order peaks. The possible interference loops between resonate and non-resonate transitions for high orders are probably very similar to the case of the second order.

There is some similar optical experiment [34] has been studied, in which light has been set to certain direction and current was measured in the same direction. The quantum interference resonance current $j \propto \frac{\varkappa}{\delta B}$,$\varkappa$ is the photon momentum and δB
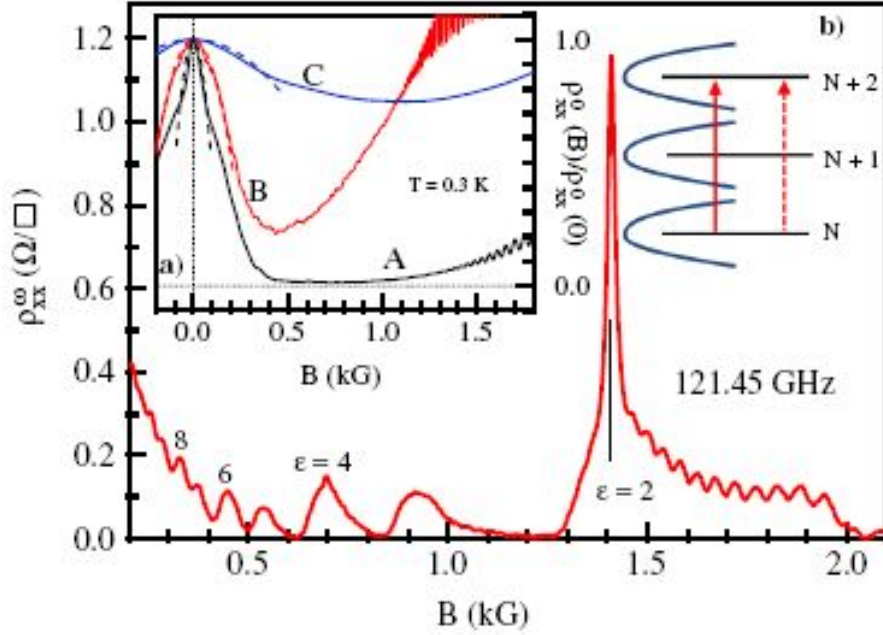
Figure 3.7 : Inset(a): The 3 high-mobility, modulation-doped GaAs/AlGaAs samples(A,B,C) show negative magneticresistance (NMR), as explained by a mechanism of interplay between strong scatterers and smooth disorders. The dashed lines are the asymptotic lines that yield the characteristic frequency ω_0 for the NMR. In addition to the $\varepsilon = 2$ spike, extra peaks can be observed at the high-order even numbers of $\varepsilon(\varepsilon = 4, 6, 8)$ in sample A. Inset (b) is a schematic for cyclotron and quadrupole transitions.

is the deviation from the resonate magnetic field[35]. From our results, generally speaking, the spike favors in a frequency higher than 100GHz. But we have slower decreasing trace than $\frac{1}{\delta B}$. This is because, in our experiment, reflection of MW from metals parts inside sample space will make it to polarize to any direction and the current we measure is an average effect over all directions. But qualitatively, this spike could be considered as a fast decreasing function from the resonate magnetic field compared to other phenomena, such as MIRO.

3.1.3.2   Interference from Random Scatterers

Negative magnetic resistances (NMR) are dominating features in sample A and B (Inset of Fig. 3.7)). The major feature is a strong NMR and a saturation, following after, of magnetoresistance at one value determined by the smooth disorders.

The interplay of two types of disorders were listed to be responsible for NMR. One is randomly distributed hard scatterers, in our samples, very dilute. The other is smooth random potential. The first mainly from the interface defects in our ultra-clean sample and leads to an asymmetric resistance response with respect to negative and positive magnetic field. The second one is from the remote dopant layers.The detail analysis and simulation for this issue can be found in Mirlin et al [36] .

To estimate scatterer density n_S, an asymptotic was drawn by dashed lines,

$$\rho_{xx}(B)/\rho_{xx}(0) = 1 - (\omega_C/\omega_0)^2$$

and it points out the onset of NMR. At the onset of NMR, $\omega_0 = (2\pi n_S)^{1/2}\nu_F(2l_S/l_L)^{1/4}$ is the frequency determined by the interaction of mechanism of two scattering disorders. The transport mean free path of smooth disorders is labeled l_L and of antidots is labeled l_S. We assigned $l_L/l_S \sim 50, 10, 5$ for sample A, B, C. With ω_0 , the density of scatterers , n_S, are $(8\mu m)^{-2}$, $(6\mu m)^{-2}$, $(2.6\mu m)^{-2}$, respectively. From the results, we can see random scatterers on a background potential as we expected. More detail could be found in ref.[37].

3.1.3.3   Magnetoplasmon Effect

The magnetoplasmon (MP) has shown in the magnetoresistance as in the FIG.3.8. The MP location coincides with ZRS.

From the background in Chapter 2, we know the plasma frequency is

$$\omega_{MW} = \sqrt{(n\omega_C)^2 + \omega_0^2}$$

, $\omega_{MW} = 2\pi f_{MW}$ is the MW frequency,

$$\omega_C = eB/m^*$$

is the cyclotron frequency and

$$\omega_0 = \sqrt{n_e e^2 q / 2\epsilon\epsilon_0 m^*}$$

is the 2D plasmon frequency, ϵ is the effective dielectric constant and is 6.9 for GaAs, $q = \frac{\pi}{w}$ is the plasma wave vector with w is the width and n is the order of MP.

For sample A: $\omega_0 = 66.4 GHz$ with $w = 180\mu m$. Fig.3.9 is the magnetic fields of MPs on different MW frequencies in sample A.

In Sample B: $\omega_0 = 113 GHz$ with $w = 90\mu m$, MP signal in this sample is very weak.

The effect of MP on the spike can not be totally ruled out but there is no solid

evidence relating the spike with MP.

3.2 The Spike in an in-plane Magnetic Field

Though the spike can be commonly found in ultra-high mobility samples, the origin of the spike is still a mysterious. As we have proposed some mechanism which may leads to this effect and also discuss more carefully on the unique properties of ultra-high mobility samples, a satisfied answer has not been given to this question. From previous experiment, an in-plane magnetic field has been employed to reduce the effect of MIRO[29], and in the following experiment, the spike survives in high in-plane magnetic fields with zero phase shift.

3.2.1 Experiment

The experiment set is almost the same with previous setup except an in-plane magnetic field added. The in-plane magnetic fields have a range from 0 to $\pm 2T$.

3.2.2 Results

In Fig. 3.10a) , we draw several magnetoresistivity traces with in-plane magnetic fields B_x from 0 to 0.8T and lifted each traces by $2\Omega/\square$. For $2\omega_C$ spikes, no phase shift is displayed even at very high B_x and there is only little drifting in high B_x (red data points in Fig.3.10b)). 2T is a very high magnetic field and one order of magnitude larger than the perpendicular magnetic field of $2\omega_C$ spike, if considering that cyclotron resonance for this sample happened within $B_Z(0-0.3T)$. 2nd harmonic
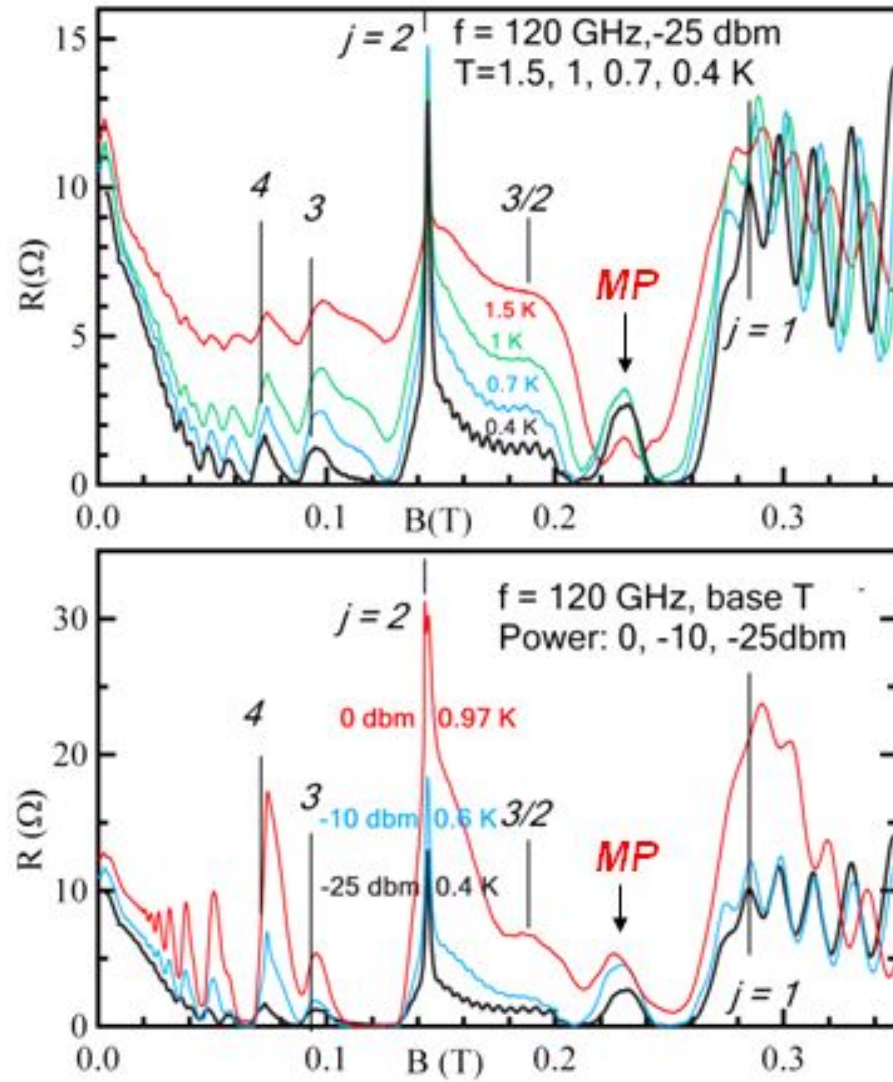
Figure 3.8 : MP shown in resistance traces in sample A as indicated by dark arrows. The top plot: temperature dependence of MP from 0.4K to 1.5 K at attenuation -25dBm. The bottom plot: power dependence of MP from 0 dBm to -25 dBm at base temperature. All traces were taken in $f_{MW} = 120 GHz$.
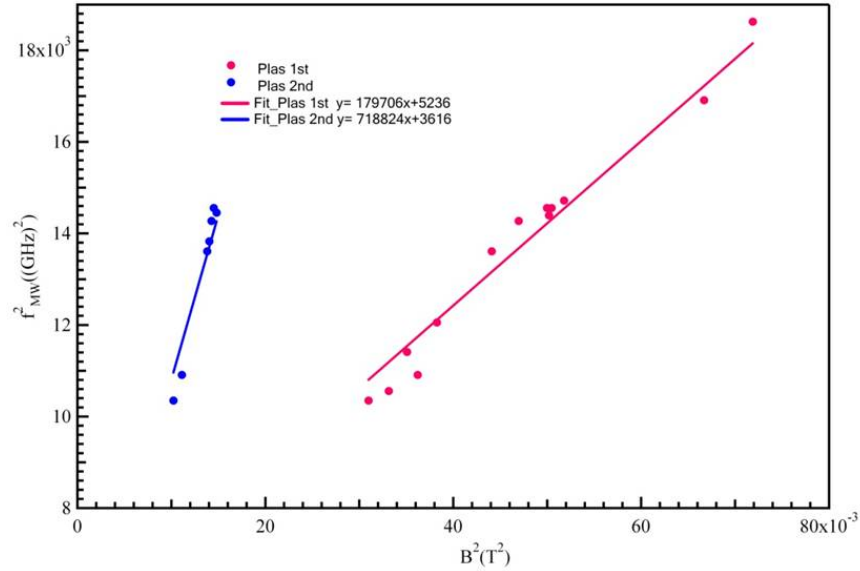
Figure 3.9 : The MP peaks for sample A. For first order MP peak, $B_{plasmon}$ at $fmw = 104.88GHz$ is around 0.18 T. The intercept of fitting line gives first order plasma frequency $72.36GHz$, second order frequency $60GHz$, which is really reasonable value comparing with calculated number $66.4GHz$.

MIRO peaks (Black arrows) have a large phase shift towards smaller ε, which could be seen from both a) and b) in Fig. 3.10. Cyclotron data for both sample A and B are taken and plotted in Fig. 3.10b) and they have almost the same trend of phase shifts.

The amplitude of both $2\omega_C$ spikes and 2nd harmonic MIRO peaks are suppressed by in-plane magnetic fields as they introduce more scattering incidents of electrons with boundary and also with impurities and decrease the mean free path and life time. $2\omega_C$ spikes are a small extra tips on the top of magnetoresistance traces in a very large in-plane magnetic field up to $B_x = 2T$ as seen in Fig.3.11, while 2nd harmonic MIRO's amplitude drops to zero or a negligible value in an in-plane magnetic field above 0.8T. We also noticed that higher order MIRO also shift and damp more quickly than 2nd
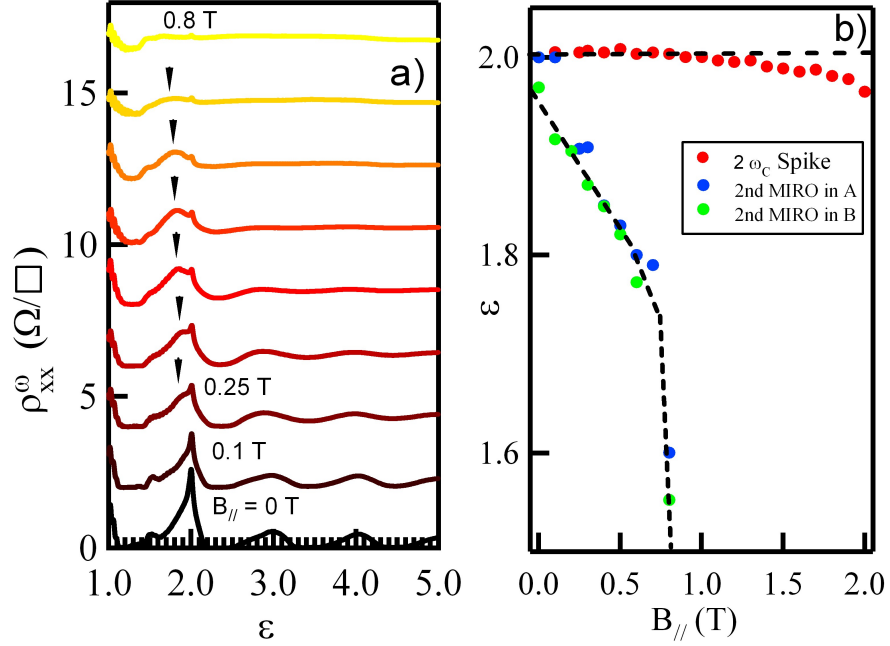
Figure 3.10 : a) Resistivity traces in different in-plane magnetic fields versus ε. All traces except the bottom one were lifted by $2\Omega/\square$. Black arrows point out 2nd harmonic MIRO peaks positions. b) Peaks positions versus in-plane magnetic fields. Red dots show $2\omega_C$ spikes in sample A, blue dots shows 2nd harmonic MIRO peak in sample A, and green dots for 2nd harmonic MIRO peak in sample B. The dash line is the guide for eyes.

order.

An overview map of magnetoresistivity ρ_{xx}^{ω} versus both B_x and B_z is in Fig.3.12 (ρ_{xx}^{ω} amplitudes are represented in color, ZRS is in dark blue area, and $2\omega_C$ peaks in small in-plane magnetic field $B_x < 2kG$ are in red). Single magnetoresistivity versus B_z trace is measured on sample A one by one with certain value of B_x at $f_{mw} = 104.88GHz$ and temperature 0.4K. Then we present them all together in this map to show the trend of the magnetoresistivity change (by interpolating 11 magnetoresistivity $(B_x : 0 - 10kG)$) . When an in-plane magnetic field is zero, the ultra-high resistivity spike,$2\omega_C$ peak , at $\varepsilon = 2$ and coincident with 2nd harmonic
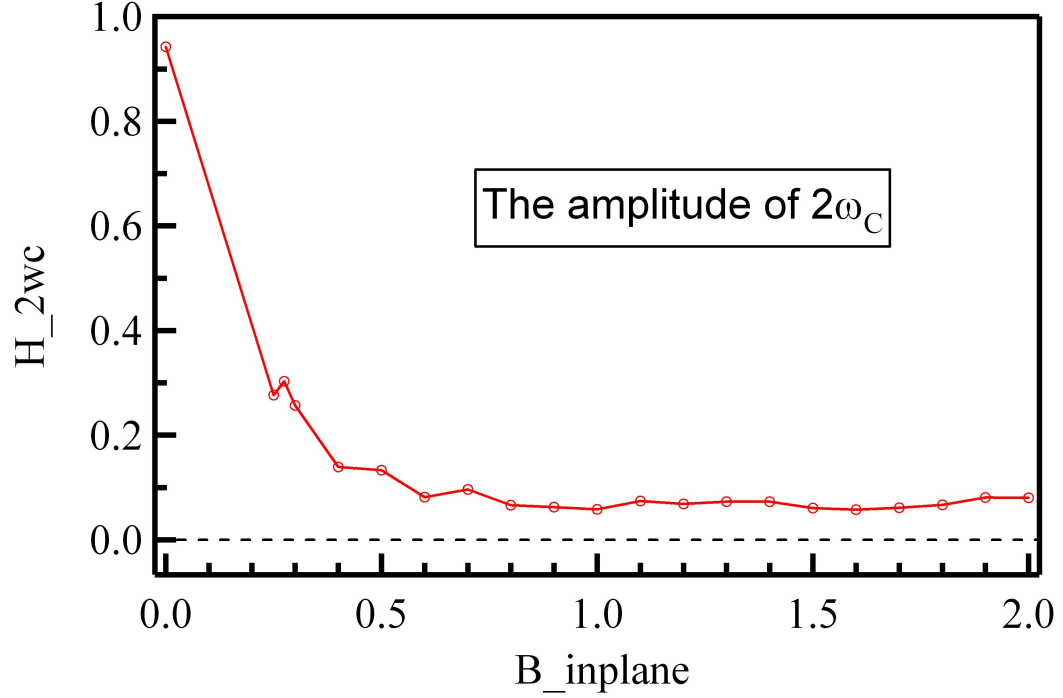
Figure 3.11 : The height of the $2\omega_C$ spike in in-plane magnetic fields

MIRO peak for this ultra-high mobility sample, is shown in a red line with an arbitrary amplitude using the same B axis with traces in resistivity map. Strong $2\omega_C$ peak on this red line is the red area at $B_x = 0kG$ on the lower edge of the map. A straight narrow light color area from $B_x = 0kG$ to $B_x = 10kG$ is shown at $\varepsilon = 2$ with the amplitude from extreme high to relatively high, while the $2\omega_C$ peak sticks at $\varepsilon = 2$ position and only changes in amplitude. Another light color area with the shape like a fish tail, as shown between $B_x : 0 - 6kG$, displays the trend that 2nd harmonic MIRO peak deviates from $\varepsilon = 2$ and towards to $\varepsilon = 1$.

$\varepsilon = 1$ ZRS is also persistent up to 0.7 T in-plane magnetic field while higher order ZRS disappear in smaller B_x. The vanish point of ZRS is linear with the in-plane
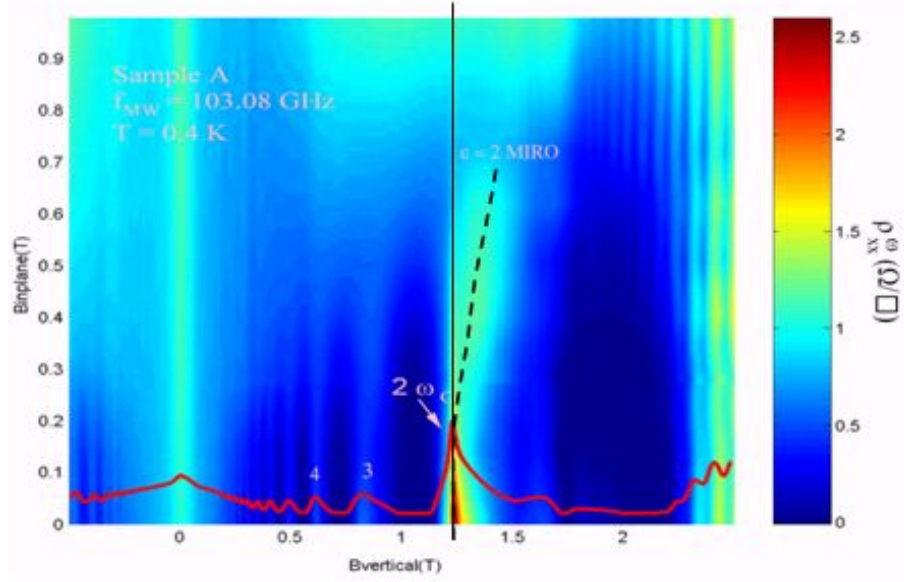
Figure 3.12 : The Resistivity map with B_x and B_z. The Red line is the resistivity trace versus B_z at $B_x = 0kG$. The dark solid line states the locations of $2\omega_C$ peaks and the dark dash line states the shifting tend of 2nd harmonic MIRO peaks.

magnetic field which means stronger in-plane fields were needed to destroy ZRS in higher B_z.

Overall, we observed that $2\omega_C$ peak displayed a zero phase shift in an in-plane magnetic field while MIRO have a very large phase shift as well as amplitude damping. The discrepancy of the development trend of $2\omega_C$ peaks and 2nd harmonic MIRO peaks in a increasing in-plane magnetic fields clearly shows they are two separated phenomena and reveals different mechanisms. In the following, the effect of an in-plane magnetic field on MIRO is discussed.
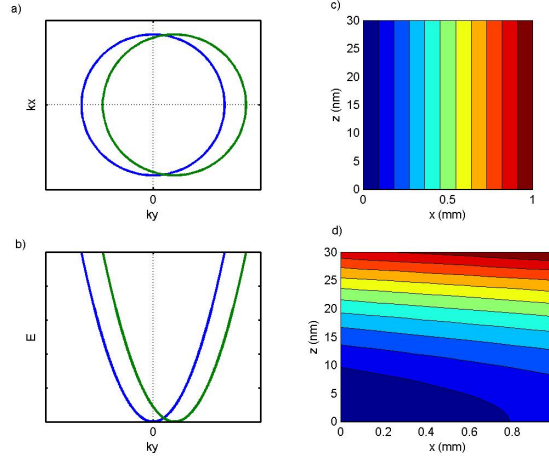
Figure 3.13 : a) Fermi surface drifting. b) Energy dispersion shift according to a). c) Energy gradient in x direction d) Energy gradient in both x direction and z direction

3.2.3 Discussion

The Zeeman splitting could be separated much larger than LLs spacing due to an in-plane magnetic field [38]and reflected on magnetotransport. But in our case, an in-plane magnetic field increases Zeeman energy $\Delta E = g\mu B_x$, is about 150mK, while the LLs spacing is ~ 9 K at $B_x = 5kG$. Therefore,the effect of Zeeman splitting from in-plane magnetic fields is very small.

Due to the confinement Δz, interface scattering changes electrons' motion and increase k_y. $\Delta k_y = \frac{B_x(\Delta Z)e}{\hbar}$. At $\Delta z = 30nm$, $\Delta k_y = 0.024nm^{-1}$ in B_x 5kG. $k_F = \sqrt{2\pi n_e} = 0.137nm^{-1}$, so Δk_y 17.5. Fermi surface drifts with a Δk_y as shown in Fig. 3.13a) with blue circle for at $z = 0$ and green for at other values. This indicates momentum transfer in different Δz, and will cause damping on MIRO.

With in-plane B_x and k_y , an effective electric field $E_z = -v_y B_x$ show in the perpendicular direction with the electric potential energy $\xi_z = v_y B_x e\Delta z = \hbar\omega_x \Delta k_y \Delta z$.
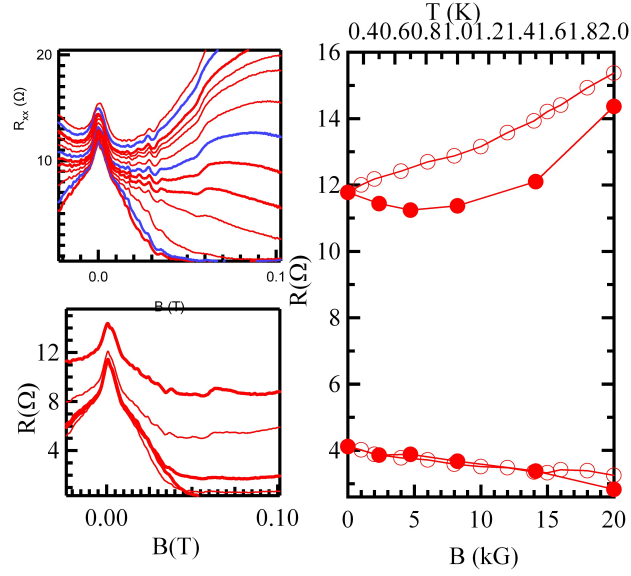
Figure 3.14 : Destroying of weak localization, left top, in different B_x, left down, in different temperatures. Right one: solid red dots for temperature dependence and holy red dots for B_x dependence. top branch in right is the zero B_z magnetoresistance and down branch is the net NMR at $B_z = 0.1kG$.

With $\Delta z = 30nm$, and $B_x = 5kG$, this energy $\xi_z = 0.59meV$ comparable to LLs separation $\Delta\xi_{LL} = 0.82meV$. With applying dc current, $E_x = \frac{I}{Wn_ee\mu}$, and $\xi_x = eE_x\Delta x$. At $\Delta x = 1mm$, $\xi_x = 0.0077meV$. Fig. 3.13 c) is the illustration of the displacement mechanism for MIRO, electrons scatter forward or backward to another LL. Peaks happen when energy change equals to $\Delta\xi_{LL}$. With in-plane magnetic field B_x, energy levels increase as shown in Fig. 3.13 d), $\xi_z = \frac{B_x^2\Delta z^2 e}{\hbar} \cdot \hbar\omega_x$, $\xi_{total} = \xi_{LL} + \xi_z + \xi_x$, $\xi_{LL} = \left(n - \frac{1}{2}\right)\hbar\omega_C, n = 1, 2, 3....$ Electrons take much shorter distance in x direction and can reach another LL. Therefore, the resonance peaks shift to higher magnetic field B_z regime and also induce the damping effect on amplitude of MIRO.

The change of k_y destroys weak localization. With drifting of Fermi surface, the wavevector in a loop and its reverse loop are not the same, therefore, interference

chances decrease. In the reverse loop, in-plane magnetic field will drag electrons to the opposite direction. Temperature has the similar effect on weak localization as the interference length is the function of temperature. From Fig. 3.14 right down branch, it is interesting to note that the trend of net NMR, which is gotten from zero field resistance subtracting the resistance at $B_z = 0.1kG$, are almost the same for both in-plane magnetic field and the temperature.

3.3   Temperature Dependence of Ultra-high Mobility GaAs/AlGaAs

In quantum transport in ultra-high mobility sample A, temperature dependence also reveals very interesting physics in 2DEG as shown in Fig. 3.15.

Temperature dependence experiment was done in a He-3 cryogenic. A heater, which equips on the bottom of the probe, along with a temperature controller with a feedback loop are used to control the system to reach a balanced temperature in a temperature range 2 K to 30 K. Below 2K, heat from absorption pump inside the insert of the He-3 cryogenic remotely changes the temperature in the sample space. A stable temperature is always reached when He-3 cooling power balanced outside heat.

The Fig.3.15 shows the magnetoresistivity at T = 0.3K to T =10K. SdH oscillations disappear when temperature reaches 1 K and phonon scattering starts to involve in from T=1.5K. This kind of oscillations could be from integration with Leaky interface phonons(LIP) [39]. The electrons at high LLs interact with LIP which carries
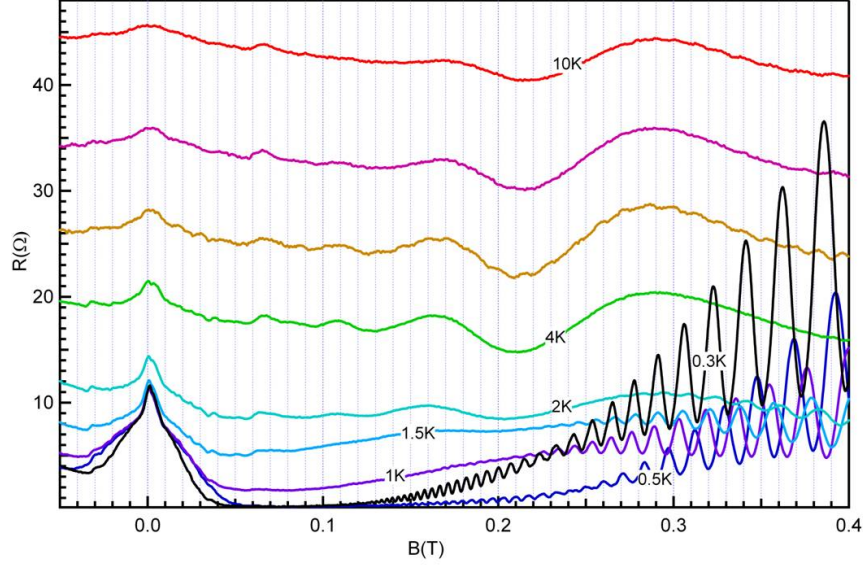
Figure 3.15 : Temperature dependence of magnetoresistivity

a wave vector $q = 2k_F$. The condition for electrons interaction with phonons is $2k_Fu_R = l\omega_C$, $l = 1, 2, 3, ...$ k_F is the Fermi wave vector of the 2DEG at zero B field as displayed in Fig. 3.16. The orders of resonance peaks are inverse proportional to the magnetic fields of peaks. The frequency of resonance is $f(B) = \frac{2k_Fum^*}{e}$ =0.3 T and $u = 2.9km$.

3.4   Conclusion

Overall, we observed a strong cyclotron harmonic spike ($2\omega_C$ spike) supposed on the top of 2nd harmonic MIRO peak in an ultra-high mobility GaAs/AlGaAs sample. It has been observed in different samples and a wide range of MW frequencies from 50GHz to 150GHz. Temperature dependence and power dependence have been systematically studied. There is no phase shift for $2\omega_C$ spike with an in-plane magnetic
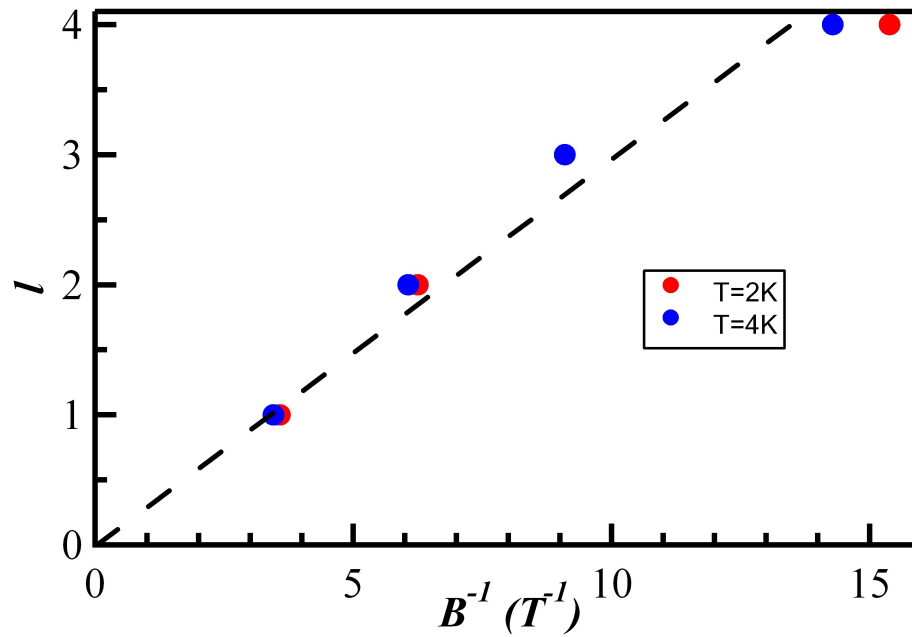
Figure 3.16 : The leaky interface phonon resonance peaks order versus inverse magnetic field. Red dots show T= 2K measurement and blue dots show T=4K measurement. Dash line shows the linear fitting of experiment data.

field. In addition to this unique spike, temperature dependence of this ultra-high mobility sample shows LIP resonance with $u = 2.9km$.

Chapter 4

Quantum Transport in Antidot Lattice Patterned High Mobility Samples under Microwave Irradiation

Quantum transport in 2DEG patterned with antidot lattices received lots of attentions recently and in such systems, GR can be observed in a low magnetic field. The electron trajectory in these modulated systems has been an open question and sparked extensive discussions. Some works [21, 40, 41, 42, 43, 44] discussed the origins of the GR peaks, which was discovered to originate either from the commensurable cyclotron diameter and lattice constant or a specific aspect ratio between the lattice constant and the dot diameter. Yuan [4] later did some followup works with high mobility samples. In high magnetic fields, AB effect has been found in an antidot lattice patterned Hall bar, which originates from the spin resolved edge states[6].

In our experiment, we used ultra-high mobility 2DEG to fabricate bare Hall bar mesas as well as the Hall bar mesas patterned with antidot lattices. The different magnetoresistance in low fields for a Hall bar mesa patterned with antidot lattices of different aspect ratios will be presented. Under MW irradiation, AB oscillations have been observed.

4.1   Experiment

In quantum transport experiments, low temperature and well prepared samples are the two key elements. The setup for low temperature environment in our experiments, as shown in Figure 3.1, is similar to that for the previous cyclotron harmonic spike experiment. On the other hand, detailed description of sample preparation, containing the procedures of e-beam lithography and fabricating micro and submicrometer antidots, will be presented in Appendix A. Preparation of our samples can be divided into three stages: 1) ohmic contact preparation with the lift-off method 2) Hall bar preparation in standard photolithography 3) antidots fabrication in e-beam lithography.

4.2   Results

4.2.1   Geometric Resonance and Magnetoresistance of Hall bar mesas

The samples are from three wafers, which are the same as those for sample A, B, and C in the previous chapter3, with key parameters listed in Table 5.1. Six small pieces are cleaved for antidots fabrication. Sample Aa is from wafer A, sample Ba and Ca are from wafer B, while sample Da, Ea, and Fa are from wafer C. Triangular antidot lattice patterns are fabricated on sample Aa to Ea and the honey comb pattern is written on sample Fa.

Those samples are cleaved into 4mm*4mm squares, with the design illustrated in Fig. 4.1A. The Hall bar is either 90 or 180 μm wide depending on samples. Fig. 4.1B
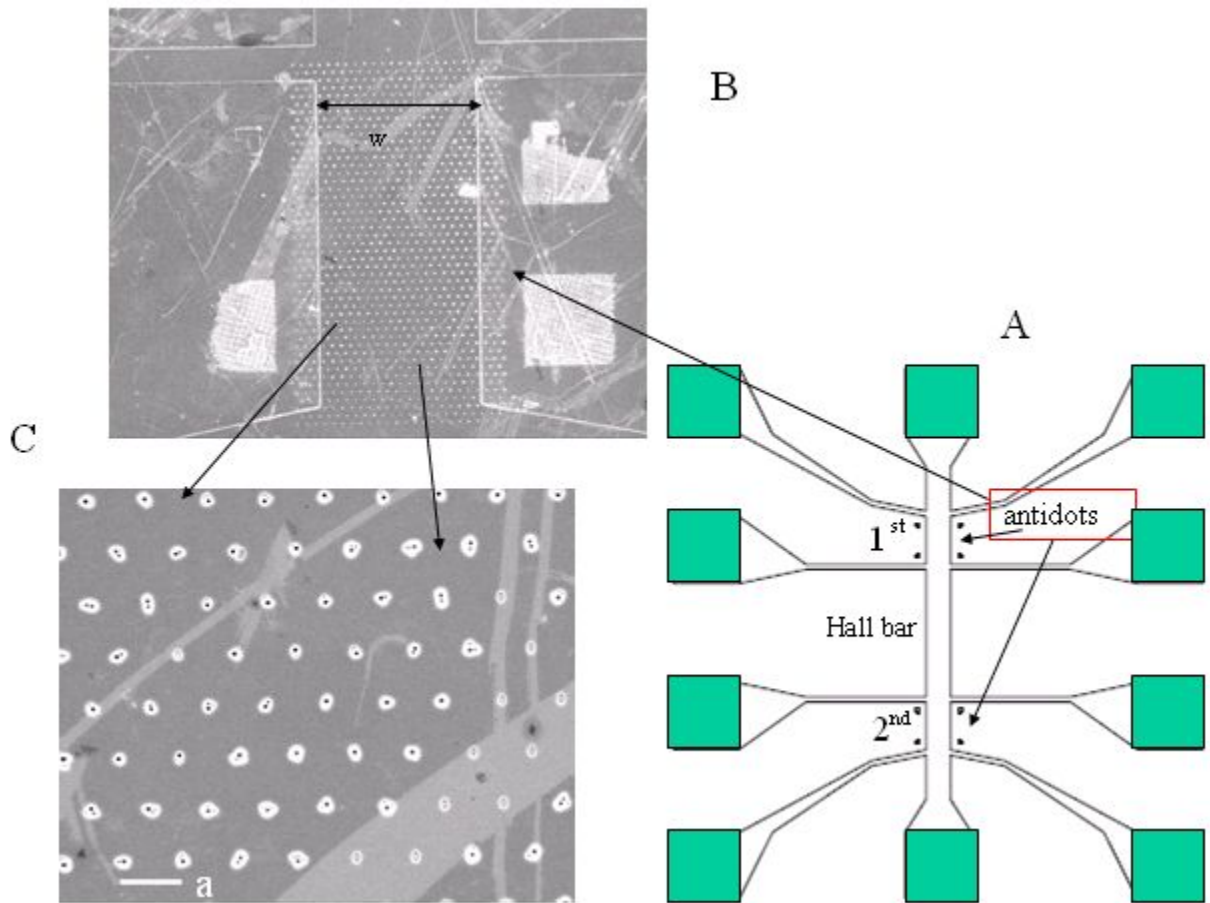
Figure 4.1 : The antidots sample image. A: Sample design. Green squares represents ohmic contacts. Hall bar section is in the middle with two antidot sections on two sides. The black spots were used to locate the Hall bar structure during fabrication of antidots. B: SEM image of the a antidot section (width w) C: Antidot SEM image.

shows a clear image of antidot lattices composed of triangular structures on top of a

Hall bar mesa. Fig. 4.1C is the enlarged pattern area. The lattice constant a and the

diameter of antidot d are intentionally designed to vary in different samples. Antidots

are artificial hard scatterers imposed on 2DEG to alter the carrier mobility μ and in

some sections, even alter the electron density n_e. Specific parameters for each sample

are listed in Table 4.1.

Sample	Aa	Ba	Ca	Da	Ea	Fa
Hall bar n_e/μ	6.13/8.6	4.24/12	4.16/12.6	3.34/27.8	2.86/29	3.1/28
1^{st}section d (μm)/ a (μm)	2/10	1.3-1.5/10	2/10	1/3	0.4/3	0.6-0.8/5
1st section n_e/μ	6.24/1.26	4.24/4.5	4.16/1.89	3.34/0.7	2.86/1.3	3.1/2.97
2nd section d (μm)/ a (μm)	2/10	1.7/10	2.5/10	1.2/6	0.6/6	0.6-0.8/5
2nd section n_e /μ	6.13/1.26	4.24/1.45	4.16/1.37	3.34/1.5	2.86/3	3.1/2.97

Table 4.1 : Antidots sample parameters. The density of electrons n_e is with unit $10^{11}cm^{-2}$ and mobility μ is with unit $10^6 cm^2/Vs$.

4.2.1.1   The Magnetoresistance and Geometric Resonance

Introducing antidot lattices creates artificial hard scatterers in 2DEG and shortens the mean free path of the carriers, leading to a decreased mobility. This can be seen from low magnetic field (B< 1T) magnetoresistance in the inset of Fig. 4.2. In very small fields, the antidot lattice patterned section (red line) possesses a resistance about three times of the unpatterned one (blue line) and displays strong GR oscillations. But when the field is higher than approximately 0.2 T, two resistances almost overlap, indicating a negligible effect of dilute antidot scatterers (a = 10 μm, d $\sim$1.5 μm ,$\Rightarrow$2.25% scatterers density) on the electron mean free path and thus magnetoresistance in a relatively strong magnetic field.

The mobility of 2DEG drops after the antidot lattice is added, and the more it drops, the more it affects the magnetoresistance in high fields. But in low fields, the
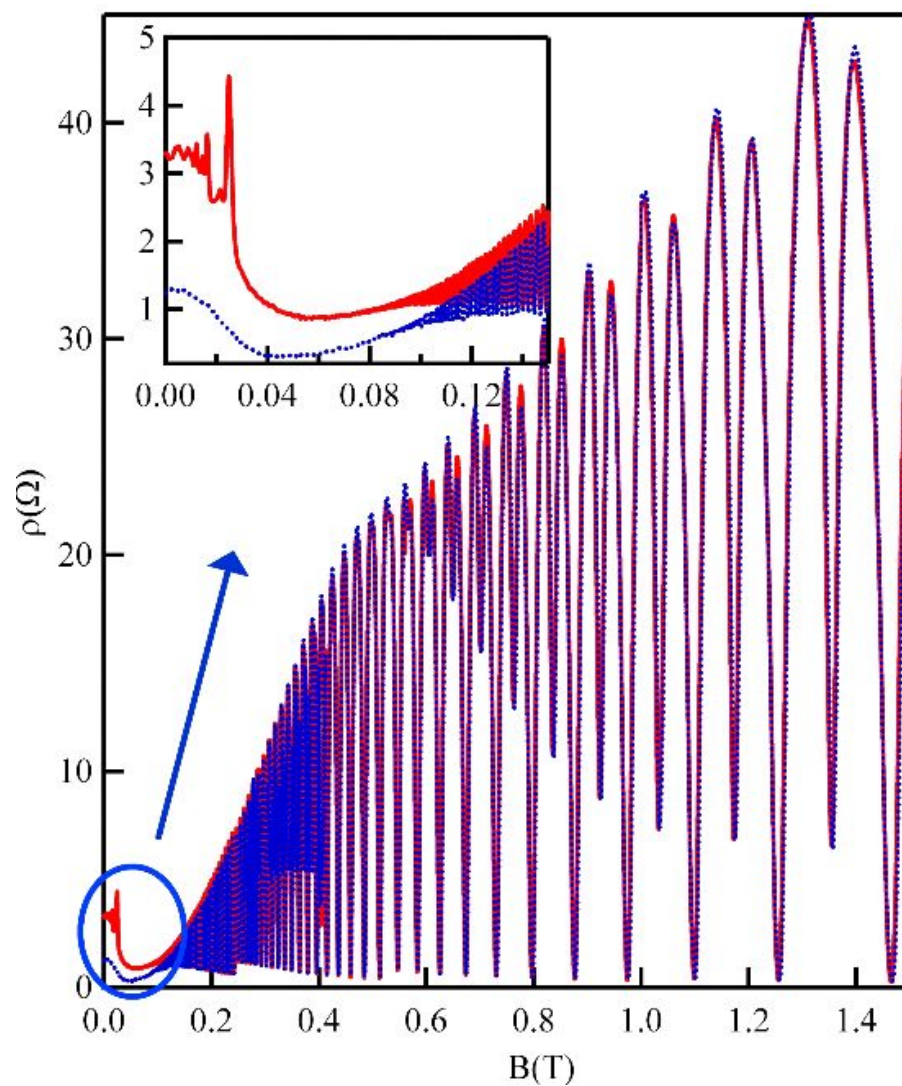
Figure 4.2 : Magnetoresistance of sample B. The blue line is for the Hall bar section and the red line is for the antidots section. The inset is the enlarged low fields magnetoresistance in the blue circle.

quality of GR peaks are related to its original mobility, which is determined by the purity of the sample. A sample with higher original mobility usually produces higher orders of GR peaks with sharper features. In Fig. 4.3, the first one is the GR from sample Aa (original wafer mobility $8.6 \times 10^6 cm^2/Vs$) with only two peaks. Second and third are GR from sample Ba (original wafer mobility $12 \times 10^6 cm^2/Vs$) and Da (original wafer mobility $27.8 \times 10^6 cm^2/Vs$) with multiple peaks. The major two peaks in sample Da are sharper and stronger than in sample Ba.

4.2.1.2 Geometric Resonance in Triangular Antidot Lattices with Different Aspect Ratios

GR oscillations have been studied for different kinds of lattice patterns, such as triangular and square ones with various aspect ratios. The pattern of GR oscillations has strong odd-even peaks and the cyclotron radius of peaks is commensurable with the lattice constant.

The cyclotron radius is

$$R_C = l_B^2 k_F = \left(\frac{257 \mathring{A}}{\sqrt{B}} \right)^2 \sqrt{2\pi n_e}$$

, where there l_B is magnetic length, k_F is the Fermi wavevector, and n_e is electron density.

For sample Aa in Fig. 4.3a), $R_C = 5.49\mu m$ for the first order and $9.5\mu m$ for the second order. The ratio of cyclotron diameter to the lattice constant is $\frac{2R}{a} = 1.1, 1.9$
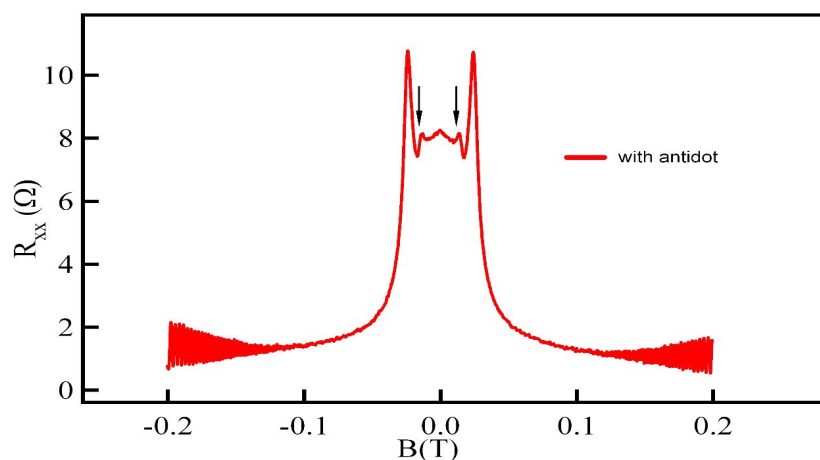
(a) Geometric resonance in sample Aa from wafer A. Both sections exhibit the same GR. Black arrows point to the 2nd order peaks.
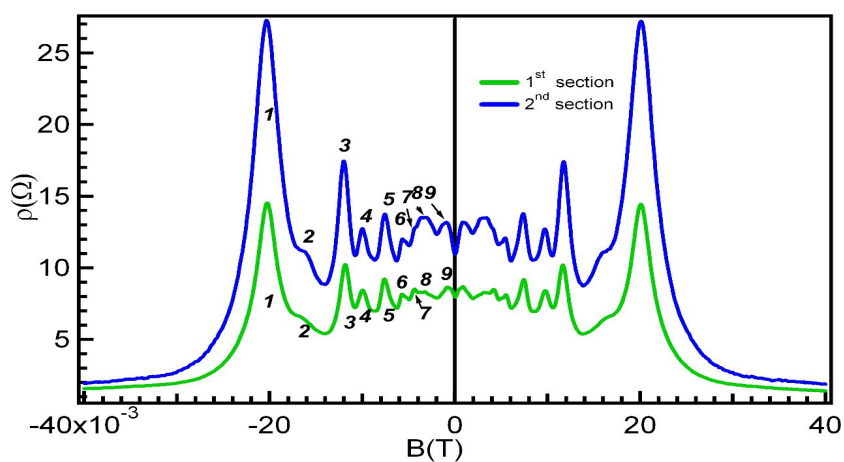
(b) Geometric resonance in sample Ba from wafer B
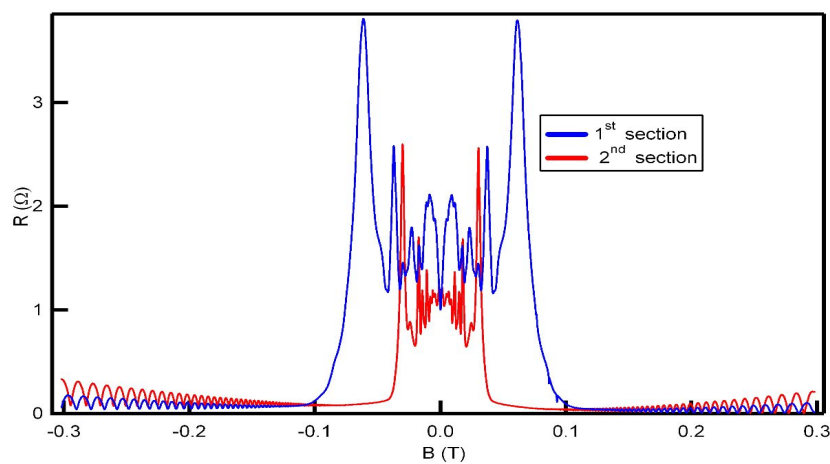
(c) Geometric resonance in sample Da from wafer C

Figure 4.3 : Geometric resonance in samples Aa, Ba, Da with various mobilities
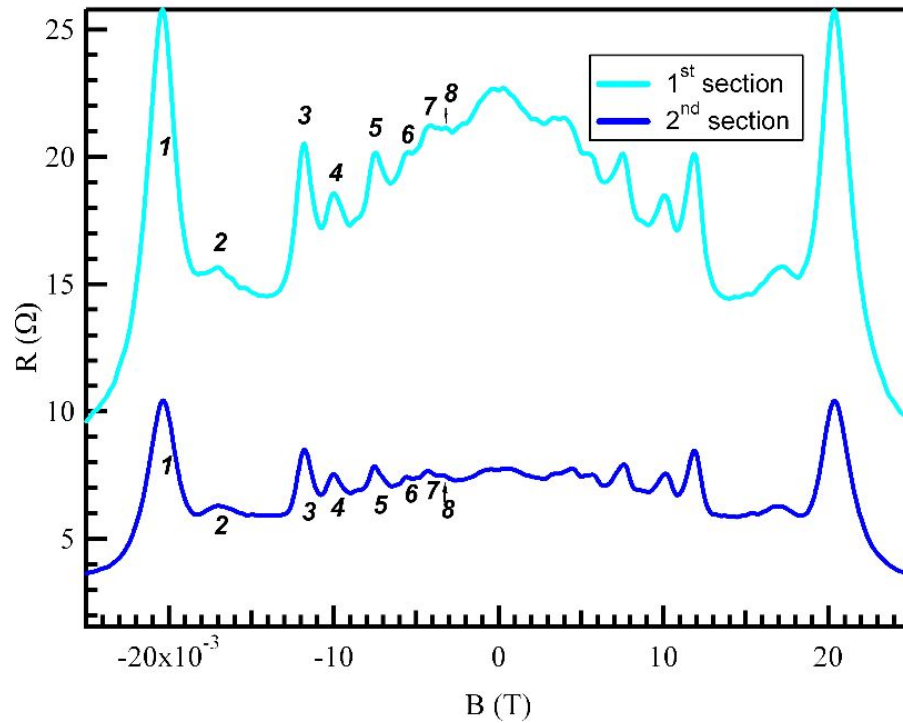
Figure 4.4 : Geometric resonance for sample Ba

for the first and second order respectively.

In sample Ba, the ratios $\frac{2R}{a}$ for the 1st section , which are on the light blue line in Fig. 4.4, are 1.056,1.256, 1.818, 2.132, 2.872, 3. 982, 5. 374, 6. 592 for the 1st to 8th order peaks respectively. The ratios $\frac{2R}{a}$ for the 2nd section (on the dark blue line) are 1.056, 1. 262, 1.818, 2.13, 2.78, 3. 818, 4. 964, 6.148 for the 1st to 8th order peaks respectively.

In sample Ca, we have similar results as in Fig. 4.5. The ratios $\frac{2R}{a}$ for the 1st section (blue line) are 1.056,1.278, 1.8, 2.16, 2.84, 3.8, 4.98, 26 for 1st to 9th order peaks respectively. The ratios $\frac{2R}{a}$ for the 2nd section (green line) are 1.054, 1.284, 1.8, 2.16, 2.86, 3. 844, 5.06, 6.08, 24 for the 1st to 9th order peaks respectively.
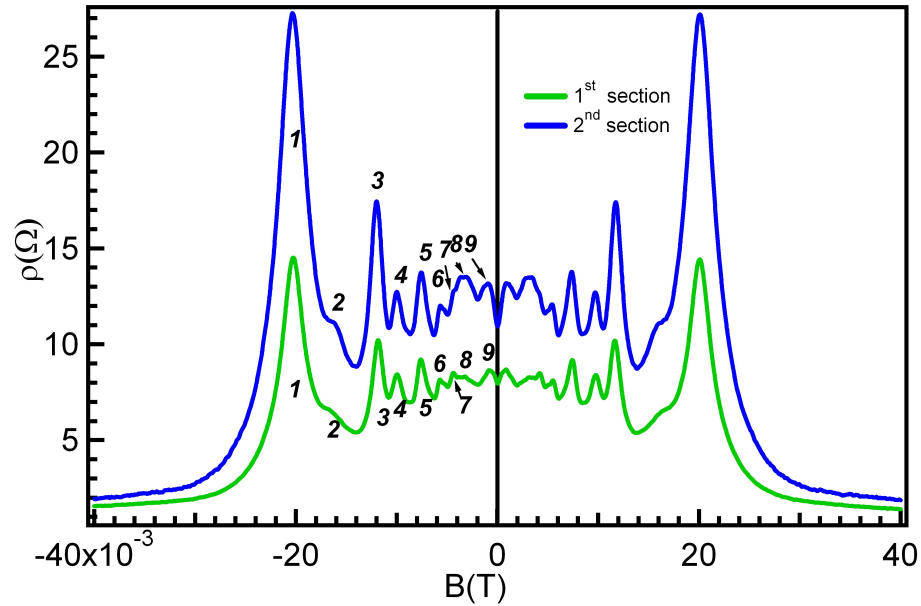
Figure 4.5 : Geometric resonance for sample Ca

Sample Da 's results are in Fig. 4.6. The ratios $\frac{2R}{a}$ for the 1st section (a) are 1.05,1.33, 1.72, 2.13, 2.38, 3.73, 5.69,7.25,8.93, 13.71 for the 1st to 11th order peaks respectively. The ratios $\frac{2R}{a}$ for the 2nd section (b) are 1.06, 1.31, 1.82, 2.18, 2.47, 2.88, 3.82, 4.19, 5.02, 5.89,6.9, 27 for the 1st to 12th order peaks respectively.

In sample Ea, Fig. 4.7, the ratios $\frac{2R}{a}$ for 1st section (a), are 1.05, 1.28, 1.76, 2.15, 2.43, 2.81, 3.76, 4.11, 4.87, 5.7, 6.74, 9.15, 28.78 for the 1st to 13th order peaks respectively. The ratios $\frac{2R}{a}$ for 2nd section (b) are 1.07, 1. 29, 1.84, 2.19, 2.89, 3. 88, 5.08, 6.48, 65.67 for the 1st to 9th order peaks respectively.

As the mobility increases, more detailed features show up around zero magnetic field. Even-odd peaks come in strong-weak patterns, implying spin related phenomena.
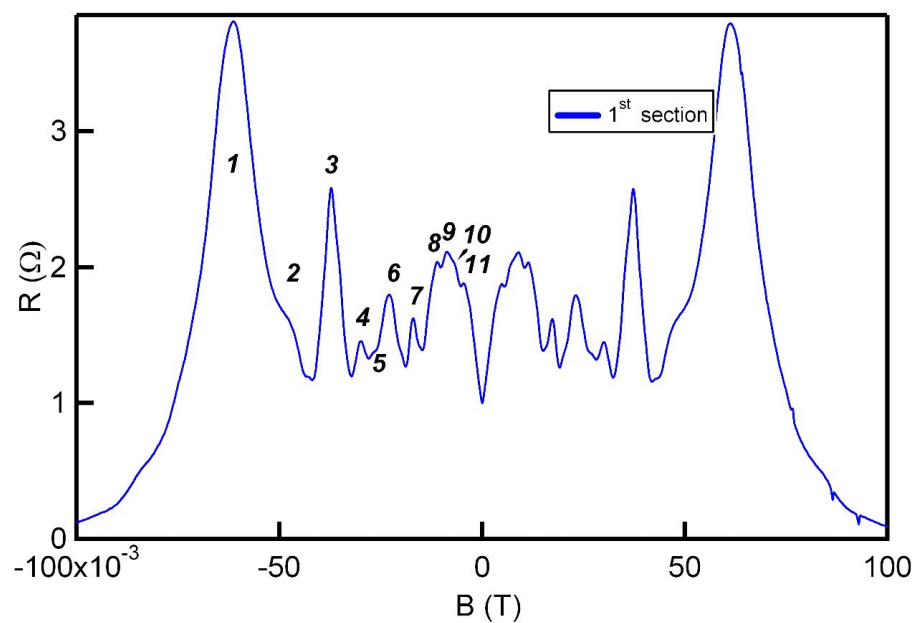
(a) 1st section
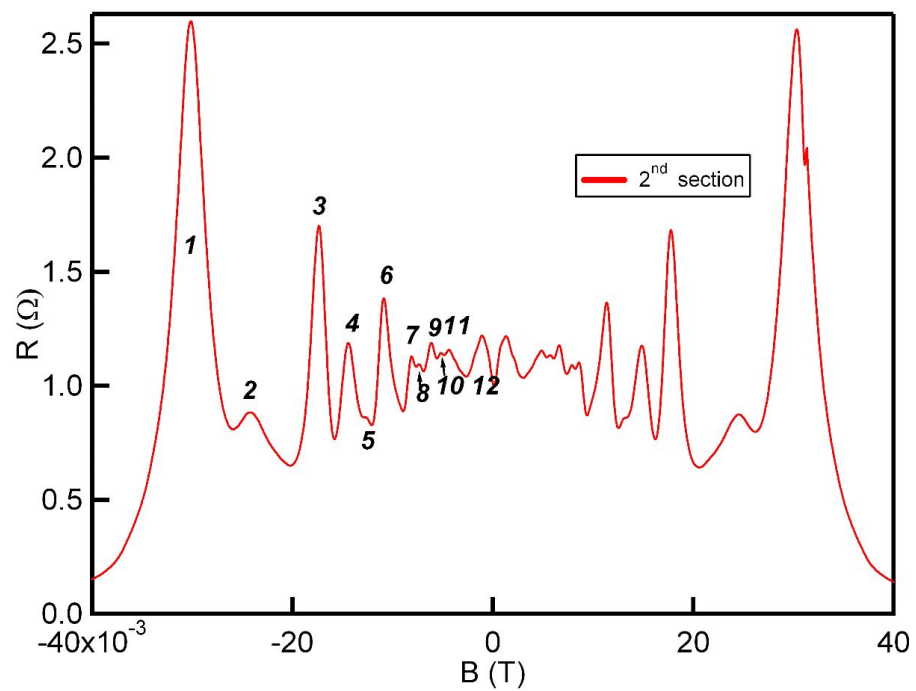
(b) 2nd section

Figure 4.6 : Geometric resonance for sample Da
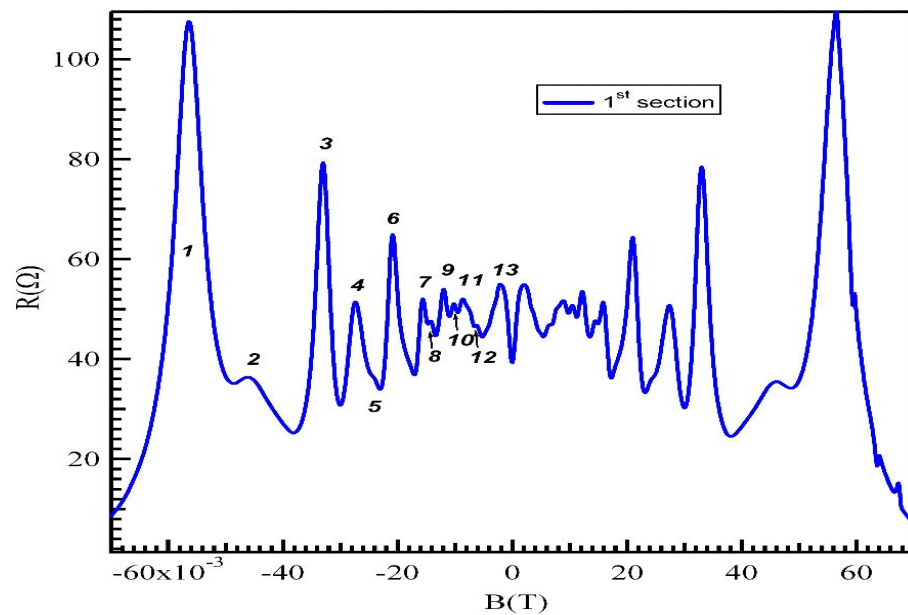
(a) 1st section
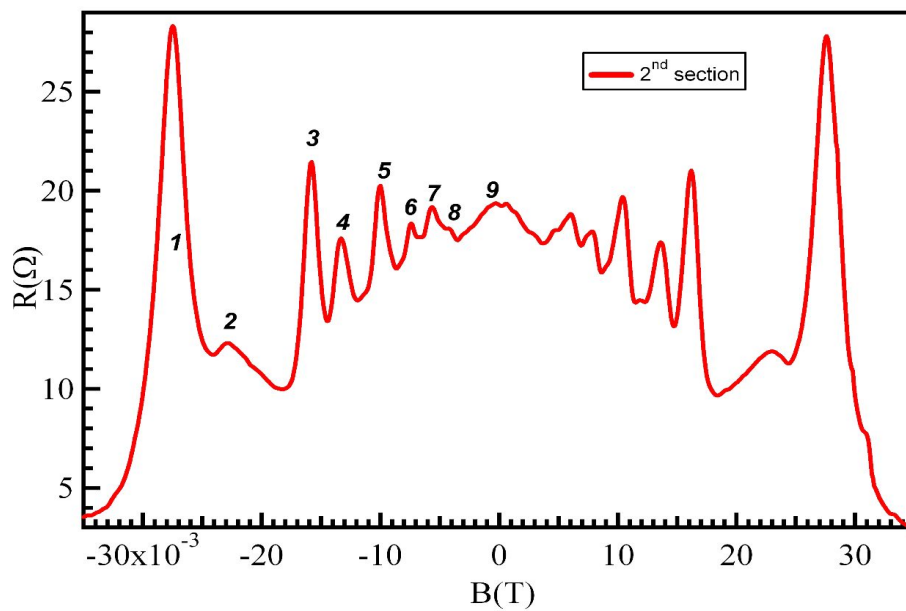
(b) 2nd section

Figure 4.7 : Geometric resonance for sample Ea

4.2.1.3   Temperature Dependence of Geometric Resonance

Temperature-dependent experiments can be realized with a heater aside the sample with feed back control loops as introduced in chapter3. The range of temperature in use is from 0.3K to 35K.

Antidot lattices provide the electric potential modulation for 2DEG. The antidot is the electric barrier for freely moving electrons. Increasing temperature enhances the fluctuation of Fermi energy and consequently electrons have more chances to tunnel through the barrier. In Figs. 4.8,4.9,4.10,4.11, and 4.12, first order peaks are always the most robust with respect to the increasing temperatures. While lower order peaks are very easy to be destroyed, in ultra-high mobility samples, such as Da and Ea, the 3rd and 5th order peaks are also quite robust at high temperature. It should be noted that odd peaks are major peaks that can survive at high temperature, while even peaks are affiliated to major peaks and disappear when temperature increases.

4.2.1.4   Geometric Resonance and Hall Voltage Oscillations

In Fig. 4.13, GR with respect to different in-plane magnetic fields has been investigated. There is no phase shift when in-plane magnetic fields are applied and the amplitude of peaks only displays very small variation. In Fig. 4.14 and 4.15, Hall voltage oscillations between red and black lines are presented for in-plane magnetic fields between 0 and 2.0T. This kind of oscillations are antisymmetric and their amplitudes increase with in-plane magnetic fields. The amplitude of the first order peak
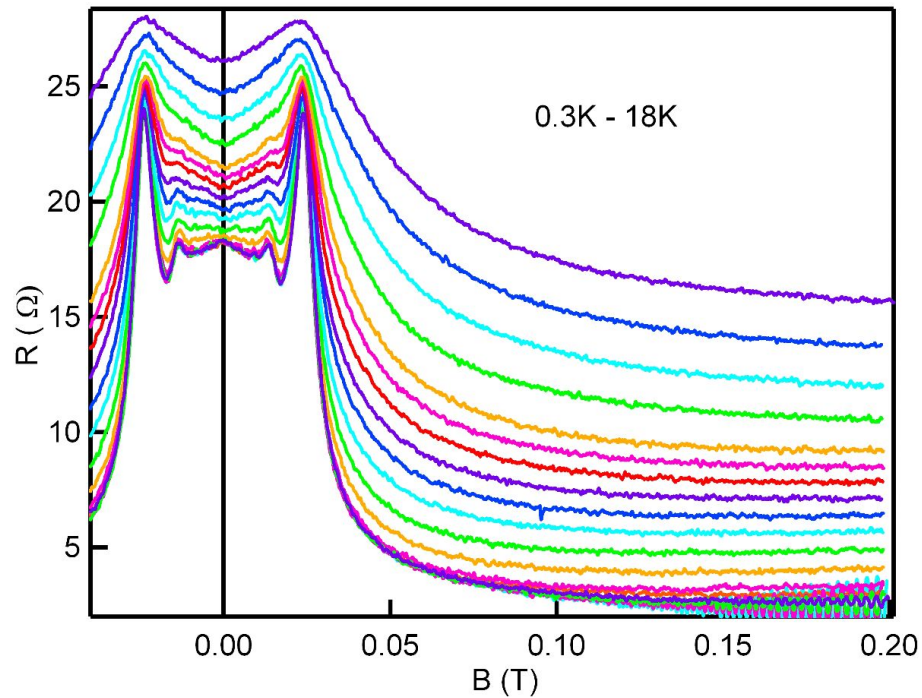
Figure 4.8 : Temperature dependence of magnetoresistance of sample Aa for temperature 0.3K to 18K

increases about 5 times when a 2.0T in-plane magnetic field is applied. This kind of Hall oscillation is the indication of magnetic lattices [45, 46].

4.2.1.5 Geometric Resonance in a Honeycomb Antidots Lattice

To further study the electron transport, honeycomb pattern has been fabricated with a lattice constant $5\mu m$ and a dot diameter $0.5\mu m$. The GR trace is shown in Fig. 4.16. The ratios of $\frac{2R_C}{a}$ are 1.044, 1.786, 2.136, 2.748, 3.068, 3.684, 4.116, 4.844, 6.464, 4.912 for peaks with the 1st to 11th order. Certain patterns show up, but the underlying mechanism for the formation of either triangular or honeycomb lattices are not very clear.

(a) 1st section

(b) 2nd section
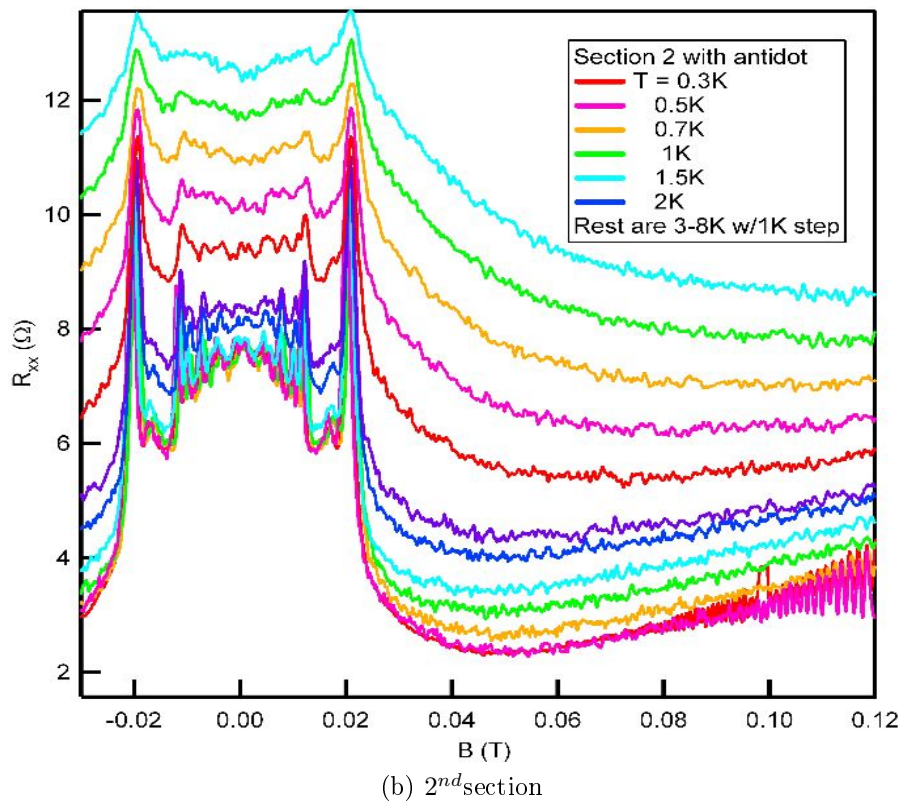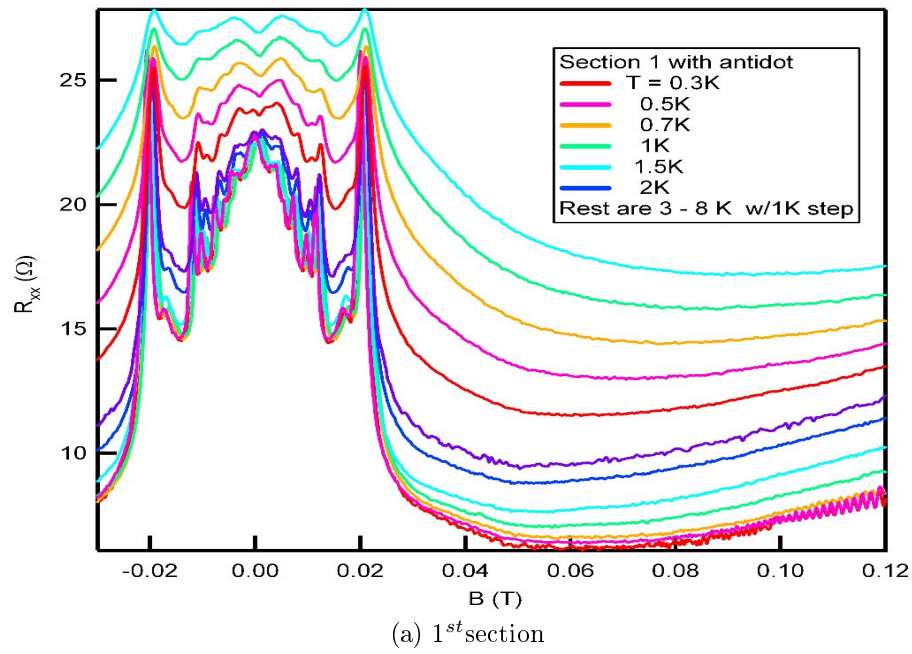
Figure 4.9 : Temperature dependence of magnetoresistance of sample Ba for temperature 0.3K to 8K.
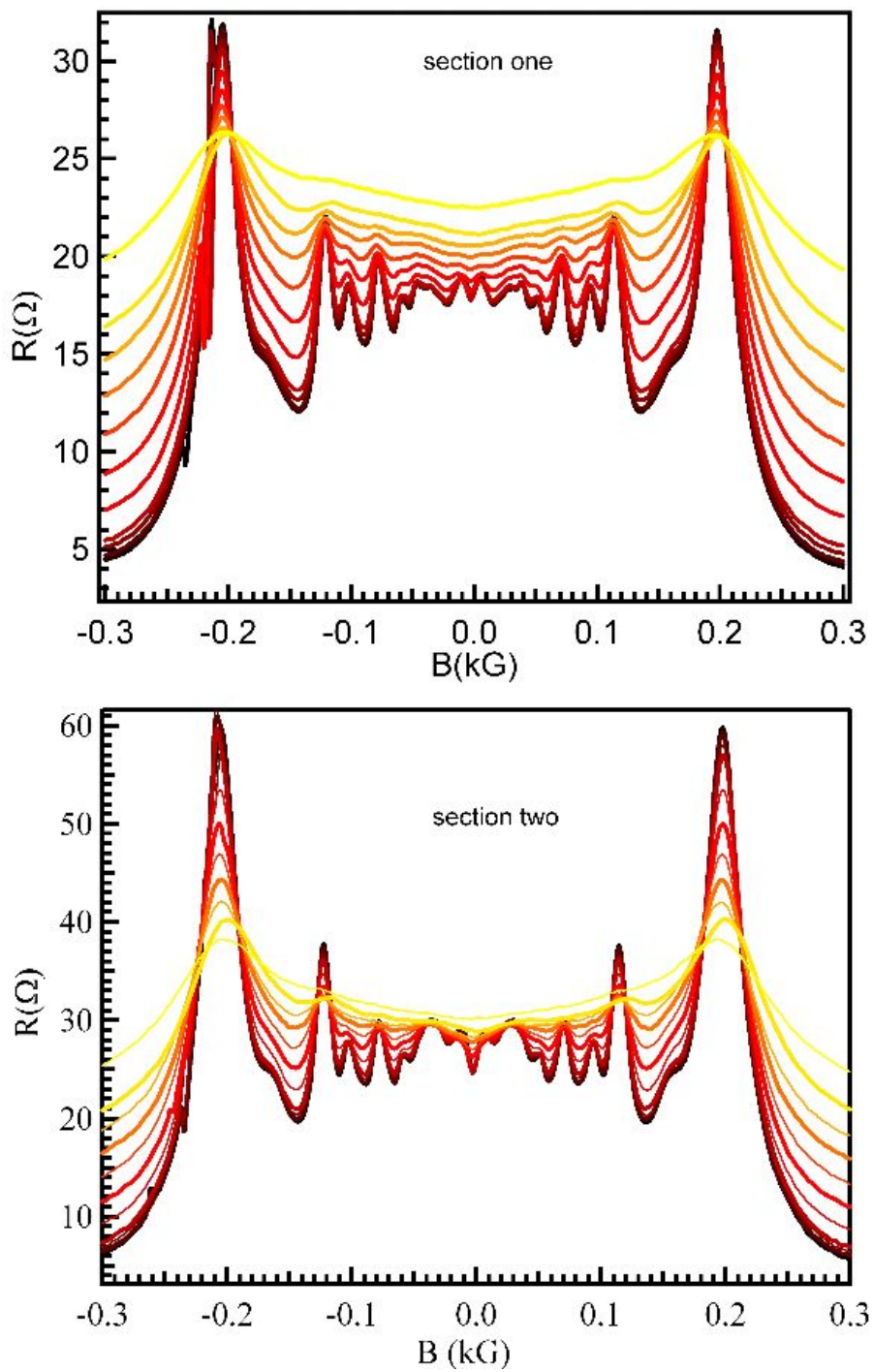
Figure 4.10 : Temperature dependence of magnetoresistance of sample Ca for temperature 0.3K to 10K
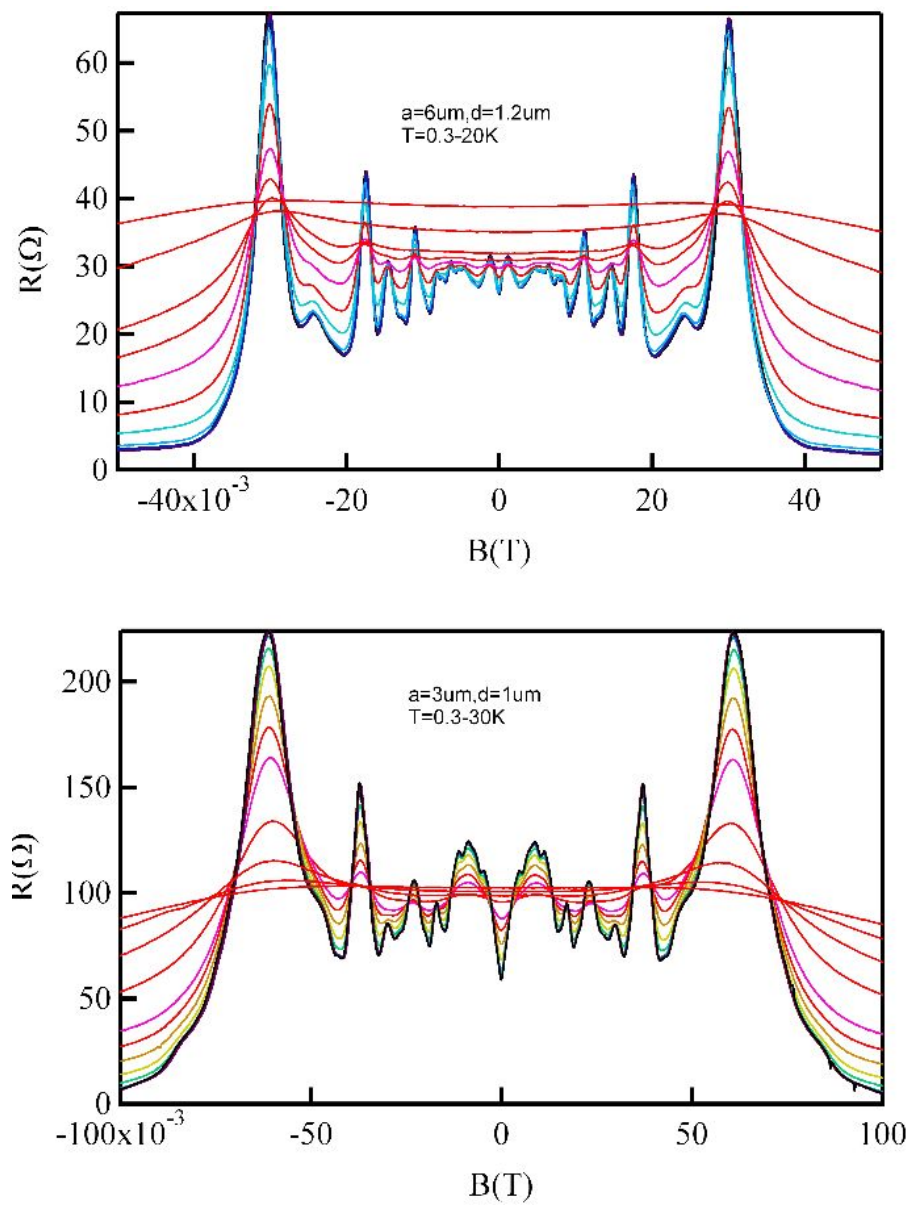
Figure 4.11 : Temperature dependence of magnetoresistance of sample Da for temperature 0.3K to 20K or 30K for section one or two respectively.
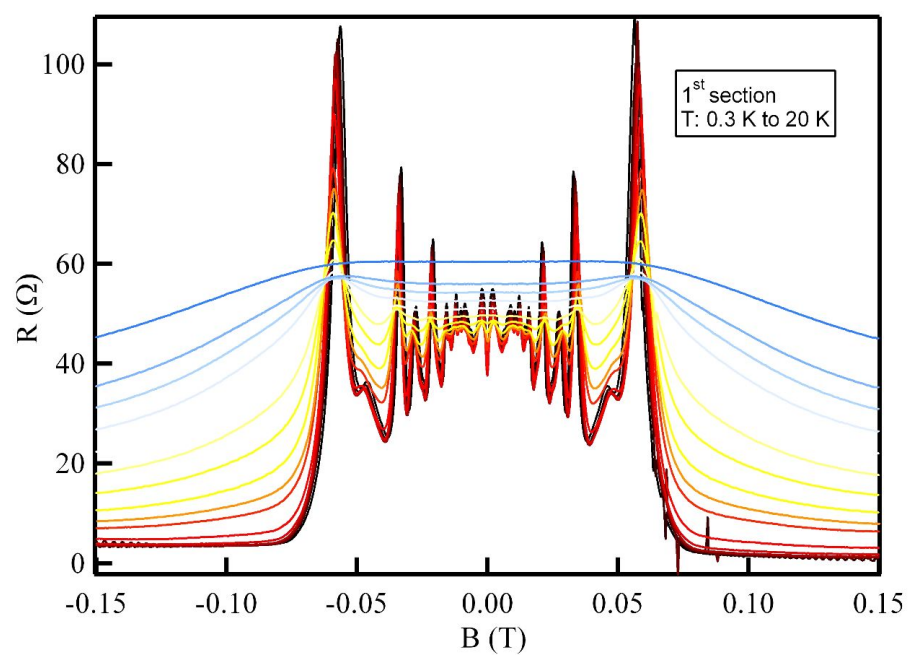
(a) 1st section
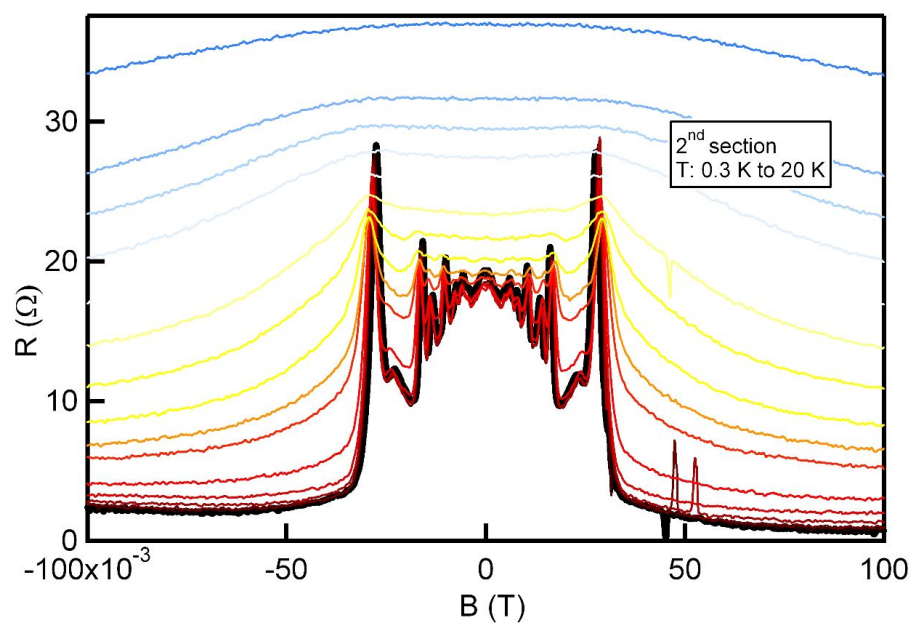
(b) 2nd section

Figure 4.12 : Temperature dependence of magnetoresistance of sample Ea for temperature 0.3K to 20K
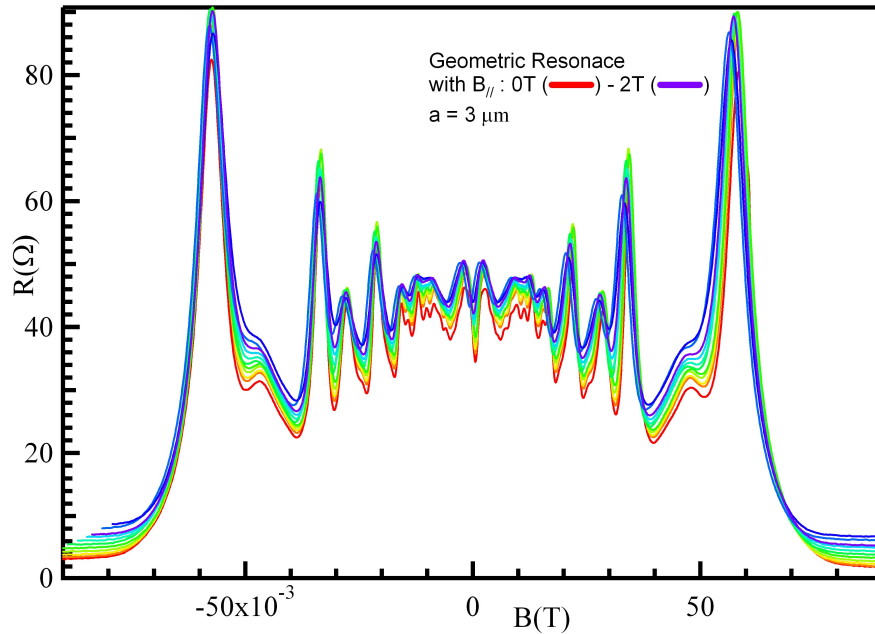
Figure 4.13 : Geometric Resonance in inplane magnetic fields from 0 T to 2T with the magnetic field increment step 0.2T. The data were taken from sample Ea with lattice constant $3\mu m$.

From the ratio $\frac{2R_C}{a}$ in samples Aa to Fa, we note the similarity of the results: they are around integer numbers at some orders of peaks and the period of the peaks are proportional to 1/B. To further illustrate the similarity of GR oscillations for the antidot lattices in different wafers with various aspect ratios, we normalize magnetic fields in all four traces in Fig. 4.17a) by factorizing out the field strength at the first order peaks. Surprisingly, all major peaks align very well in normalized magnetic fields. There are two sets of peaks existing in the traces and each of them has the period of normalized traces $\triangle \frac{1}{B'}$. This $\triangle \frac{1}{B'}$ happens to be around one. The first set is noted in dash arrows in Fig. 4.17a) up and red dots in Fig. 4.17a) down with $\frac{1}{B'} = 1, 2.037$. The second set is noted in solid arrows in Fig. 4.17a) up and blue
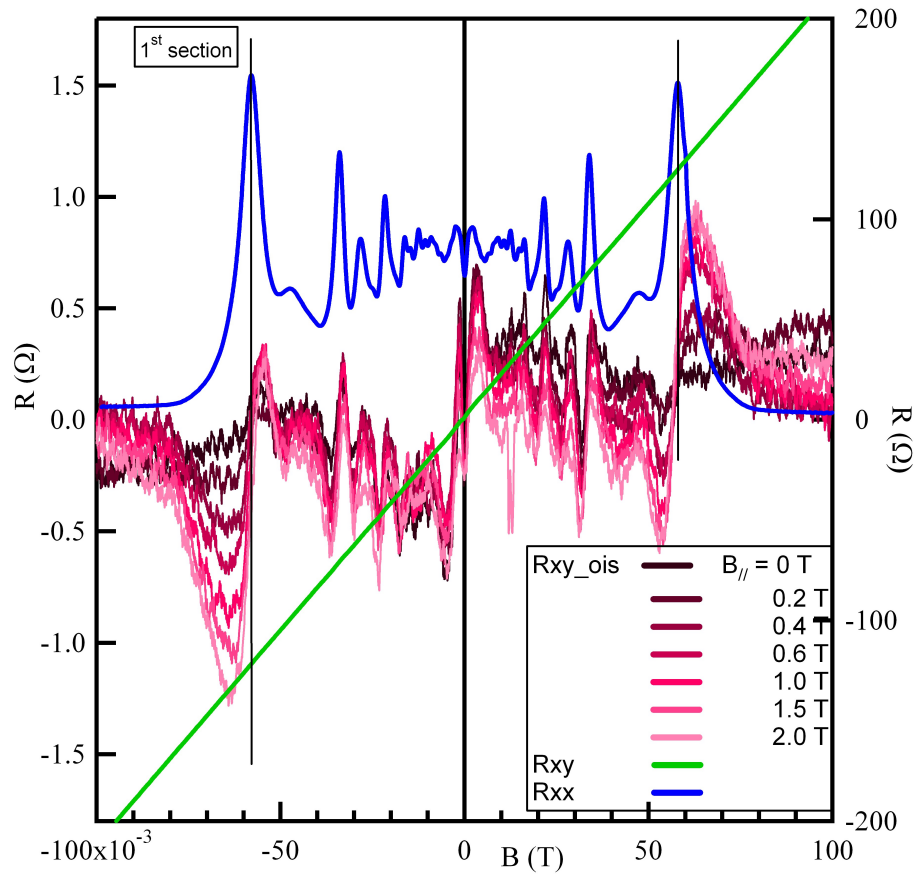
Figure 4.14 : Hall oscillations in antidot lattices with different in-plane magnetic fields (in Red and Black lines). Geometric resonance traces with arbitrary amplitude are shown in blue line. Hall voltage was shown in green line. This figure is for sample Ea section one.
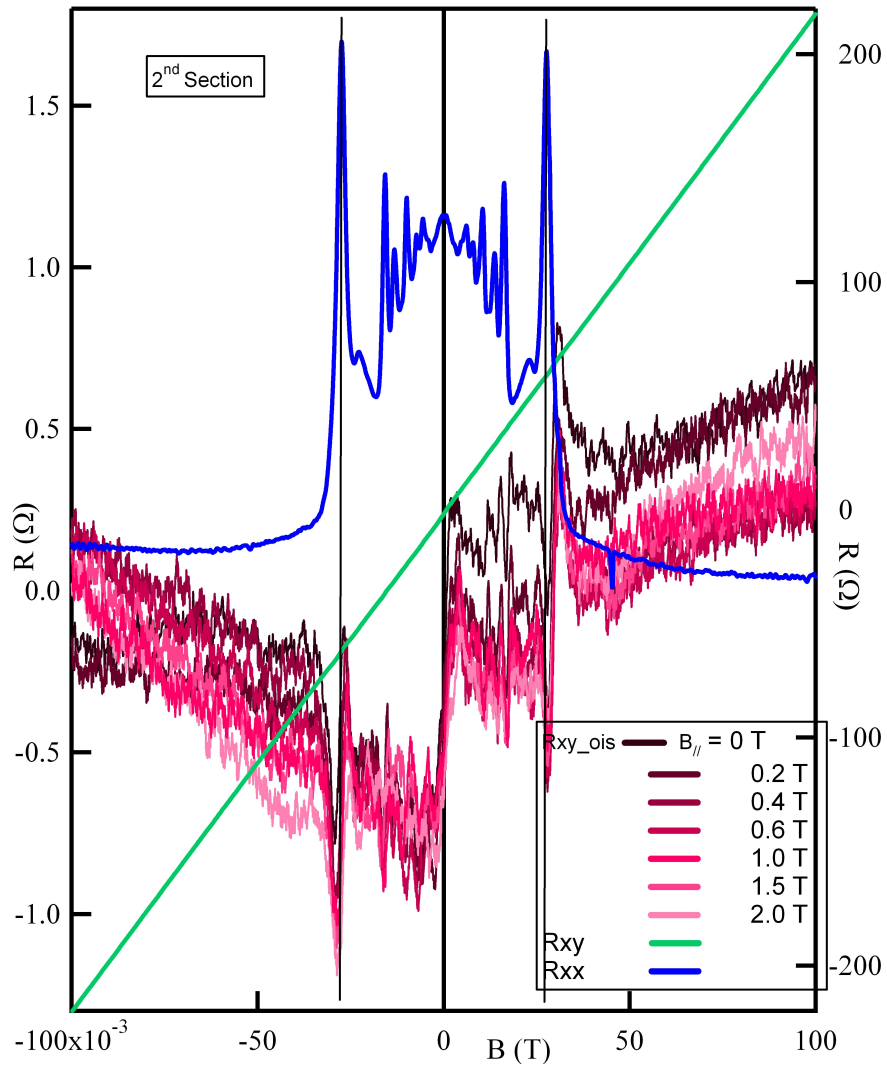
Figure 4.15 : Hall oscillations in antidot lattices with different in-plane magnetic fields (in Red and Black lines). Geometric resonance traces with arbitrary amplitude are shown in blue line. Hall voltage was shown in green line. This figure is for sample Ea section two.
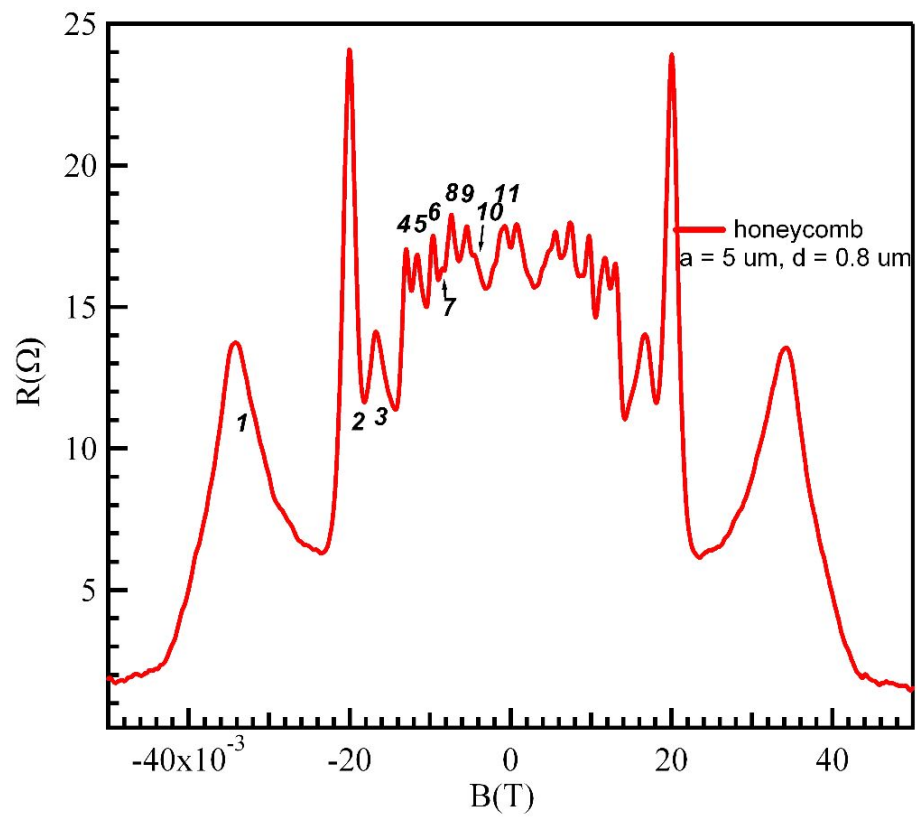
Figure 4.16 : Geometric resonate for the honeycomb lattice patterned 2DEG in sample Fa.

dots in Fig. 4.17a) down with $\frac{1}{B'} = 1.664, 2.654, 3.53$. So, the period for each set is $\frac{1}{B_1}$, where B_1 contains the information of density of electrons as well as the lattice constant. From Eq. 4.2.1.2, and the fact that $\frac{2R_C}{a}$ is around an integer number N in major peaks, we can obtain the period $\frac{\sqrt{n_e}}{Ba} \propto N$. So $\frac{1}{B} \propto \frac{aN}{\sqrt{n_e}}$ and the period is related to a and n_e. From this conclusion, we can see that the aspect ratio does not influence the period of GR in the dilute dots regime.

In the same way, we put GR in triangular and honeycomb lattices traces together. Those two lattices are fabricated using the same wafer with similar lattice constants and diameters.The normalized inverse magnetic fields of major peaks as noted in Fig. 4.17b) are 1 and 2.065 for the dash line and 1.707, 2.714, 3.504, and 4.545 for the solid line.

4.2.2   AB Oscillations in Antidots Lattices with MW Irradiation

AB oscillations, in an interference experiment with a magnetic flux present, have been observed in a metal ring and in antidot lattices in the quantum Hall regime, as mentioned in chapter 2.

In sample Ca, under the MW irradiation, B period oscillations show up in the place of MIRO peaks in magnetoresistance of antidot lattice patterned 2DEG (Red line in Fig. 4.18). At the $\varepsilon = 2$ MIRO peak, oscillations have one period $\triangle B_1 = 0.003T$ and another period $\triangle B_2 = 0.007T \sim 2\triangle B_1$. Because $\phi = \frac{h}{e} = \triangle B \star (\pi r^2)$, there is $2r \sim 1.3\mu m$, close to the dot SEM measured diameter, $2\mu m$. In dark trace around the
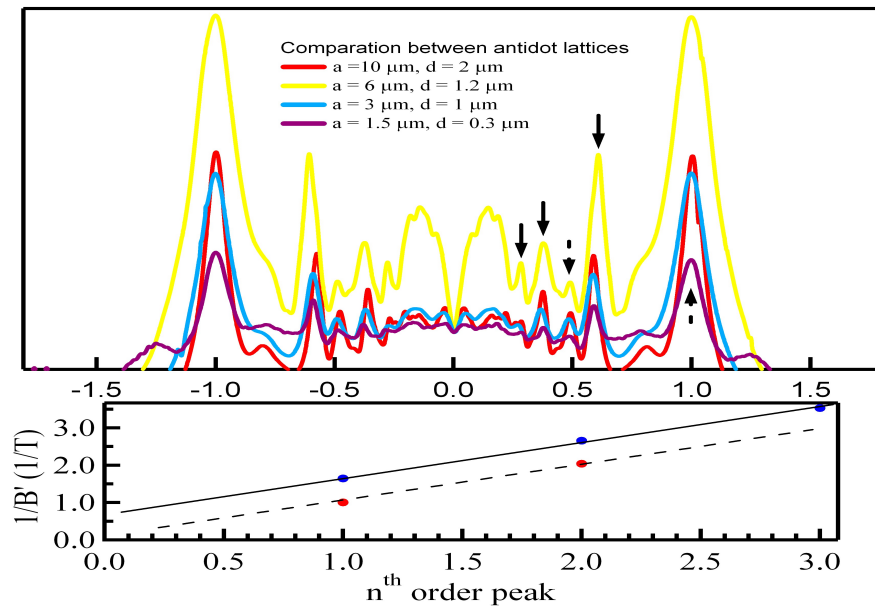
(a) up: Geometric Resonance traces for different triangular antidots lattices with various lattice constants and diameters and for different samples with different mobilities and densities. All traces were normalized by dividing first peak magnetic field. Solid arrows and dash arrows denote two sets of GR . The figure is in arbitrary y axis. down: normalized inverse magnetic field with order number for n^{th}peaks. Red dots for data are denoted in dash arrows and blue dots for data in solid arrows. The magnetoresistance trace for antidot lattice with lattice constant a $1.5\mu m$ and diameter $0.3\mu m$ is by courtesy of Z. Q. Yuan.
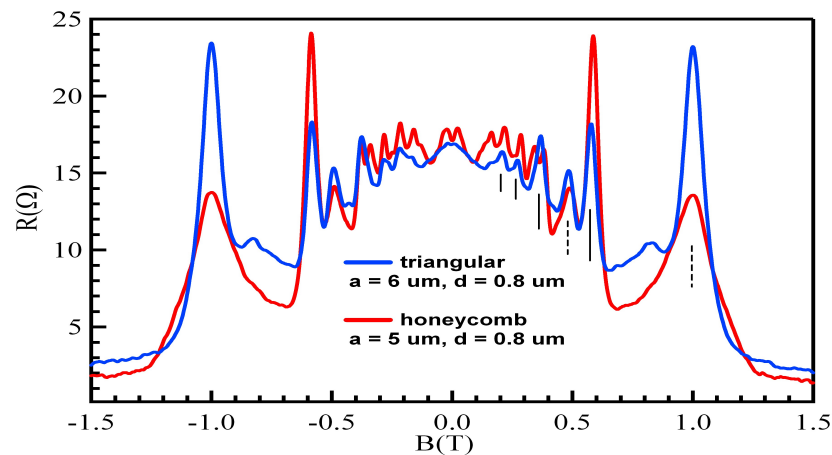
(b) Comparison of GR in triangular and in honeycomb antidot lattices in same wafers with similar lattice constants and diameters.

Figure 4.17 : Comparison GR between different antidot lattices.
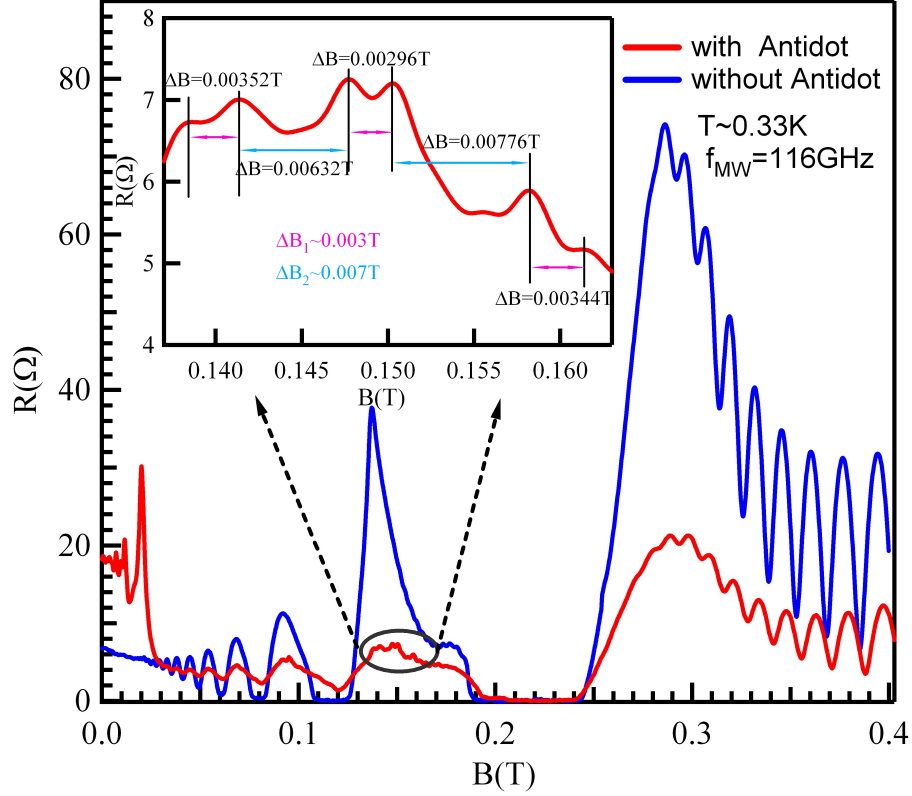
Figure 4.18 : AB oscillation in MIRO regime in sample Ca. Blue line: magnetoresistance in MW irradiation on a Hall bar mesa. Red line: magnetoresistance in MW irradiation on antidots lattices patterned 2DEG. Inset: enlarged oscillations on top of $\varepsilon = 2$ MIRO with periods $\triangle B_1 = 0.003T$ and $\triangle B_2 = 0.007T$.

same magnetic field, there are no B period oscillations. So, this phenomenon needs both the MW excitation (f_{MW} and B) and an interference loop created by antidots, which leads to the MW induced AB effect.

MW induced AB effect exists not only in $f_{MW} = 116GHz$ as shown in Fig. 4.18, but also in other frequencies from 70 GHz to 130 GHz as found in our experiment.

In an in-plane magnetic field, this kind of oscillations become weaker as the in-plane magnetic fields become stronger and eventually disappear. This may be related to the suppression of MIRO in the in-plane fields.
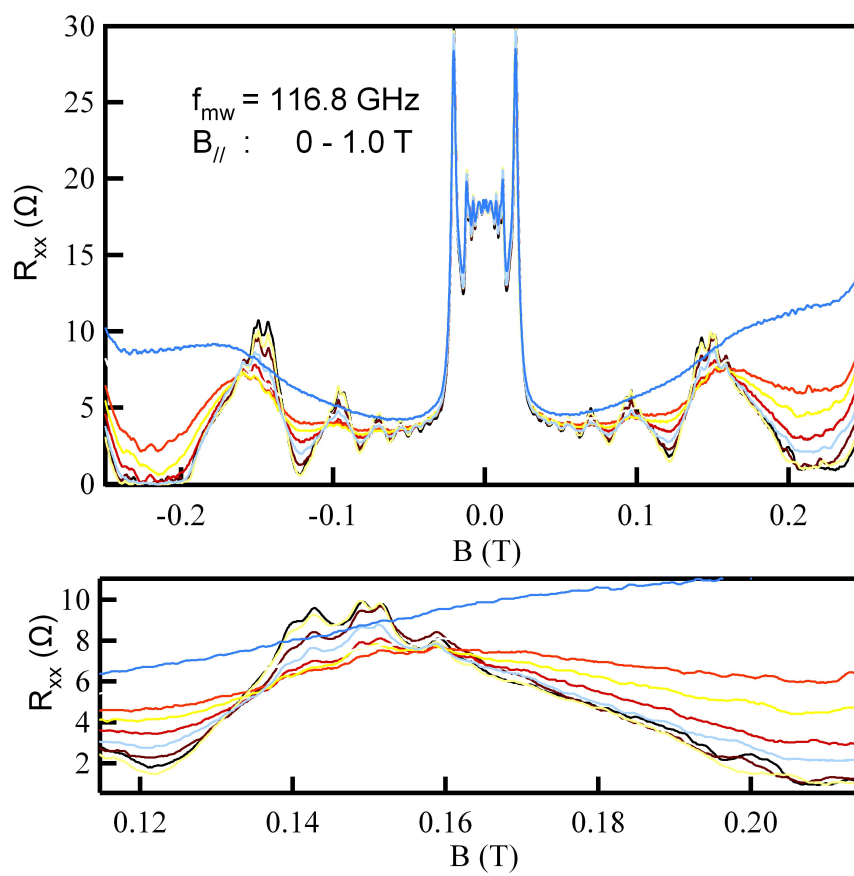
Figure 4.19 : AB type oscillations in in-plane magnetic fields from 0 to 1.0T with MW frequency 116.8GHz.

This oscillation may be related to the edge magnetoplasma modes around antidots. The interference of the edge current leads to AB oscillations.

4.3 Conclusion

Overall, antidot lattice modulated 2DEG can display many interesting phenomena, including GR, Hall oscillations, and AB effect in MW irradiation.

Chapter 5

Quantum Transport in Two Dimensional Hole Systems: Zener Tunneling Effect and Microwave Induced Resistance Oscillations

5.1 Zener Tunneling in Two Dimensional Hole Systems

5.1.1 Background:Zener Tunneling in Two Dimensional Electron Systems

Zener tunneling in 2DEG has been discovered in [29], where 1/B oscillations in differential magnetoresistance, r_{xx}, were observed when a DC-bias current I_{dc} is applied in a Hall bar sample. The magnetic fields of the oscillation peaks were found to be $B_l \propto \frac{I_{dc}}{wl}$, where $l = 1, 2, 3...$ is the orders of peaks and w is the width of the Hall bar. The effect, while rather spectacular, can be explained by a simple model [29] based on Zener tunneling of semiclassical electron orbits between N and $N+1$ LLs (N is the LL index) in a Hall field E_y, in which an energy conservation rule, i. e.,$2R_c e E_y = l\hbar\omega_c$, is essential, where $2R_c$ is the orbital diameter, a length scale characterizing the hoping distance ΔY. It was experimentally found that $\Delta Y = \gamma R_C, \gamma \approx 2$. High amplitude (comparing to magnetoresistance in the same magnetic fields) oscillations were observed up to $l = 4$ in the samples of $3 \times 10^6 cm^2/Vs$ mobility, and subsequently, to $l > 10$ in very-high mobility $\mu \approx 10^7 cm^2/Vs$ 2DEG in GaAs[29, 47, 48, 49]. The oscillations can be viewed as, in effect, a series of geometrical resonance in a homogeneous 2DEG resulting from commensuration of orbit size with a periodic modulation

of scattering rates[29, 50, 51].

5.1.2 Experiment

5.1.2.1 Sample Characterization

Major samples we used for this work are samples Ah and Bh as seen in Table
5.1, which are the Hall bars processed with photolithography and wet-etching on
pieces cleaved from a molecular beam epitaxial wafer. The wafer has a 15nm-width
$Al_{0.4}Ga_{0.6}As/GaAs/Al_{0.4}Ga_{0.6}As$ symmetrical QW (QW) and a carbon dopant layer
50 nm above the QW. Ohmic contacts to the 2DHG were made by diffusing Zn/In
alloy on the Hall bar. Both samples have a hole density of $p \approx 2 \times 10^{11}/cm^2$ and a
mobility of $\mu \approx 7 \times 10^5 cm^2/Vs$, determined from SdH measurements at T = 0.33 K.
We deduced the transport scattering time τ_{tr} from Drude relation $\tau_{tr} = \frac{\mu m^*}{e}$, where
$m^* \approx 0.4m_e$ is the hole effective mass (measured separately by MW cyclotron res-
onance (CR) [38]),m_e is the free electron mass.$\mu = \frac{1}{pe\rho}$, ρ is the magnetoresistivity.
The quantum scattering time τ_q was estimated from the onset of SdH, $\omega_C \tau_q \approx 1$,
where $\omega_C = eB/m^\star$ is the hole cyclotron frequency. For comparison, the scatter-
ing times of a typical 2DEG sample used in [29], sample Ch, are also listed. It is
worth emphasizing that the scattering times in Ah, Bh, Ch are compatible, allowing
us to examine the similarities and differences between Zener effects in two distinct
electronic systems.

Sample	Hall Bar Width (μm)	Structure	Density $(10^{11}/cm^2)$	Mobility $(10^5 cm^2/Vs)$	$\tau_{tr}\,(ps)$	$\tau_q\,(ps)$
Ah	50	15 nm C-(001) $Al_{0.4}Ga_{0.6}As/GaAs/Al_{0.4}Ga_{0.6}As$ (Ref. 6)	2.06	7	160	12
Bh	100	15 nm C-(001) $Al_{0.4}Ga_{0.6}As/GaAs/Al_{0.4}Ga_{0.6}As$ (Ref. 6)	2.08	5	114	14
Ch	50	Si-(001) $GaAs/Al_{0.3}Ga_{0.7}As$ (Ref.1)	2.00	30	115	10

Table 5.1 : Parameters for sample Ah,Bh and Ch

5.1.2.2 Experiment Setup

Our experiments on 2DHG were carried out by applying the differential resistance measurement technique described in [29], with samples immersed in the coolant (base temperature 300 mK) of a top-loading Oxford helium3 refrigerator, and the magnetic field B applied perpendicular to 2DHG plane. A calibrated thermometer placed in the vicinity of the sample was used to measure the coolant temperature. A constant DC-current bias I_{dc} as well as a AC-modulation current, $I_{ac} = 100nA$ with a frequency $f = 17Hz$, were fed through the sample, and the differential resistance, $r_{xx} = \left(\frac{\partial V}{\partial I}\right)_{I_{dc}} = \frac{v_{ac}}{I_{ac}}$, was then recorded by lock-in amplifiers at the modulation frequency.

5.1.3 Results

Figure.5.1 shows respectively the r_{xx} traces for sample Ah under $I_{dc} = 0, 1, 2, 3, 4, 6, 8, 10\mu A$. At $I_{dc} = 0$, where standard magnetoresistance was observed, SdH shows sharp beating patterns, indicating the existence of two subbands. Fast Fourier Transform anal-

ysis on SdH [38] in the magnetic field range B < 3 T yields the hole densities $p_+ = 1.0 \times 10^{11} cm^{-2}$ ($p_- = 1.1 \times 10^{11} cm^{-2}$) respectively for spin-up (spin-down) heavy-hole subband. There is about 10% difference between them and the energy splitting is about 1.5 K which is quite small and not enough to separate the two subbands, considering the LLs broadening $\Gamma \approx 1.2K$ obtained from CR measurement [38]. However, SdH beats can still be resolved due to the resonance between two sets of LLs in a magnetic field sweep [52].

We now focus on the data in the DC-bias regime, where we observe characteristic signatures of Zener tunneling previously observed in 2DEG. SdH oscillation diminishes and finally disappears presumably due to the carrier heating effect of large current I_{dc}, and in the range B < 5 kG, the r_{xx} is dominated by DC-induced features. Two features should be highlighted: 1) a broad peak in r_{xx}, which presents symmetrically on either magnetic field directions, and which shifts to high B as the I_{dc} increases; and 2), a sharp drop in r_{xx} for each trace beyond a critical magnetic field. These two features correspond, respectively, to the maximum transition probability of Landau transitions and the cutoff of transitions taking place sequentially in increasing B, as depicted by the schematics in Fig. 5.1, top-right. Similar peaks were observed in the r_{xx} traces of the 100 μm Hall bar, sample Bh.

It is worthwhile to examine these features quantitatively as a function of the DC bias current I_{dc}. For this purpose, we determine the B position of 1) by the derivative $\frac{dr_{xx}}{dB} = 0$ (solid dots); and that of 2) by the maximum curvature of r_{xx}, e.g., Max $|\frac{d^2 r_{xx}}{dB^2}|$
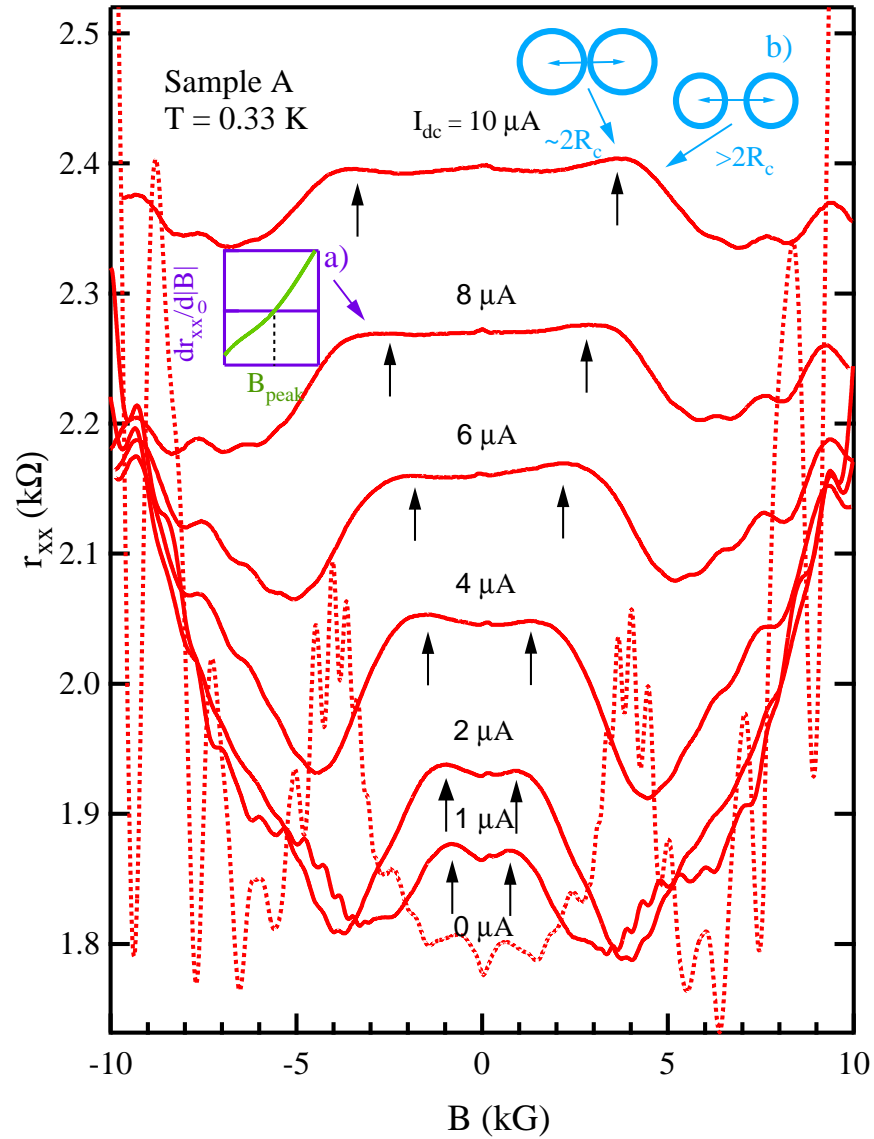
Figure 5.1 : The differential magnetoresistance under $I_{dc} = 0, 1, 2, 3, 4, 6, 8, 10\mu A$ for the 50 μm Hall bar sample (sample Ah) at a temperature 0.33K. A peak (up arrows) arises and shifts to higher magnetic fields with the increase of I_{dc}. The inset a) shows the point $\frac{dr_{xx}}{dB} = 0$ which defines the peak; and the inset b) is the illustration of Zener tunneling mechanism. The dot trace is the magnetoresistance without I_{dc}.
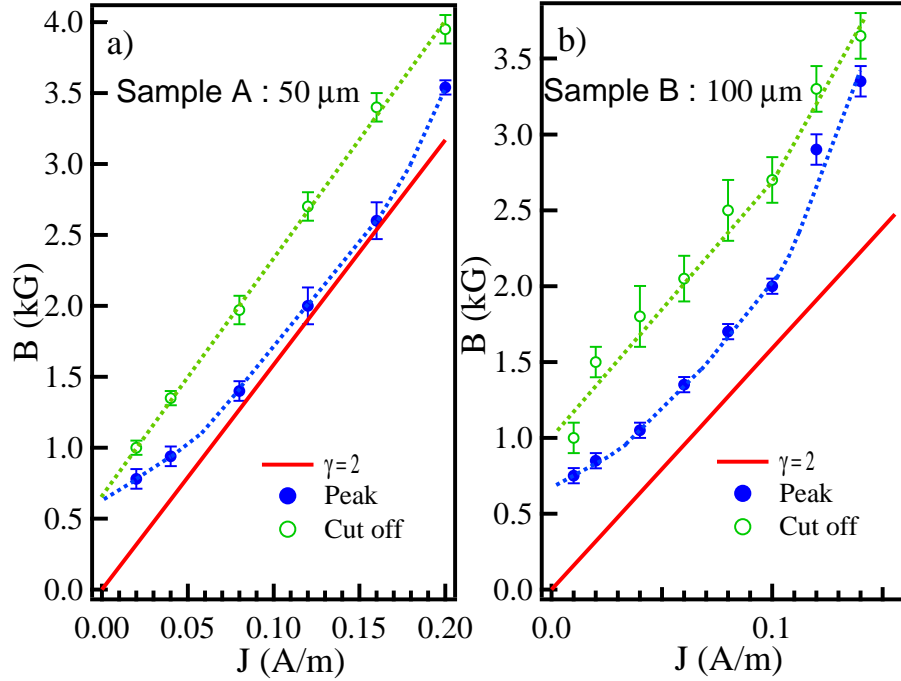
Figure 5.2 : Experimental peak positions (solid dots) and the cutoff positions (open circles) are shown for a) 50 μm (sample Ah), and, b) 100 μm (Bh) Hall bars. The solid lines are the theoretical results with $\gamma = 2$; the dotted lines are guides for the eye only.

(open circles). These data are plotted against the current density $J = \frac{I_{dc}}{w}$ in Fig. 5.2a)

and b), respectively for samples Ah and Bh. The fact that the peak positions are

close to the $\gamma = 2$ lines indicates that, indeed, these features are resulting from the

Zener tunneling effect of 2D holes. As we will discuss in the text, due to spin-orbital

coupling, the peaks may be smeared out by intersubband scattering. Other factors

for consideration include the inhomogeneous current distribution across the Hall bar,

especially in increasing J .

Fig.5.3 shows the temperature dependence of differential magnetoresistance of

sample Ah at $I_{dc} = 5\mu A$. In Fig.5.3a), the Zener peaks disappear gradually as

temperature goes up and can persist up to about 1.5 K. We note that for 2DEG such temperature is about 4 K [29]. The different temperature dependence can be partly account for the fact that the Fermi level in 2DEG sample in [29] is about 80 K and that for sample Ah is about 15 K. The slope of the differential magnetoresistance, i.e.,$\frac{dr_{xx}}{dB}$, near the cutoff is drawn in Fig. 5.3b). In fact, above 0.7 K the slope drops linearly as the temperature goes up. We have also measured the temperature dependence of B = 0 resistance, shown in the Fig. 5.3b), which indicates a T-linear dependence between T = 0.3 K and 1.5 K. Such data appear to confirm that phonon scattering dominates scattering in this temperature range in our 2DHG for B = 0, similar to that observed in GaAs 2DEG [13].

To further examine the Zener effect in a 2DHG, we have measured the differential magnetoresistance in a gated Hall bar. A Ni/Cr metallic gate was fabricated on the surface of the Hall bar, which allowed us to increase the 2DHG density up to $\sim 4 \times 10^{11} cm^{-2}$. In the inset, a mobility vs hole density plot is shown. A somewhat puzzling result is that above approximately $p \approx 2.5 \times 10^{11} cm^{-2}$, the mobilities drops roughly linearly with carrier densities. Notice that our QW is asymmetric due to one-side doping; increasing 2DHG densities by the gate potentials in effect enhances asymmetry and thereby increasing the Rashba spin-splitting. The other factor for consideration is the interface scattering (including both the $Al_{0.4}Ga_{0.6}As$ barrier alloying scattering and the interface roughness scattering), which becomes important as the carrier wavefunction being shifted towards the barrier. We note that simi-
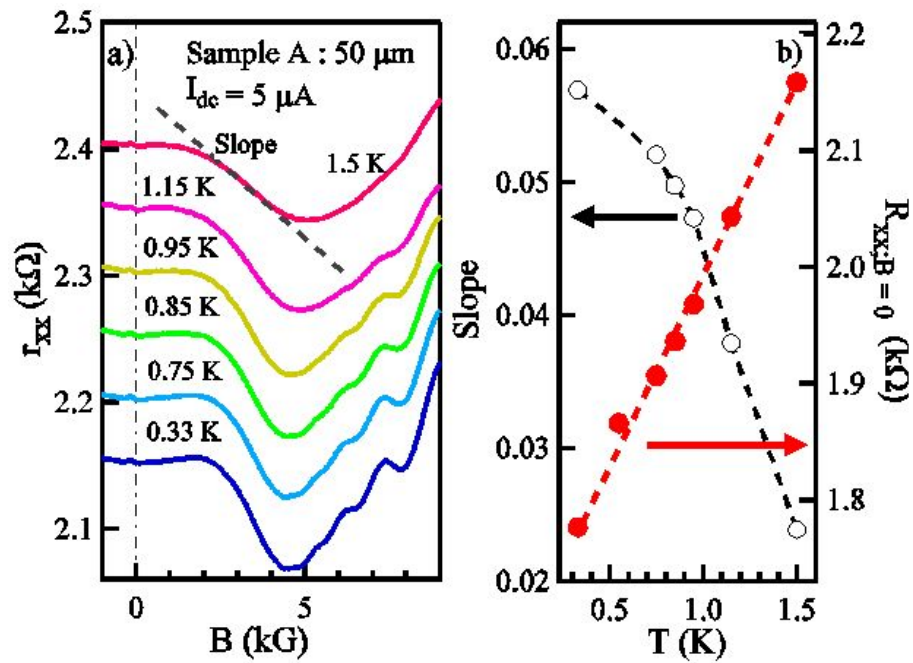
Figure 5.3 : a) The differential magnetoresistance traces are shown for 50 μm Hall bar (sample Ah) at $I_{dc} = 5\mu A$ at 0.33, 0.75, 0.85, 0.95, 1.15, 1.5K, respectively. For clarity, the traces are vertically shifted consecutively by $0.5k\Omega$. The dash line illustrates the slope. b) Solid dots are zero-field temperature-dependent resistance data without applying I_{dc}; Open dots are the slope for different temperatures in a).

lar mobility vs density behavior has been reported for a gated $15nm$ QW, and was attributed to the intersubband scattering involving light hole subband in increasing density [53].

Perhaps the more puzzling observation is that in increasing hole density, the Zener tunneling features gradually disappear. Fig. 5.4 shows the r_{xx} traces measured at T = 0.33 K with $I_{dc} = 1, 2, 4, 6, 8, 10\mu A$ for a hole density $p = 2.63 \times 10^{11} cm^{-2}$. Remarkably, the traces do not show any evidence of Zener effect. On the other hand, the $I_{dc} = 0$ data shows strong positive magnetoresistance, which indicates multi-band scattering dominates the transport in this regime [54, 55]. All together, the data demonstrate that the smearing of Zener features happens concomitantly with the positive magnetoresistance, indicating the involvement of inter-subband scattering.

5.1.4 Discussion

In summary, we have observed the magnetoresistance features in a high-mobility GaAs 2DHG that are consistent with the Zener tunneling mechanism under a DC-bias current. However, in stark contrast to the Zener effect observed in a GaAs 2DEG, such effect is strongly damped in 2DHG. In this study the samples Ah, Bh, and Ch have comparable scattering parameters. This fact indicates that the scattering times τ_{tr} and τ_q are not the only parameters characterizing the transport in Zener oscillation regime.

Presently we do not have a concrete explanation for the observed discrepancy in
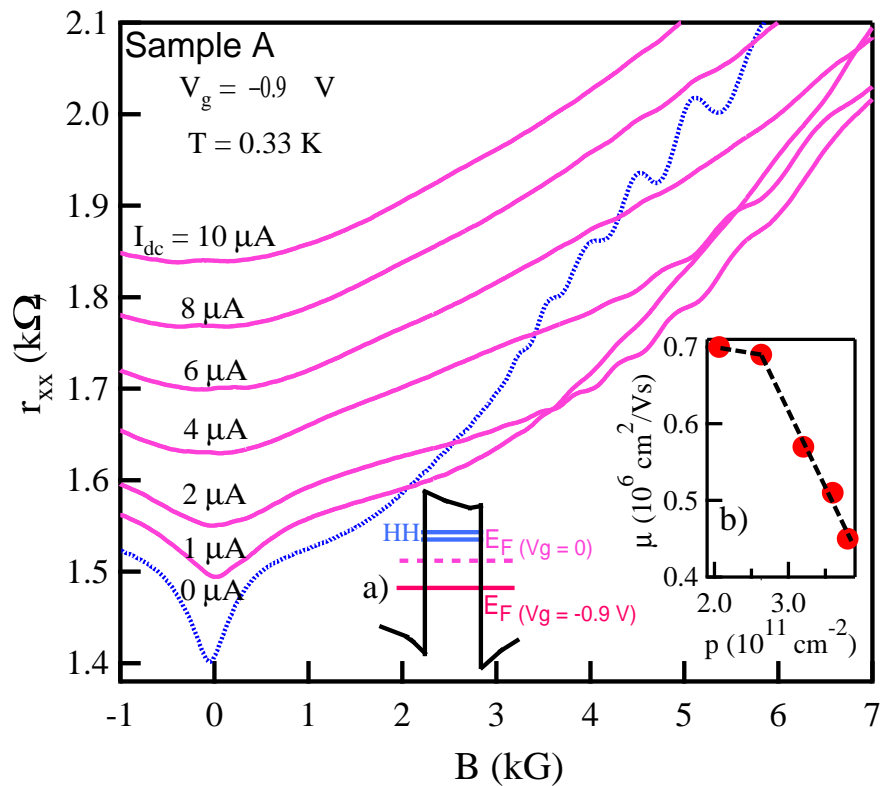
Figure 5.4 : Differential magnetoresistance observed in a gated 2DHG sample is shown. Strong, positive magnetoresistance is observed where there is no evidence for Zener tunneling peaks and valleys. The inset shows the mobility as a function of carrier density in the gated Hall bar.

Zener amplitude between the 2DHG and the 2DEG. Several factors can be considered, however, which may have certain influence for the Zener effect. First, weakness of Zener tunneling in 2DHG may be due to damping via the Dingle factor. The stronger damping in 2DHG comes from its larger effective mass thus smaller LLs spacing. Second, the valence band structure in a QW is known to be complex [56]. In the simplest case where only the spin-up and spin-down heavy-holes are occupied, in a strong bias current, disorder may contribute to scattering between spin-splitting subbands, thus broaden LLs. Moreover, with increasing hole density the effective mass of p_- and that of p_+ acquire different values, the Zener peaks should be further smearing out. Finally, the amplitude of oscillations in DC field is determined by the back-scattering rate [50, 51], and this rate may be significantly different in various systems. Another reason why the DC oscillations are small in 2DHS may be related to the quantum scattering rate without inhomogeneous broadening, i.e. even if SdH oscillations give comparable Dingle factor, suppression of Zener oscillations is determined by the Dingle factor without inhomogeneous broadening.

5.1.5   Conclusion

In conclusion, we have studied the Zener tunneling effect in a high-mobility 2DHG. The data are remarkably consistent with a simple model of commensurate transition of Landau orbits in a Hall field. On the other hand, quantitative difference between the amplitude of the Zener oscillations in 2DEG and 2DHG indicate that the usual

transport scattering time and the Dingle factor cannot adequately describe nonlinear resistance in this regime. A quantum Dingle factor without inhomogeneous broadening is suggested to be responsible for such observations. A complete understanding of nonlinear transport in 2DHG requires theories explicitly dealing with such phenomenon in spin-orbit coupled systems.

5.2 Microwave Induced Resistance Oscillations in Two Dimensional Hole Systems

5.2.1 Experiment

5.2.1.1 Sample

The sample Ah, as mentioned in the Zener tunneling experiment, is used here with 15nm QW,Carbon dopant layer, and 50um Hall bar . Another sample from same wafer of sample Ah, labeled as sample Dh, is shaped as a square, also used in this experiment.

5.2.1.2 Experiment setup

This experiment was done in a He-3 cryogenic. MW, with frequencies 2GHz to 40GHz,was produced by a frequencies generator, sent through a coax line, and delivered on top of samples. A series Guun diod oscillators were used for MW in higher frequencies.
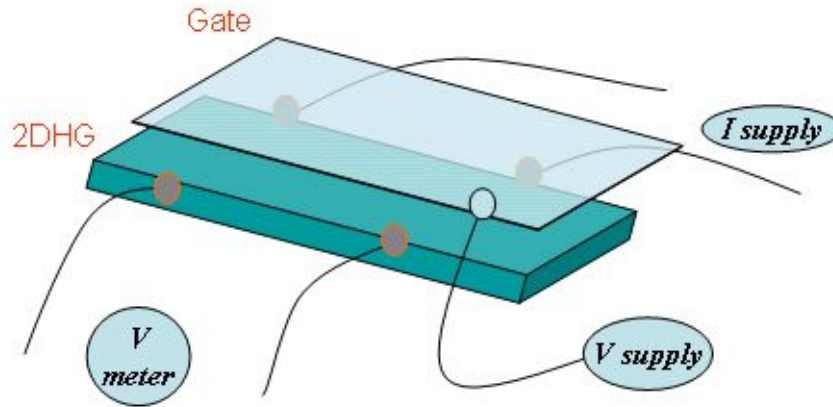
Figure 5.5 : A gated sample illustration. Sample gate is semitransparent for MW illumination. A separate voltage supply was used for gate tuning.

5.2.2 Results

In Figure 5.6, a strong magnetoresistance peak (in black arrow) shows at $\varepsilon = \frac{\omega_{MW}}{\omega_C} = 1$, with MW irradiating on sample Ah . The magnetic field position of the peak is shifted with the frequency of MW. Those peaks are much broader than MIRO peaks in electrons systems. There is no higher order peaks.

The linear relation of frequency and magnetic field of cyclotron peak in Fig. 5.7 covered the a frequency range from 2GHz to 60GHz. Even with the presence of linear relation of frequency and magnetic field, the existence of magnetoplasmon cannot be easily rule out without a survey in a wider frequency range. 2D plasmon for sample Ah with 50um width is $f_p = 1/2\pi(ne^2q)/(2\varepsilon\varepsilon_0 m^*)$, with $q = \pi/w$ and ε dielectric constant, and m^* effective mass. $f_p = 44GHz$ is for this sample.

The data from the square sample Dh also shows similar behavior, which concludes that magnetoresistance peaks in sample Ah observed in Fig. 5.6 and 5.7 is not from
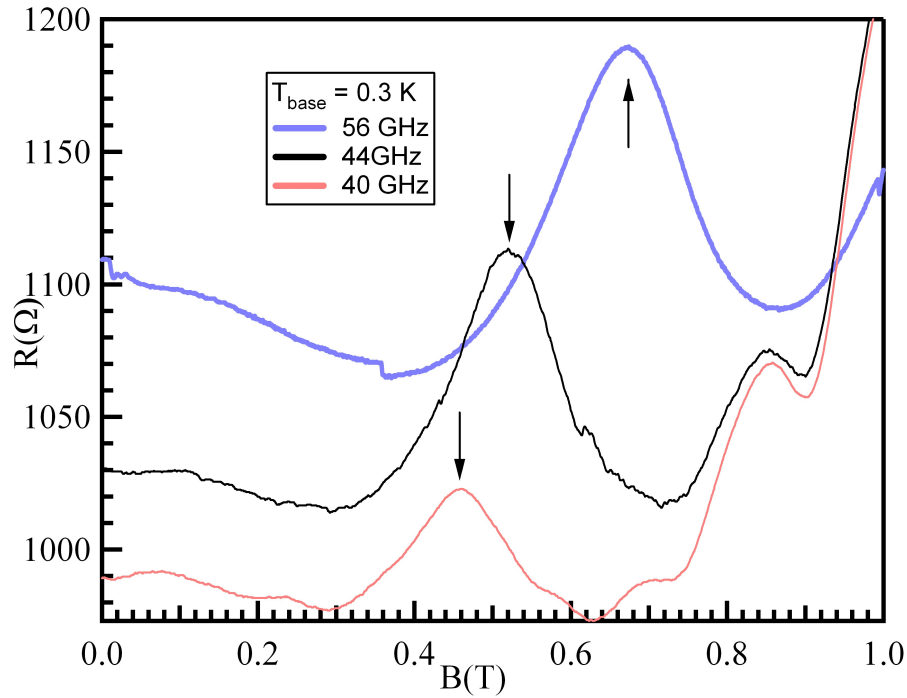
Figure 5.6 : MW induced resistance peaks for 2DHG at frequencies 40 GHz (red line) , 44 GHz (black line), and 56 GHz (blue line). The black arrows point to peaks.

magnetoplasmon.

In the sample Ah, gate voltage was used to adjust density of holes. Negative gate voltage was applied to decrease the density of holes. In Fig. 5.8, there is not shift of cyclotron peaks magnetic field positions with gate voltage 0 V to - 0.704V. But with large gate voltages, cyclotron peaks shift to higher magnetic fields, with reduced amplitude in even larger gate voltages. This shifting may be because density of holes significantly decrease or hole band structures was altered by outside electric field and change peaks position by influencing effective mass of holes.
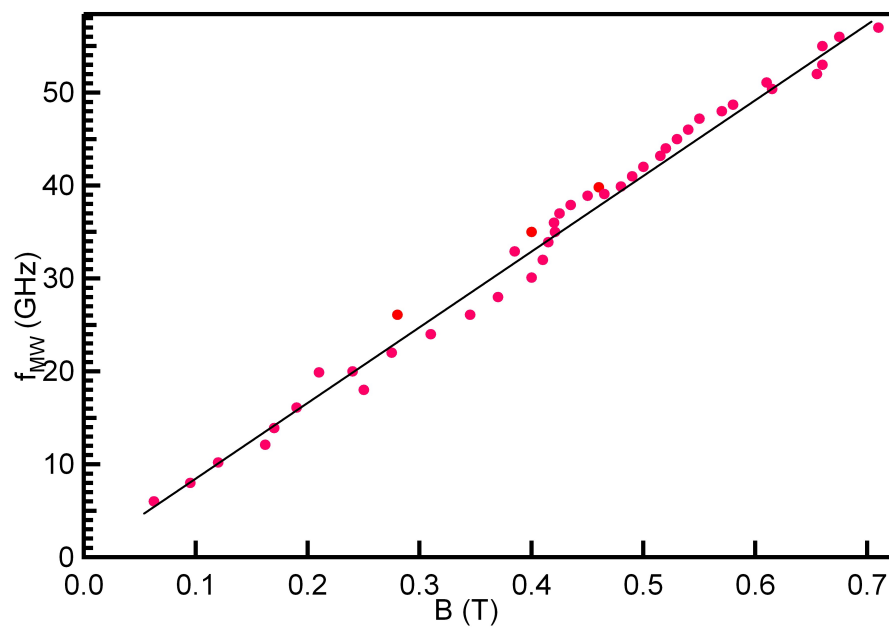
Figure 5.7 : The linear relation between frequencies and magnetic fields of peaks in various frequencies from 2 GHz to 60 GHz
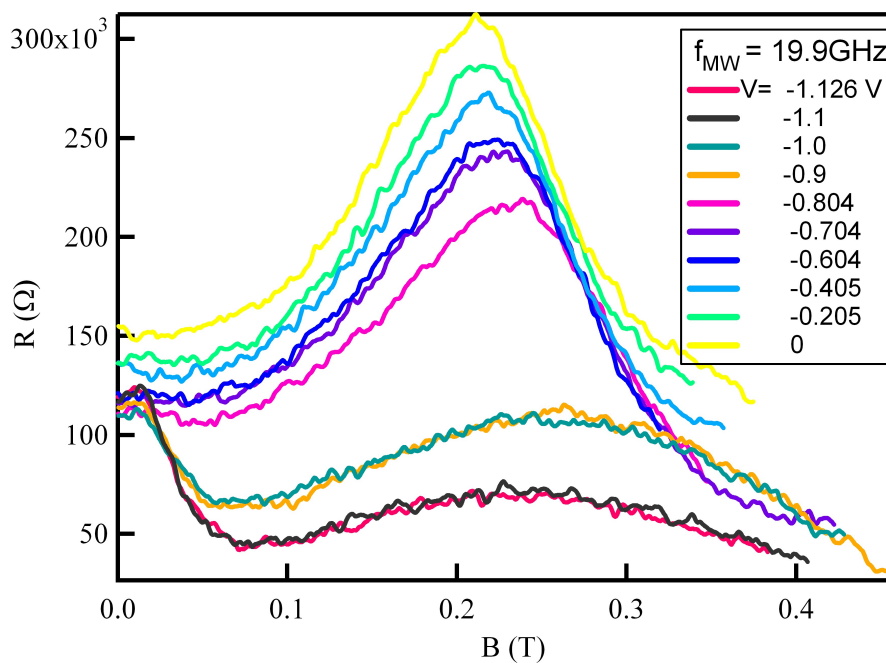
Figure 5.8 : Gate voltage dependence of MIRO in 2DHG. Gate voltages is from 0 to -1.126V. The MW frequency is 19.9GHz.

5.2.3 Conclusion

The MIRO has been observed in 2DHG with a large damping effect, similar to Zener tunneling effect. With a controllable gate voltage, there is a very small phase shift in MIRO peaks for gate voltages smaller than 1V and a large suppression for the gate voltages larger than 1V.

Chapter 6

Conclusions

This thesis collects several discoveries in the field of quantum transport in 2DEG with low magnetic fields applied, made by my colleagues and me over the last few years.

In 2DEG irradiated by microwave, a new peak, namely cyclotron harmonic peak or $2\omega_C$ spike, can be observed in magnetoresistance with a very high quality factor. No phase shift is displayed even when an in-plane magnetic field is applied. High mobility of the sample and high frequencies have been determined to be the favorable conditions for this kind of spike.

In the presence of a modulated antidots lattice potential, ultra-high mobility 2DEG exhibits the AB effect in magnetotransport in the MIRO regime when microwave irradiation is applied. This kind of AB effect is observable when the irradiation possesses relatively high frequencies, but disappears in an in-plane magnetic field.

GR in this kind of ultra-high mobility 2DEG has been systematically studied using several samples, differing from each other in density, mobility, aspect ratio, and lattice array. Although the density and lattice constant influence the GR cyclotron magnetic field, same or similar lattice arrays determine that the magnetoresistance oscillations display the same period in GR regime after normalization. In addition,

the oscillation of hall voltage further indicates the existence of magnetic lattices.

In 2DHG, large damping factors have been discovered in two nonlinear effects, namely Zener tunneling and MIRO, which derive from the complex structure of hole bands as well as the large effective mass of holes.

Overall, a variety of new phenomena during the quantum transport process in low magnetic fields have been discovered. They broaden our view on 2DEG and 2DHG transport and help us to understand the carrier motion in two dimensional systems, including their interference, scattering from disorders, and response to spontaneous or artificial potential, etc. Two dimensional systems, clean and rich in physics, are expected to keep being quested by future physicists.

Bibliography

[1] John H. Davis, *The physics of Low-Dimensional Secmiconductors* (Cambridge University Press, New York, 1998). xii, 7, 9

[2] C. Yang, J. Zhang, R. Du, J. Simmons, and J. Reno, Physical Review Letters **89**, 1 (2002), ISSN 0031-9007. xiii, 2, 10, 13

[3] M. Zudov and R. R. Du, Physical Review Letters **90**, 2 (2003), ISSN 0031-9007. xiii, 2, 12, 14

[4] Z. Yuan, C. Yang, R. Du, L. Pfeiffer, and K. West, Physical Review B **74**, 2 (2006), ISSN 1098-0121. xiii, 3, 15, 47

[5] R. Webb, S. Washburn, C. Umbach, and R. Laibowitz, Physical Review Letters **54**, 2696 (1985), ISSN 1079-7114. xiii, 18

[6] M. Kato, A. Endo, S. Katsumoto, and Y. Iye, Physical Review B **77**, 1 (2008), ISSN 1098-0121. xiv, 18, 19, 47

[7] D.-H. Lee and J. Leinaas, Physical Review B **69**, 1 (2004), ISSN 1098-0121. xvi, 31, 32

[8] K. Von Klitzing, G. Dorda, and M. Pepper, Physical Review Letters **45**, 494 (1980). 1, 8

[9] D. C. Tsui, H. L. Stormer, and A. C. Gossard, Physical Review Letters **48**, 1559 (1982), ISSN 00319007. 1

[10] R. B. Laughlin, Physical Review Letters **50**, 1395 (1983), ISSN 00319007. 1, 2

[11] D. C. Tsui, G. J. Dolan, and A. Gossard, Bull. Am. Phys. Soc. **28**, 365 (1983). 2

[12] M. Zudov, Ph.D. thesis (1999). 2

[13] M. Zudov, R. R. Du, J. Simmons, and J. Reno, Physical Review B **64**, 201311 (2001). 2, 12, 79

[14] P. D. Ye, L. W. Engel, D. C. Tsui, J. A. Simmons, J. R. Wendt, G. A. Vawter, and J. L. Reno, Applied Physics Letters **79**, 2193 (2001). 2

[15] R. G. Mani, Nature **420**, 646 (2002). 2, 12

[16] C. L. Yang, M. Zudov, T. a. Knuuttila, and R. R. Du, Physical Review Letters **91**, 1 (2003), ISSN 0031-9007. 2, 12

[17] R. Winkler and J. Kotthaus, Physical Review Letters **62**, 1177 (1989). 3

[18] R. R. Gerhardts, D. Weiss, and K. von Klitzing, Physical Review Letters **62**, 1173 (1989). 3

[19] D. Weiss, K. V. Klitzing, K. Ploog, and G. Weimann, Europhysics Letters (EPL) **8**, 179 (1989), ISSN 0295-5075. 3

[20] D. Weiss, K. V. Klitzing, K. Ploog, and G. Weimann, Europhysics Letters (EPL) **8**, 179 (1989), ISSN 0295-5075. 3

[21] D. Weiss, M. Roukes, A. Menschig, P. Grambow, K. Von Klitzing, and G. Weimann, Physical Review Letters **66**, 2790 (1991). 3, 47

[22] S. Studenikin, M. Potemski, A. Sachrajda, M. Hilke, L. Pfeiffer, and K. West, Physical Review B **71**, 1 (2005), ISSN 1098-0121. 12

[23] S. Studenikin, A. Sachrajda, J. Gupta, Z. Wasilewski, O. Fedorych, M. Byszewski, D. Maude, M. Potemski, M. Hilke, K. West, et al., Physical Review B **76**, 1 (2007), ISSN 1098-0121. 12, 25

[24] A. V. Andreev, I. L. Aleiner, and A. J. Millis, Physical Review Letters **91**, 056803 (2003). 12

[25] A. Auerbach, I. Finkler, B. I. Halperin, and A. Yacoby, Physical Review Letters **94**, 1 (2005), ISSN 0031-9007. 12

[26] A. Durst, S. Sachdev, N. Read, and S. Girvin, Physical Review Letters **91**, 1 (2003), ISSN 0031-9007. 14

[27] D. Heitmann, Surface Science **170**, 332 (1986), ISSN 0039-6028. 14

[28] D. Heitman, M. Ziesmann, and L. Chang, Physical Review B **34**, 7463 (1986). 14, 32

[29] C. Yang, R. Du, L. Pfeiffer, and K. West, Physical Review B **74**, 1 (2006), ISSN 1098-0121. 15, 25, 36, 73, 74, 75, 79

[30] Y. Zhang, *Quantum Mechanics* (Science Press, 2002). 16

[31] P. T. Colebridge, Physics Review B **44**, 3793 (1991). 21

[32] S. Syed, M. J. Manfra, Y. J. Wang, R. J. Molnar, and H. L. Stormer, Applied Physics Letters **84**, 1507 (2004), ISSN 00036951. 21

[33] Z. Yuan, Ph.D. thesis (2009). 22

[34] A. Dmitriev, S. Emelyanov, S. V. Ivanov, P. Kopev, Y. Terentev, and I. Yaroshet-skii, JETP letters **54**, 462 (1991). 32

[35] A. Dmitriev, Sov.Phys.JETP **72**, 347 (1991). 33

[36] A. Mirlin, D. Polyakov, F. Evers, and P. Wölfle, Physical Review Letters **87**, 126805 (2001), ISSN 1079-7114. 34

[37] Y. Dai, R. Du, L. Pfeiffer, and K. West, Physical Review Letters **105**, 2 (2010), ISSN 0031-9007. 34

[38] Z. Q. Yuan, R. R. Du, M. Manfra, L. Pfeiffer, and K. West, Applied Physics letter **94**, 052103 (2009). 42, 74, 76

[39] M. Zudov, I. V. Ponomarev, a. L. Efros, and R. R. Du, Physical Review Letters **86**, 3614 (2001), ISSN 0031-9007. 44

[40] T. Yamashiro, J. Takahara, K. Takagaki, and Others, Solid state communications **79**, 885 (1991), ISSN 0038-1098. 47

[41] J. Takahara, T. Kakuta, T. Yamashiro, Y. Takagaki, T. Shiokawa, K. Gamo, S. Namba, S. Takaoka, and K. Murase, Japanese journal of applied physics **30**, 3250 (1991), ISSN 0021-4922. 47

[42] E. Baskin, G. Gusev, Z. Kvon, A. Pogosov, and M. Entin, Soviet Journal of Experimental and Theoretical Physics Letters **55**, 678 (1992). 47

[43] S. Ishizaka, F. Nihey, K. Nakamura, and T. Ando, Physical Review B **51**, 9881 (1995). 47

[44] S. Ishizaka and T. Ando, Physical Review B **55**, 16331 (1997), ISSN 0163-1829. 47

[45] L. Moore and D. Goldhaber-Gordon, stanford.edu **3**, 295 (2007). 59

[46] C. Siegert, A. Ghosh, M. Pepper, I. Farrer, and D. Ritchie, Nature Physics **3**, 315 (2007), ISSN 1745-2473. 59

[47] A. T. Hatke, H.-S. Chiang, M. A. Zudov, L. Pfeiffer, and K. West, Physical Review Letters **101**, 246811 (2008). 73

[48] A. Hatke, M. Zudov, L. Pfeiffer, and K. West, Physical Review B **79**, 161308 (2009). 73

[49] Zhang W., C. H.-S, Z. M.A, L. Pfeiffer, and K. West, Physical Review B **75**, 041304(R) (2007). 73

[50] M. G. Vavilov, Physical Review B **76**, 115331 (2007). 74, 83

[51] M. Khodas and M. G. Vavilov, Physical Review B **78**, 245319 (2008). 74, 83

[52] M. Raikh and T. Shahbazyan, Physical Review B **49**, 5531 (1994). 76

[53] C. Gerl, S. Schmult, H.-P. Tranitz, C. Mitzkus, and W. Wegscheider, Applied Physics Letters **86**, 252105 (2005), ISSN 00036951. 81

[54] B. Grbic, C. Ellengerger, T. Ihn, K. Ensslin, D. Reuter, and A. Wieck, Applied Physics letter **85**, 2277 (2004). 81

[55] B. Grbic, R. Leturcq, T. Ihn, K. Ensslin, D. Reuter, and A. Wieck, Physical Review B **77**, 125312 (2008). 81

[56] R. Winkler, *Spin-orbit Coupling Effects in Two-dimensional Electron and Hole Systems* (Springer-Verlag,Berlin, 2003). 83

[57] L. Ponomarenko, A. Visser, and A. Pruisken, Physical Review B **75**, 035313 (2007). 104

Appendix A

Fabrication of an Antidot Lattice Pattern on a Hall bar Mesa

To make a Hall bar mesa (tens or hundreds μm) with an antidot lattice pattern or any other small scale patterns ($l^\sim 1$ μm or smaller), it is necessary to use both photolithography and e-beam lithography. There are two different process sequences. First one is making large features first and then fabricating small patterns afterward. Second one is to make small features first and fabricate large patterns. In making transport samples of carbon nanotubes , nanotubes are deposited on the substrate first and the electrodes are made after that by locating nanotubes under Scanning Electron Microscope(SEM). The GaAs samples, used to fabricate antidot patterns, only available in $4mm \times 4mm$ squares. In order to maximum use the sample, first process sequence is the choice.

A.1   Hall Bar Fabrication

Hall bar fabrication usually has several flows: 1) making an optical mask for photolithography, 2) making ohmic contacts using the lift off technique, 3) making the Hall bar by photolithography.

In Figure A.1, the Hall bar contains three parts.Two sections are with a antidots lattice and in the middle section, there is a Hall bar mesa without the antidots lattice.
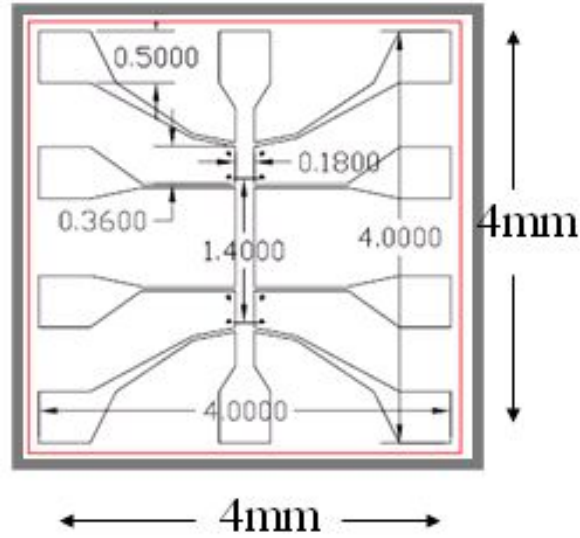
Figure A.1 : The Hall bar design for 4mm×$4mm$ square GaAs/AlGaAs.

The width of the hall bar were $90\mu m$ or $180\mu m$ and the length is $1000\mu m$. Around the sections with antidots, there are four L shape makers for each section. Those makers were used to align antidot arrays with the Hall bar geometry.

A.2   Antidot Lattice Patterns Fabrication

Two flows are included in antidot lattice patterns fabrication: 1) designing antidot lattice patterns using Design CAD, 2) transferring antidots design using SEM and Nanometer Pattern Generation System (NPGS) software to the Hall bar mesa.

Fig. A.2 gives an example on the antidot arrays design in Design CAD. Note that since the dot area will be etched away, dash line must be used for dot circles. Finally , the design lines must be converted to vectors.

The design file will be later used in NPGS (A.3) and along with the run file to
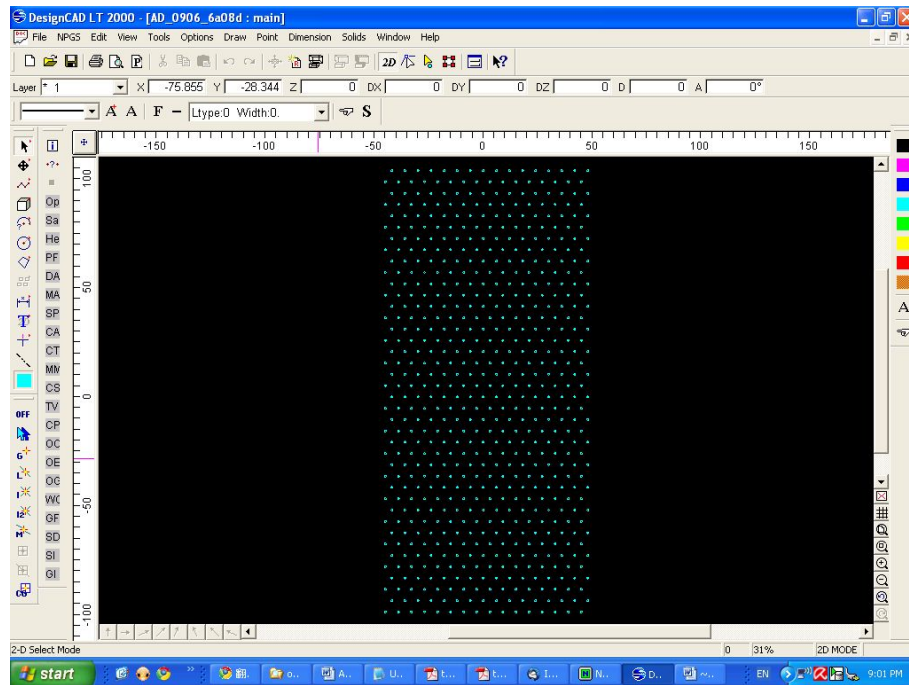
Figure A.2 : A antidot triangular array design in design CAD lattice constant 6 μm and d diameter is $0.8\mu m$in design. width $90\mu m$.

control the electron beam motion. The run file has several parameter settings as in Fig. A.4, A.5. This run file has one loaded entity and repeats writing the pattern only once. The center of the pattern locates at (0,0). In some run files, multiple patterns are loaded with many repeats, the center of each pattern may be different from (0,0).

The parameters for this pattern are shown on the right part in Fig. A.5. The e-beam is focused onto a very small dot, maybe around 10 nm diameter depending on different SEMs, so it can write the patterns like a pen. In order to cover a big area, a grid of dots is drawn. Because of back scattering effect, the density of dots do not have to be very large and it is determined by the center to center distance and
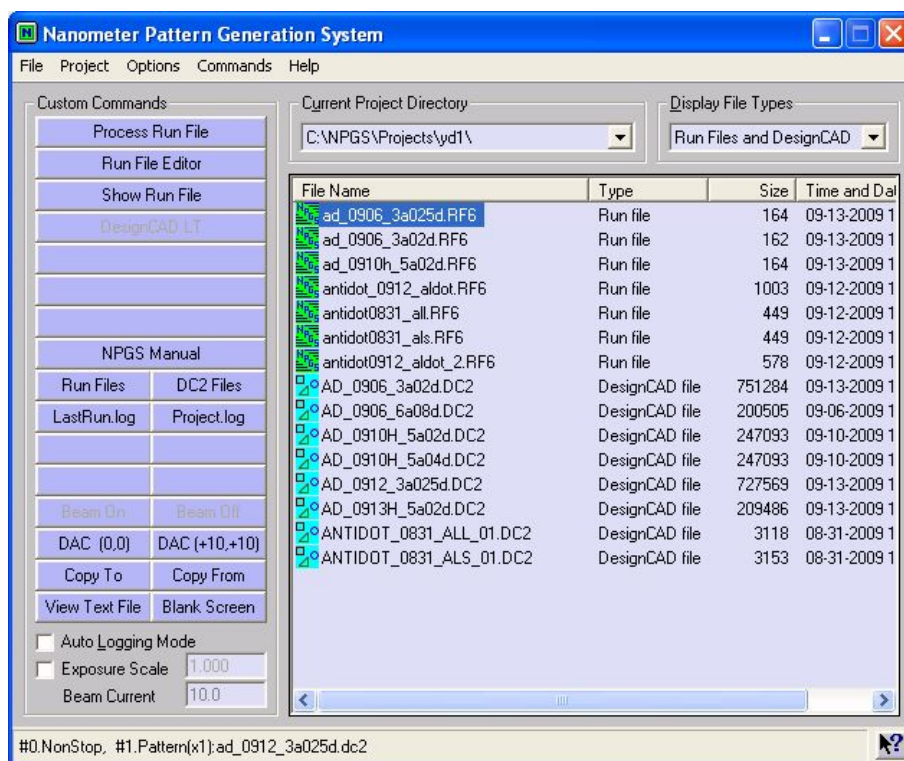
Figure A.3 : NPGS current projects including design CAD files and run files
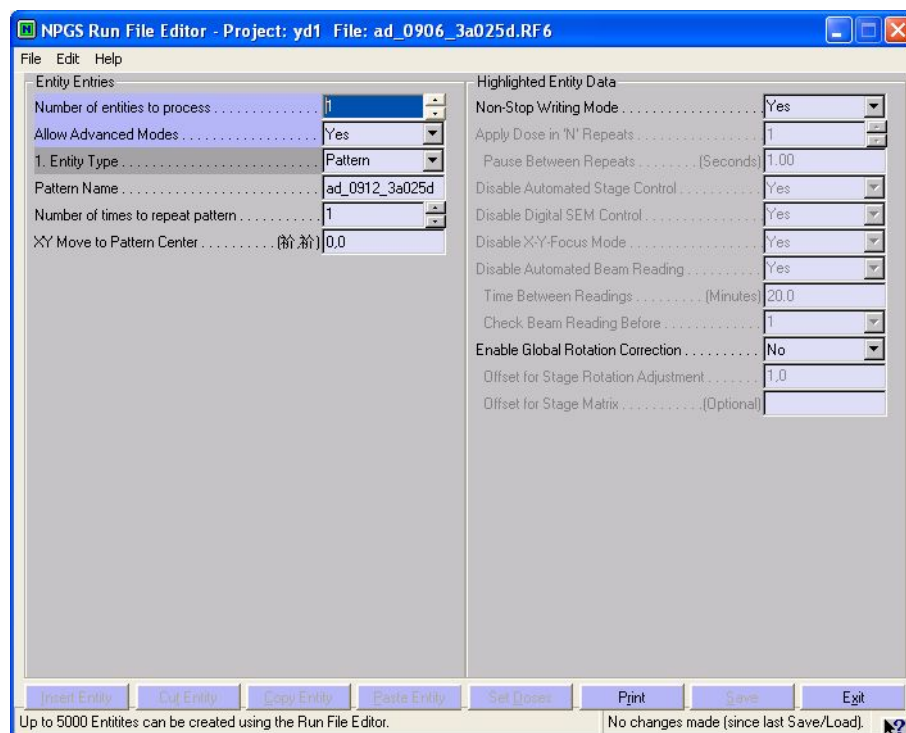
Figure A.4 : NPGS run file editor window with the parameters commonly used.

the line spacing. The dot size is affected by the time (Dwell) of beam staying on one spot or by the number of electrons per area (area dose). For a very-fine structure, those must be considered to get a satisfied result.

In the parameter setting panel, Origin offset is usually set to (0,0). Magnification was set to fit the one pattern into the scope and this will be adjusted automatically if too large value is employed and the pattern is outside the edge of the image scope. The center to center distance and the line spacing are used to set the e-beam dot distance in two directions. Measured beam current is a reading from a current meter when focusing e-beam to one spot for a few seconds.

In Fig. A.6, left image is the written pattern on the top of the hall bar mesa. To
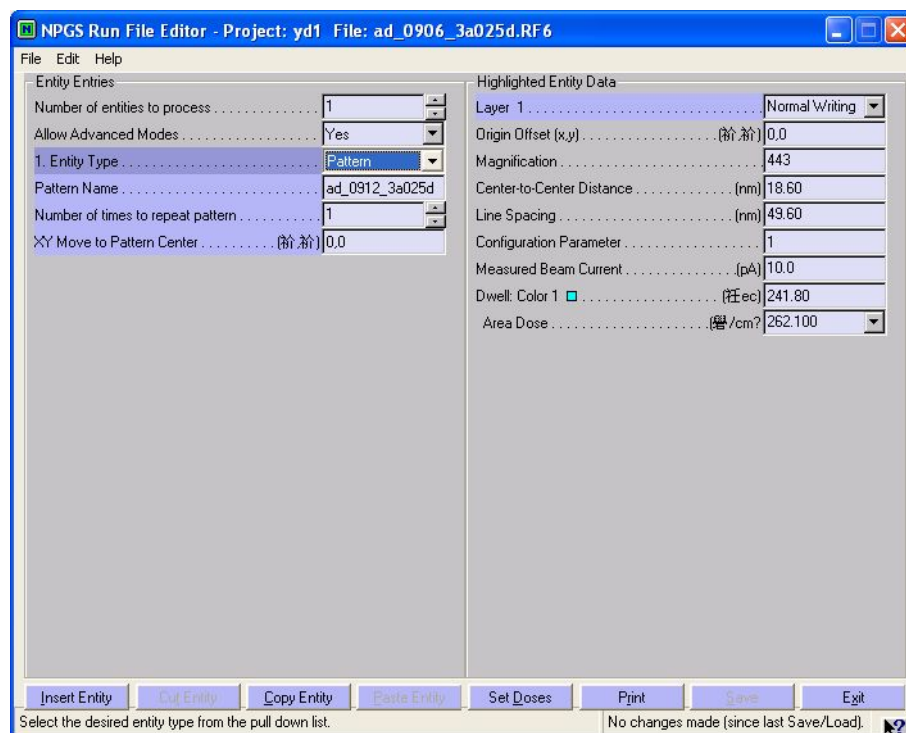
Figure A.5 : NPGS run files editor window with pattern parameters on the right.

align this pattern along with the hall bar, four makers were made in four corners of the hall bar section. Since the pattern center should be overlapped with the mesa center, four makers were first imaged and their coordinates were recorded, from which the coordinate of the center of mesa was derived.

A.3   Finishing

After finishing all the steps, the samples are to placed on a chip carrier and wired with gold wires.
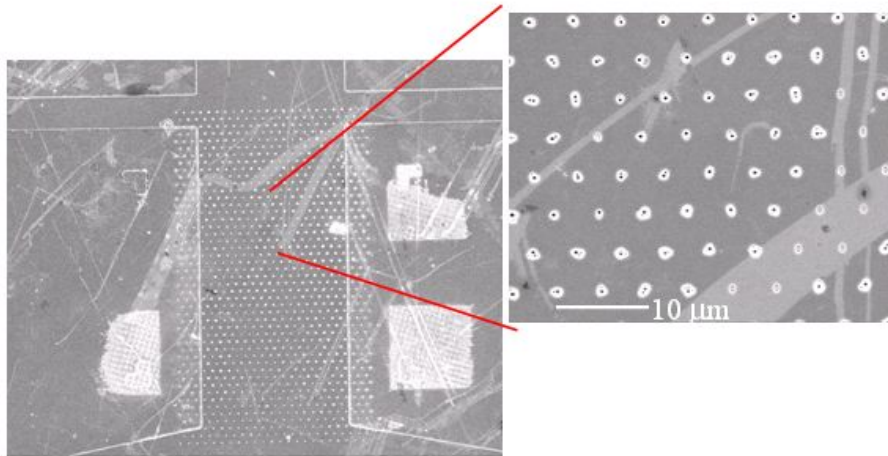
Figure A.6 : SEM image of the Hall bar section with a antidot lattice on (left) and antidots (right) .

Appendix B

Characterization of Samples InP/InGaAs and InGaAs/GaAs

B.1 InP/In$_{0.53}$Ga$_{0.47}$As

Three different types of InP/In$_{0.53}$Ga$_{0.47}$As were measured.

B.1.1 Sample 1015 and 1023

Those two samples are from Princeton for the project of the quantized Hall insulator state[57]. The Figure B.1 is for the crystal structure of InP/InGaAs as well as the band structure. InP and In$_{0.53}$Ga$_{0.47}$As are the lattice matched. The samples are in 1mm×1mm square shape. Hall resistivity as well as longitudinal resistivity have been measured in different temperatures from 29mK to 1.3K. The density of 1015 is $1.7 \times 10^{11} cm^{-2}$ and the mobility is $7 \times 10^4 cm^2/Vs$. In Fig. B.2 for sample 1015, the quantized hall insulator state is persistent to 12T and a quantum critical point is at 12.6 T, $\nu = 0.52$, in a blue circle. For sample 1023, the density is $2.0 \times 10^{11} cm^{-2}$ and the mobility is $1 \times 10^5 cm^2/Vs$. There is no quantum critical point in sample 1023 in Fig. B.3.
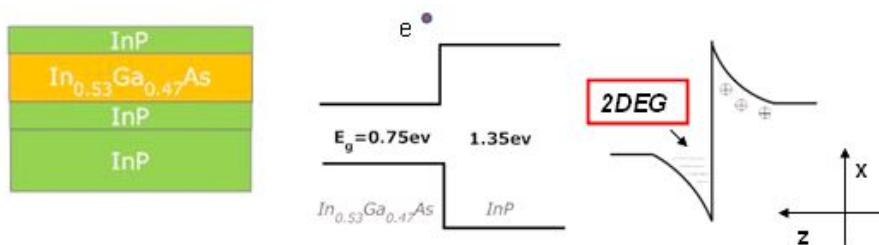
Figure B.1 : Lattice matched InP/InGaAs. From left to right, the wafer structure, the conduction band of InP/InGaAs and the triangular QW with 2DEG trapped inside.
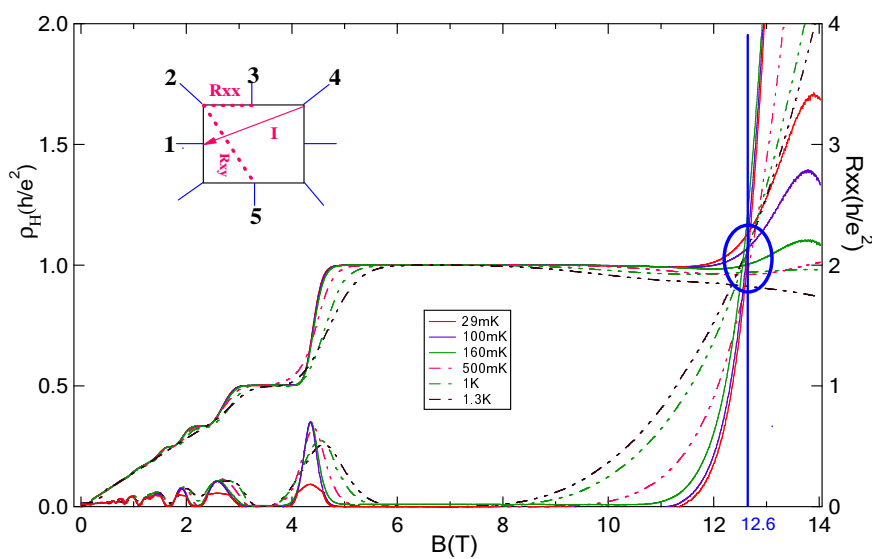
Figure B.2 : Hall resistivity traces with the quantized Hall insulator state and longitudinal resistivity traces in various temperatures for sample 1015. Quantum critical point is in the blue circle.
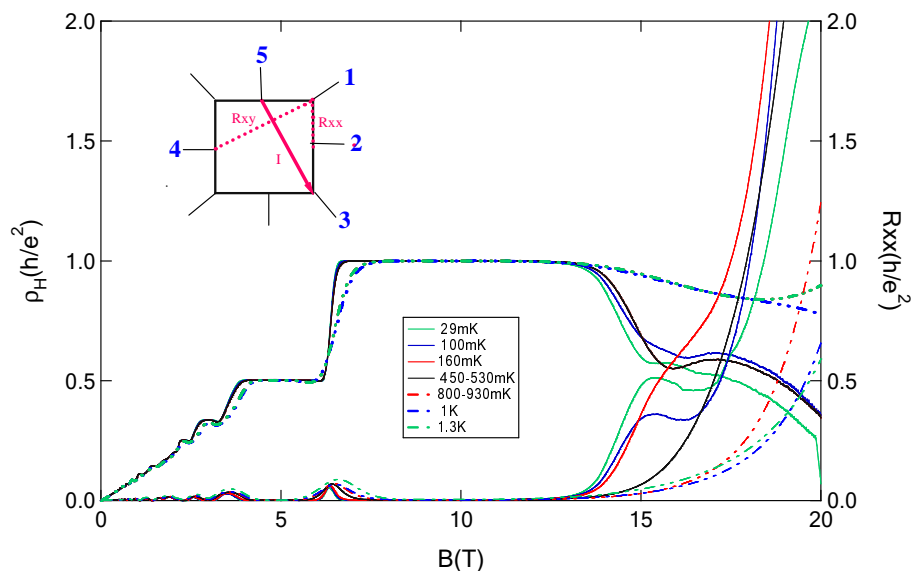
Figure B.3 : Hall resistivity traces with the quantized Hall insulator state and longitudinal resistivity traces in various temperatures for sample 1023. No quantum critical point.

B.1.2   IQH samples

The wafers are from IQH , a industrial company, and made from Molecule Beam Epitaxy. In Fig. B.4, the sample structure with a top doped layer results in an asymmetric QW. A magnetoresistance trace shows up to $\nu = 4$. SdH oscillations are in Fig. B.5.

B.1.3   Samples Grown from Metal Organic Chemical Vapor Deposition (MOCVD)

The Fig. B.6 is the characterization trace for InP/InGaAs grown from MOCVD.
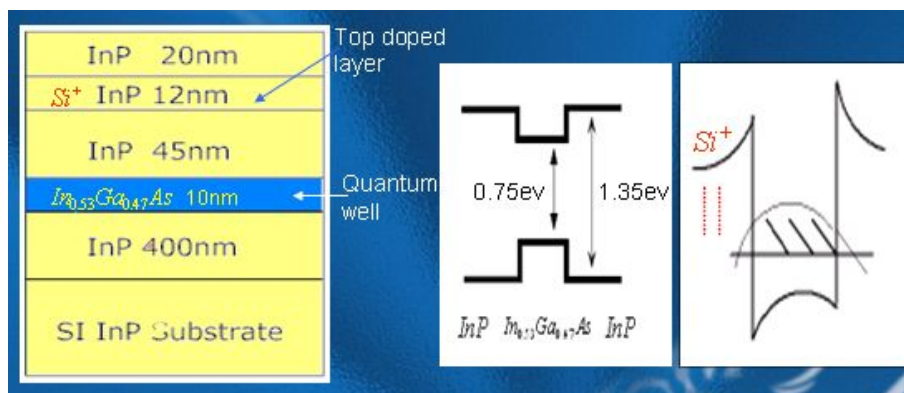
Figure B.4 : Lattice matched InP/InGaAs from IQH. From left to right, the wafer structure, the conduction band of InP/InGaAs, and an asymmetric QW with 2DEG inside.
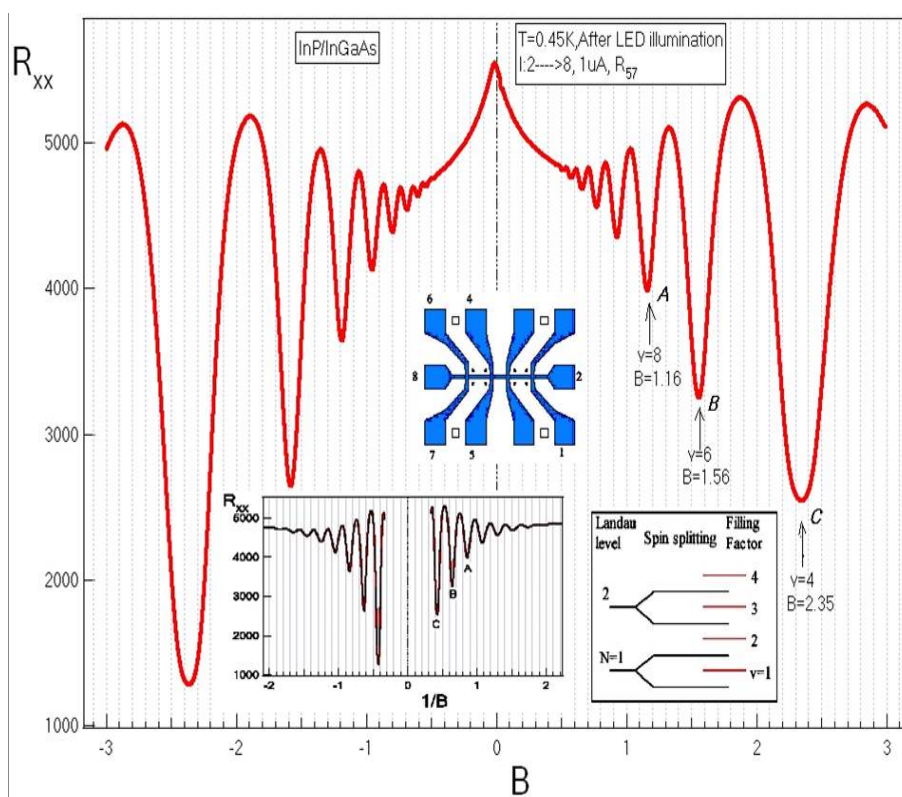
Figure B.5 : Magnetoresistance for InP/InGaAs up to $\nu = 4$. The Hall bar Geometry is in blue.
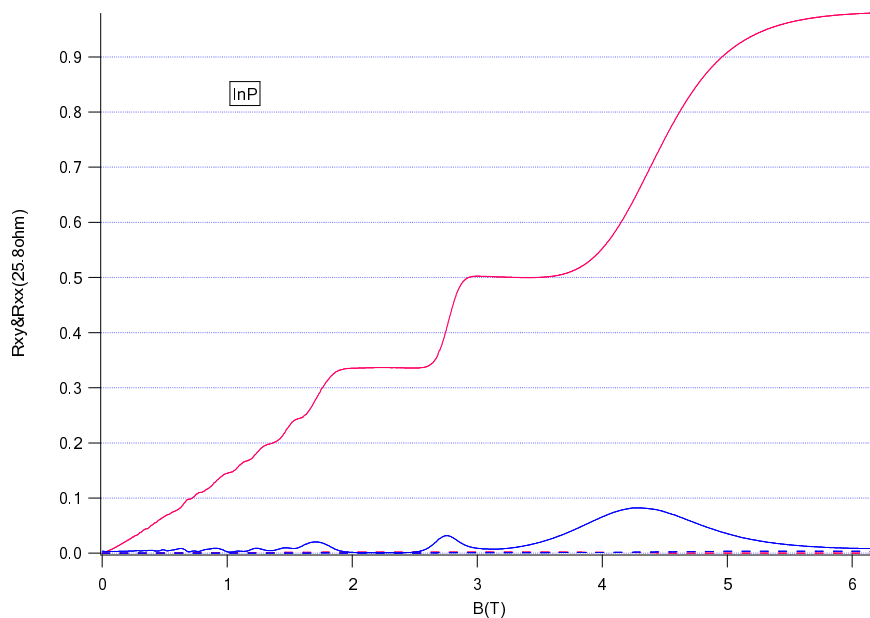
Figure B.6 : Characterization of InP/InGaAs. Blue line is SdH and Red line is IQHE.

B.2   In$_{0.53}$Ga$_{0.47}$As/InAlAs

B.2.1   Characterization

The sample structure, the band structure, and characterization traces are in the following Fig. B.7,B.8,B.9. There is some mixing in hall voltage with longitudinal voltage in sample V4 and V6, which is not good for the quantum transport purpose experiment. The density and mobility could calculated from the characterization traces. The best sample is V5, with density of electrons $2 \times 10^{11} cm^{-2}$ and mobility $8 \times 10^4 cm^2/Vs$.
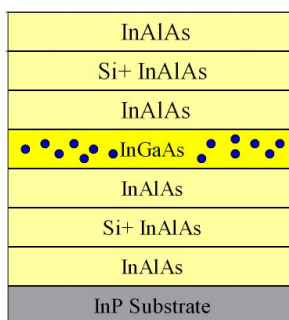
(a) V3 with symmetric dopant layers
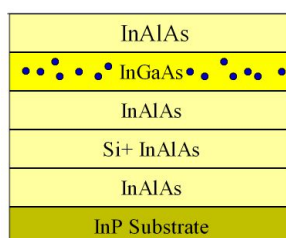
(b) V4 with a bottom dopant layer
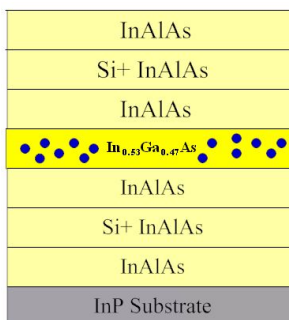
(c) V5 with symmetric dopant layers
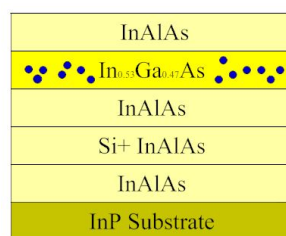
(d) V6 with a top dopant layer

Figure B.7 : Sample Structures for InGaAs/InAlAs V3,V4,V5,V6.
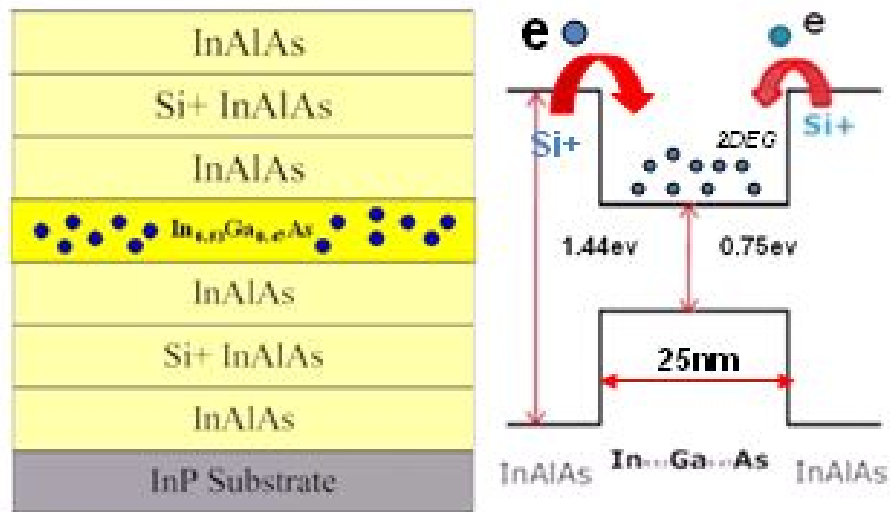
Figure B.8 : A InGaAs/InAlAs sample structure, with symmetric doping layers, (left) and the band structure (right)

B.2.2   Gated In$_{0.53}$Ga$_{0.47}$As/InAlAs Samples

To adjust the density in InGaAs/InAlAs, a gate with 100nm Al and 100nm Al$_2$O$_3$ was fabricated on top of 2DEG. The magnetoresistance with different gate voltages as shown in Fig. B.10.

B.2.3   the Insulator State in Gated InGaAs/InAlAs

In Fig. B.11, there is a insulator state in high magnetic field for a gated hall bar. The density of electron is $2 \times 10^{11} cm^{-2}$. Quantum critical point is at 15.3T and $\nu = 0.56$ at this density.
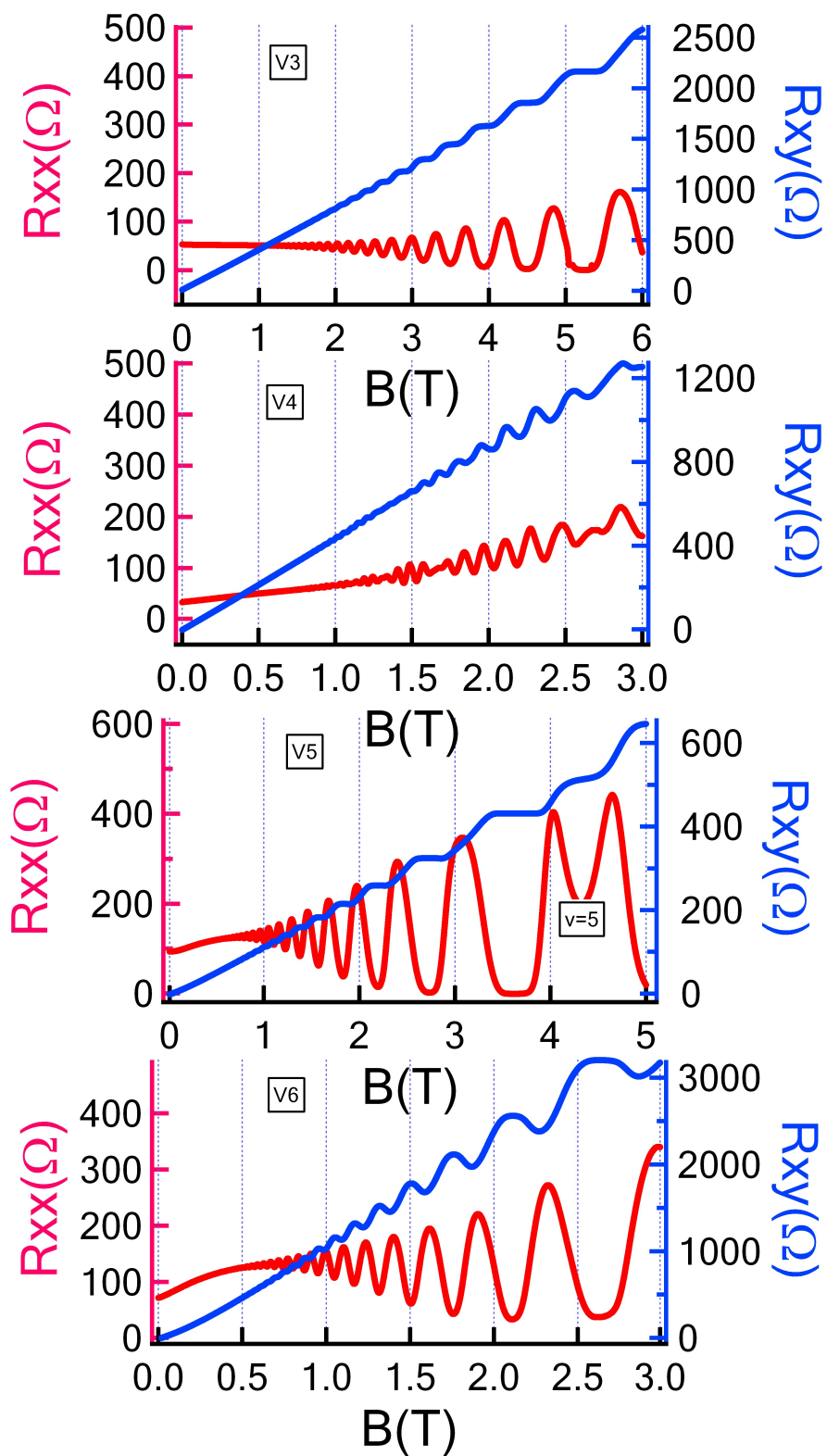
Figure B.9 : Characterization of InGaAs/InAlAs V3,V4,V5, V6. Blue traces are IQHE and Red Traces are SdH.
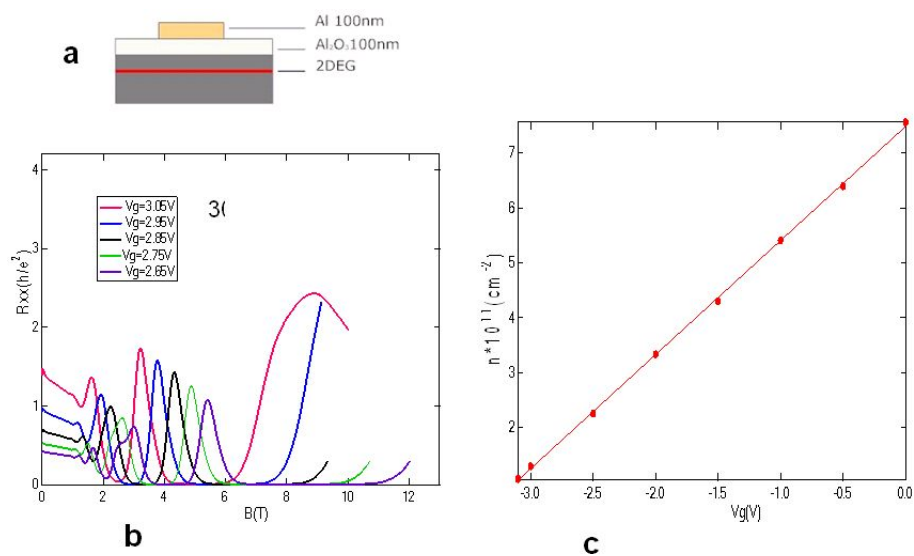
Figure B.10 : Gated InGaAs/InAlAs. a) Illustration of a gated sample b) magnetoresistance in different voltages c) density of electrons versus gate voltage. The line shows the linear relation between them.
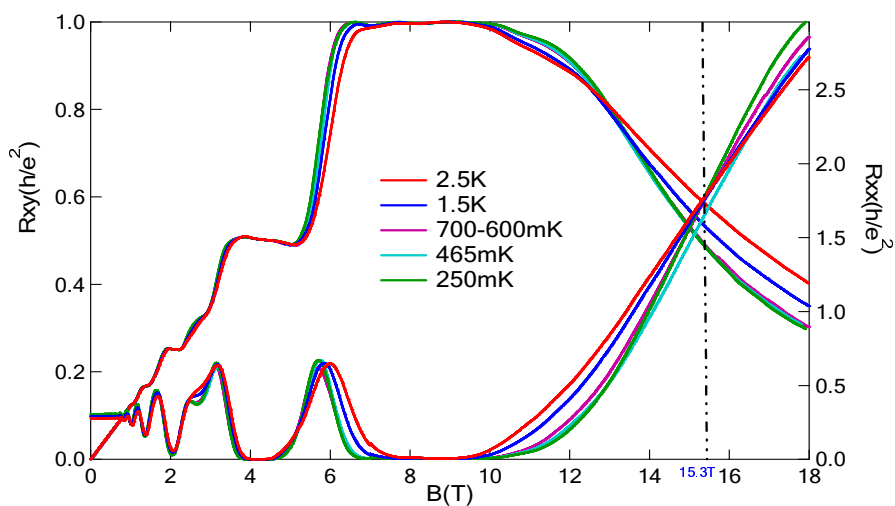
Figure B.11 : Temperature dependent traces for a gated InGaAs/InAlAs from 250mK to 2.5K.